A Low Complexity 6DoF Magnetic Tracking System For Biomedical Applications

Thesis submitted to the Politecnico di Torino for the degree of **PhD in Electrical, Electronics and Communications Engineering, July 2021.**

David A. Fernandez G.

S251991

Supervised by

Prof. Danilo Demarchi
PhD. Marco Crepaldi

Signature _____

Date _____ / _____ / _____

Abstract

In this thesis work, we present the development of a Six Degrees of Freedom (6DOF) magnetic tracking system based on a low computational complexity algorithm and a low-cost, wireless and wearable hardware for biomedical applications.

We start by studying the role of the different types of tracking systems presented in the literature on the biomedical field, with a special interest in upper limb motion tracking, hand fingers motion tracking and medical instrumentation tracking. Based on this study, we choose to work with magnetic tracking techniques and set our system general characteristics.

Then, we present a literature review of magnetic tracking systems from which we extract our thesis goals, design constraints and research contribution to the field which consists of designing a wearable wireless magnetic tracking system based on the use of a lightweight algorithm onboard a small-sized low-cost MCU that can acquire and process the magnetic field signals perceived by movable sensors and transmit the estimated sensor position and orientation to an end-user device via wireless communication, projecting to the substitution of gold standard high-cost systems for the development of medical device of its use as an assessment tool in the research field.

Following the presented research methodology consisting of short experimentally driven step development cycles, we expose our system development from exposing our proposed tracking methodology and system hardware architecture to a functional prototype of a 6DOF magnetic tracking system with 2.6 mm static spatial accuracy, 5.4 mm dynamical spatial accuracy and 1.78 ° orientation accuracy within a 21 cm radius, BLE communication with a maximum measured latency of 150 ms, processing unit current consumption of 51.1 mA and a 0.54 cm^3 marker size.

A Figure Of Merit (FOM) was developed to compare the state-of-the-art magnetic tracking systems with our prototype. On this analysis, our system ranks only second w.r.t. only wireless magnetic tracking systems to the industry gold standard Polhemus G4 using deeply engineered micro-sensors.

This allows believing that with further system optimization our tracking methodology could replace the use of industry gold standard instruments for the development of low-cost medical instrumentation and research assessment tools with off-the-shelf components.

Acknowledgements

The completion of this work could have not been achieved without the help of my advisors PhD. Marco Crepaldi and Prof. Danilo Demarchi, thank you for the opportunity, guidance and support during these three years.

To PhD. Alessandro Sanginario, PhD. Paolo Motto Ros, PhD. Enrico Macrelli, PhD. Mariacarla Memeo and M.Sc. Cecilia Bosia, thank you for all your collaboration to this work.

A debt of gratitude is owed to the Istituto Italiano di Tecnologia and the Politecnico di Torino for supporting the development of this work.

To the friends that I have met along the way, my adopted family, thank you for the good times.

Last but not least I would like to thank my family, my parents Jhonny and Rosa, my sister Yani, none of this would have been possible without your love and support.

Contents

List of Tables

List of Figures

Abbreviations

2D Two-Dimensional.

3D Three-Dimensional.

6DOF Six Degrees of Freedom.

AHRS Attitude and Heading Reference Systems.

AOA Angle of Arrival.

AR Augmented Reality.

BLE Bluetooth Low Energy.

BPF Band-Pass Filter.

CF Complementary Filter.

DOF Degrees of Freedom.

EKF Extended Kalman Filter.

FEM Finite Element Methods.

FES Functional Electrical Stimulation.

FIR Finite Impulse Response.

FOM Figure Of Merit.

GLONASS Global Navigation Satellite System.

GPS Global Positioning System.

GRNN Generalized Regression Neural Network.

GTS Global Tracking System.

GUI Graphical User Interface.

HMI Human Machine Interface.

I2C Inter-Integrated Circuit.

IMU Inertial Measurement Unit.

ITS Indoor Tracking System.

KF Kalman Filter.

LOS Line of Sight.

LPF Low-Pass Filter.

LUT Look-Up Table.

MCU Microcontroller Unit.

MEMS Microelectromechanical Systems.

MLAT Multilateration.

NN Neural Network.

PDOA Phase Difference of Arrival.

PGA Programmable Gain Amplifier.

RAM Random Access Memory.

RF Radio-Frequency.

RMSE Root Mean Squared Error.

RSSI Received Signal Strength Indication.

sEMG Surface ElectroMyoGraphic.

SNR Signal-to-Noise Ratio.

SPI Serial Peripheral Interface.

TDOA Time Difference of Arrival.

TOA Time of Arrival.

TOF Time of Flight.

UART Universal Asynchronous Receiver Transmitter.

UKF Unscented Kalman Filter.

USB Universal Serial Bus.

UWB Ultra-wideband.

VR Virtual Reality.

WPS Wi-Fi Positioning Systems.

WTS Workspace Tracking System.

Chapter 1

Introduction

Tracking systems are an interesting and extensive field of research and development, with an ever-growing necessity of enhancing and surpassing the capabilities of existing systems.

Being able to understand, capture and quantify how an object moves and where it is located inside a determined space with a minimum expected accuracy can be considered both as key and limit to the development of a vast number of modern applications.

As an example, we can consider the constant necessity of capturing immersive human motion manifested in the entertainment industry, sports engineering and biomedical research. We can also take into account the need to capture how objects are manipulated in real-time, for example, surgical instrumentation, drones, airplanes and unmanned aerial vehicles.

The application domain of a tracking system depends on and is limited by the technologies and techniques that have been used for its implementation. Therefore, research can mainly focus on these two aspects to reach new results. We can innovate with new techniques expecting to reach bet-

ter characteristics with pre-existing technologies and produce a significant contribution to the field. Otherwise, we could experiment with new technologies, expecting to open new research possibilities to the field.

This thesis research work focused on the development of a low complexity algorithm for the development of a low-cost wearable magnetic tracking system for biomedical research applications. It is organized into five chapters.

The first chapter will introduce the reader to the thesis thematic. The second chapter will review the use of tracking systems for biomedical applications, determining which might be the best technology option for the development of a tracking intended to be used in the biomedical field. The third chapter will expose the work methodology we used for our system development, as well as the main testing procedures used. The fourth chapter will expose the complete development of our tracking system solution from its functioning proposal to a functional prototype, exposing as future work two new project proposals obtained due to the system characteristics. The fifth chapter will conclude the thesis by compiling all the observations we have obtained during our study.

In the following sections of this chapter, we will introduce basic concepts necessary to comprehend the notions behind most tracking systems. Then, we will classify tracking systems according to their main capabilities and the used technologies for their development. Finally, we will focus on introducing our application field of interest and we will discuss the applicability of the previously introduced types of tracking systems.

1.1 Basic Concepts and Terminology

In this section, we will introduce a set of concepts useful to set a basic knowledge of tracking systems and their operation.

We can start by defining the tracking systems as those systems capable of supplying the location, attitude or movement data of objects inside a determined space in a timely ordered manner or at the user request (UKEssays, 2018). These are also known as positioning systems.

The simplest form is a one-dimensional tracking system or ranging system that can be defined as a system able to measure the distance between two objects in just one direction. Similarly, Two-Dimensional (2D) and Three-Dimensional (3D) tracking systems are defined as those capable of determining the position of an object inside a 2D and 3D space.

Attitude and Heading Reference Systems (AHRS) are tracking systems capable of providing attitude information of the tracked object, mainly in the form of the Tait-Bryan angles roll, pitch and yaw (Bennet, 2020). And finally, Six Degrees of Freedom (6DOF) tracking systems are defined as those able to provide 3D position and attitude information about an object.

Time of Flight (TOF) is the measured time that a signal wave, particle or object takes to travel from a starting point to an endpoint. In energy wave propagation systems the emitter device is placed at the starting point and the receiver device at the endpoint (Terabee, 2020). Then, the TOF is used either to measure the wave velocity in the medium v or the path's length or range r using (1.1),

$$TOF = \frac{r}{v}. \tag{1.1}$$

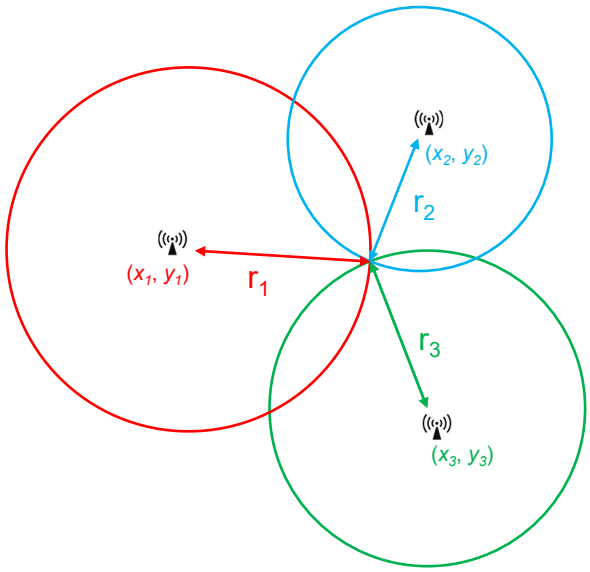

Figure 1.1: True-range multilateration. The position of a device can be determined by using the known ranges r_1, r_2 and r_3

Time Difference of Arrival (TDOA) can refer to the measured time delay between the Time of Arrival (TOA) of two signal waves emitted simultaneously from different points to a single receiver, or to the measured time delay between the arrival of a wave originated by single emitter to two different receivers (Seuté et al., 2016). Similarly Phase Difference of Arrival (PDOA) is the measured phase between the signal wave arrival to two different and closely positioned receivers. TDOA is used to estimate the range difference from two points parting from Eq. (1.2),

$$TDOA = \frac{r_1 - r_2}{v}. \tag{1.2}$$

These measurements and distance estimation techniques allow us to introduce Multilateration (MLAT) techniques, which are among the most common position estimation techniques for tracking systems.

True-range MLAT is based on determining the tracked object 2D or 3D position by measuring distances between the tracked object and at least

two or three nonaligned known position points correspondingly, and then intersecting the circumferences or spheres formed around the known points with the measured distances, as shown in Fig. 1.1. To measure said distances, the TOF of a wave traveling from the tracked object to multiple antennas located at the know position points might be used.

Pseudo-range MLAT, or also called hyperbolic positioning is based on using TDOA of a wave emitted from the tracked object to two different receivers (Wong et al., 2017). Parting from Eq. (1.2) and the assumption of two receivers separated by a distance d placed at the coordinate points $\vec{P_1} = [\frac{-d}{2}, 0, 0]$ and $\vec{P_2} = [\frac{-d}{2}, 0, 0]$, we can arrive to the expression shown by Eq. (1.3), and with some algebraic arrangement obtain the two-sheeted hyperbola expressed by Eq. (1.4),

$$r_1 - r_2 = \Delta r_{12} = \sqrt{(X + \frac{d}{2})^2 + Y^2} - \sqrt{(X - \frac{d}{2})^2 + Y^2} \tag{1.3}$$

$$\frac{X^2}{\Delta r_{12}^2/4} - \frac{Y^2}{d^2/4 - \Delta r_{12}^2/4} = 1. \tag{1.4}$$

Implementing the same case in 3D we will arrive to define a two-sheeted hyperboloid of the emitter possible positions. Adding a third receiver will define another hyperboloid, and intersecting them would reduce the possible positions to a curve. Finally, adding a fourth receiver will reduce the possible positions to one or two points.

Angle of Arrival (AOA) is another tracking technique that consists in calculating the direction from which a wave arrive to a group of receiver antennas from the measured TDOA or PDOA as shown by Dotlic et al. (2017). In its simplest form, the path difference p of the wave arriving to two antennas separated by a distance d is related to the AOA θ as shown by Eq. (1.5). Considering the signal wavelength λ, the PDOA is expressed as Eq. (1.6).

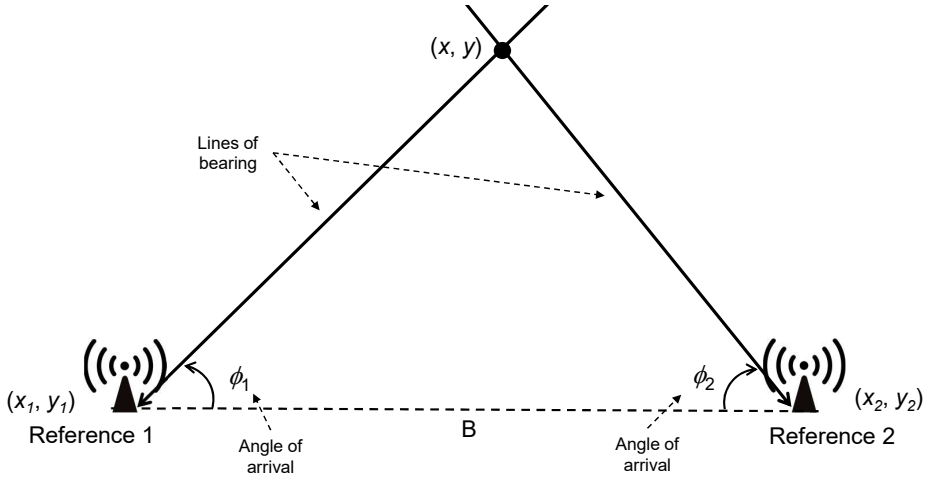

Figure 1.2: Triangulation technique based on measured angle of arrival for position estimation. The lines of bearing parting from two references with known location intersect at the position of the emitter.

Therefore, the AOA can be expressed as Eq. (1.7).

$$p = d \sin\theta \tag{1.5}$$

$$\alpha = \frac{2\pi}{\lambda} p \tag{1.6}$$

$$\theta = \arcsin \frac{\alpha\lambda}{2\pi d} \tag{1.7}$$

Then, having multiple groups of receivers in known locations allow us to intersect the lines of arrival to estimate the emitter 2D or 3D position depending on the complexity of the system, as shown in Fig. 1.2. This tracking technique is known as Triangulation.

Modern and more complex tracking systems are based on the use of Kalman Filter (KF) which is a linear quadratic estimation algorithm that estimates internal states of a linear dynamical system by using a series of measure-

ments taken over time, including statistical noise and expected inaccuracies (Kim and Bang, 2018).

Tracking systems based on non-linear dynamical systems can also use extensions and generalizations of the KF method as the Extended Kalman Filter (EKF), which uses the Jacobian to linearize the differentiable systems around the current estimated state, and the Unscented Kalman Filter (UKF) based on the unscented transformation.

Complementary Filter (CF) is another estimation technique based on using multiple physical sensors with different frequency-dependent signal qualities, filtering the sensor signals to their usable frequency range as a way to complement each other usability inside a closed-loop control algorithm (Colton and Mentor, 2007). It is mainly used in modern low-cost multiple sensor-based AHRS due to its low computational cost.

1.2 Tracking Systems Classification

In this section, we classify the different types of tracking systems we can find in the literature. First, we classify them according to the range and accuracy these systems can provide. These characteristics are the main limiting points for a system to be used for a determined application. Then, we classify tracking systems by the technology and techniques used for their development, explaining also the main differences between them.

This classification will help us set a basic understanding of the state-of-art and later discern which types of tracking systems suit better the application set of our interest.

1.2.1 Accuracy and Range-based Classification

Global Tracking System (GTS) are defined by their capability of determining the position and sometimes the attitude orientation of objects around the globe. The majority of these systems are designed to calculate the position of devices within a 2D plane defined by global coordinates and their altitude with an accuracy of a few meters. Through the most popular of these system we can find Global Positioning System (GPS), Global Navigation Satellite System (GLONASS) and Galileo (Grewal et al., 2007). Their most common use is providing commercial devices positioning, navigation and timing information.

Earlier versions of global positioning systems were based pseudo-range MLAT due to the feasibility of using the TDOA with available technology (Uttam and D'Appolito, 1975). Current systems use true-range MLAT instead, because of the satellite's capability of broadcasting their ephemeris and intrinsic clock bias, as well as major computational capabilities of receiver devices (Lechner and Baumann, 2000).

More complex and application-driven systems, such as aircraft trackers, combine global tracking systems with altitude measurement sensors and AHRS as to provide a full 6DOF earth referenced real-time tracking system.

GTS heavily depend on a clear Line of Sight (LOS) between the tracked device and the referenced placed broadcasters. Their accuracy can even be augmented by using a well-placed stationary receiver to compare the broadcasters' data. This is called differential GPS. In the absence of both LOS and the aid of correction or augmentation systems, for example inside of an industrial building with poor mobile connectivity, the accuracy of global tracking systems tends to drop to unusable levels. This motivated

the development of Indoor Tracking System (ITS).

ITS are defined by their capability of determining the real-time position and sometimes the attitude orientation of one or several objects within a predetermined space inside building (Curran et al., 2011). They can go from simple systems installed inside a single room to more elaborated installations capable of covering a whole building complex.

Their accuracy can range from a few meters to centimeter-level accuracy. In their simplest form, the system can determine in which zone or room of a building several objects with Radio-Frequency (RF) identifications tags are located. More complex systems can use the perceived RF signal strength to determine the range between the tracked object and multiple wireless anchors and employ true-range MLAT (Montaser and Moselhi, 2014). Other examples of ITS determine AOA of the RF signal from several anchors within a single room to calculate more accurately the tracked object position (Dotlic et al., 2017). Some ITS are also combined with AHRS systems to fully provide a 6DOF ITS.

ITS applications range from commercial devices and inventory tracking to more innovative fields as robotic guidance and automated drone indoor and underground navigation.

Workspace Tracking System (WTS) have been developed for more immersive interactive applications requiring more accuracy. We can define WTS as those systems capable of determining one or several objects' position and in some cases their attitude orientation, within a determined space ranging from few cubic centimeters to a couple of cubic meters with accuracy that ranges from centimeter to sub-millimeter level.

WTS applicability is vast, we can mention from their entertainment in-

dustry use, such as cinematic motion capture systems, Augmented Reality (AR) and Virtual Reality (VR) systems (Baldi et al., 2017), to more scientific research applications, such as medical instrumentation guidance and imaging systems (Lee et al., 2015), sport and bio-performance analysis, and neuroscience research (Memeo and Brayda, 2016). For these kinds of systems, most RF signal-based techniques do not provide enough precision. Therefore, alternative technology solutions have been found.

1.2.2 Technology Based Classification

Now we will classify tracking systems according to the most common technologies we found in the literature to develop such systems. Moreover, we will briefly introduce each type of system's main characteristics and how they work.

Then, we will start with one of the most basic and historically used tracking techniques, radar tracking. It is based on measuring the TOF and AOA a RF signal emitted and perceived by the radar after bouncing back from perceived objects in a determined space. Radar tracking has been widely used in the past to track ships and aircraft from a stationary base and onboard for ships and aircraft navigation. Today this technique is also used in robotics navigation by changing the RF signals by ultrasound or light waves (De Angelis et al., 2017).

RF network-based tracking systems determine the position of a device connected to the network by using MLAT techniques and network information such as Received Signal Strength Indication (RSSI) between the device and multiple network antennas or TOF of beacon signals travelling from the device to the antennas (Montaser and Moselhi, 2014).

These systems were widely used to determine the position of mobile phones and aircraft before the widespread availability of satellite tracking systems. For mobile tracking, the accuracy of these systems can go down to 50 m urban areas with high mobile traffic and antenna towers density.

Satellite tracking systems determine the position of devices around the globe by using true-range MLAT and broadcast signals TOF from at least three (at sea level) or four satellites (for 3D position) to the tracked device (Lechner and Baumann, 2000). This is possible due to the capability of satellites of calculating and broadcasting their ephemeris and signal transmitting time.

Satellite tracking system is the most used solution for 3D GTS. Since they are heavily dependent on LOS between the satellites and the tracked device, their accuracy drops indoors and in obstructed environments. Therefore, augmentation system techniques such as Assisted GPS, Differential GPS and Wide Area Differential GPS, have been developed.

Wi-Fi tracking systems or Wi-Fi Positioning Systems (WPS) are ITS that can determine the position of a device connected or registered in a Wi-Fi network by calculating the distance to multiple access points from their RSSI or signal TOF and MLAT techniques, or by using the signal AOA and triangulation techniques. WPS can achieve decameter level and meter level accuracy depending on the used technique and the number of close access points whose positions have been registered into the database (Mohd et al., 2017).

WPS have become important for augmented reality, health care monitoring, personal tracking and wireless security applications due to the low price and presence of Wi-Fi network interface cards in most commercial devices.

Bluetooth Low Energy (BLE) beacon tracking systems are based on using fixed BLE beacons broadcasting their universally unique identifier and indoor position to be perceived by compatible software as for the device to know when it is in proximity to a specific beacon (Mackey et al., 2020). A more complex 2D ITS can be developed using the RSSI to range the distance between the tracked device and fixed beacon and with true-range MLAT estimate its 2D position. These systems can achieve up to 1 m accuracy and have been in development during the last years, focusing on mobile marketing and location-based actions.

Ultra-wideband (UWB) is a pulse-based low energy radio technology used for large bandwidth short-ranged communications. In the last years it has been a very developing technology and one of its many applications are the UWB tracking systems. Due the accurate timing capabilities of the UWB technology different tracking techniques have been implemented to develop ITS including pseudo-range MLAT from TDOA measurements, AOA and triangulation from PDOA measurements, and true-range MLAT from TOF measurements using UWB transmission capabilities to broadcast the signal transmitting time (Alarifi et al., 2016).

UWB ITS have become of importance because they can achieve decimeter and centimeter-level accuracy, but since the required hardware has not been widely implemented in commercial devices, the use of UWB tracking systems has been mainly focused in industrial applications.

An Inertial Measurement Unit (IMU) is an electronic device capable of estimating specific forces, angular rotations and sometimes earth referenced orientation of an object by combining a set of accelerometers, gyroscopes and sometimes magnetic sensors. IMU based AHRS use these sensors data and KF or CF based algorithms to estimate the system earth referenced

orientation. Also, a self-contained 6DOF tracking system can be developed using accelerometer sensor information, AHRS estimation and zero velocity update based algorithms.

Due to the feasibility of developing IMU with Microelectromechanical Systems (MEMS) sensors, IMU based AHRS are widely implemented in smart industrial, robotic, biomedical and commercial devices applications. They can also be incorporated into pre-existing 3D tracking systems to enhance their capabilities.

Optical tracking systems are based on using an arrangement of multiple cameras (being the stereo-camera the simplest arrange) to track specific points. These points can be either retro-reflective markers, active infrared markers (Schneider et al., 2020) or specific objects that the system can recognize through deep learning algorithms, such as human joints or fingers (Cordella et al., 2012). The point image position in the 2D image plane of each camera is used to calculate the AOA of the light waves and along with the position information of each camera and triangulation techniques, the relative 3D position of the object can be calculated.

Optical tracking systems are amongst the most accurate tracking systems, able to track multiple objects with centimeter and millimeter level accuracy. But the accuracy and range that these systems are capable of achieving are directly related to the number of cameras used, sometimes requiring a large room level installation, and the presence of LOS between the tracked object and at least two cameras.

Magnetic tracking systems exploit the strong relationship between the magnetic flux density (B-field) perceived by a magnetic sensor and the sensor position and orientation relative to the magnetic field source.

This relationship allows that small changes of the sensor position and orientation to translate into significant changes in the measured $\vec{B}$. Therefore, it enables the development of WTS with millimeter and sub-millimeter level accuracy.

Said relationship can be expressed by a mathematical model in the form of $\vec{B}(\vec{P}, q)$, where $\vec{P}$ is the sensor position and q expresses the sensor relative orientation in form of a quaternion. Along with the B-field model, a non-linear regression method is needed to perform the position and orientation estimation of the tracked sensor.

Along with very high accuracy, a great advantage of these systems is that they do not depend on a LOS between the magnetic field source and the sensors, as long as no ferromagnetic materials or other unexpected magnetic field sources are present in the tracking space. Said characteristics make magnetic tracking systems a viable solution for medical instrumentation (Condino et al., 2012), gait analysis (Romero et al., 2017) and VR entertainment systems development.

1.3 Tracking Systems for Biomedical Research

In this section, we will briefly introduce what is known as biomedical engineering, which are the main biomedical application areas where tracking systems can be used. Then, we briefly discuss which sectors we intend to focus on. And finally, we discuss what kind of tracking systems are the most indicated to be used in our field of interest.

Biomedical engineering is the scientific field that focuses on combining technical engineering design and problem-solving principles with medical bio-

logical scientific knowledge to solve healthcare treatment problems. It is an evolving sector due to society's general advance towards everyday use of engineered equipment and technology in all aspects of life, including medical diagnosis, monitoring, and therapy (Enderle, 2012).

Biomedical engineering is a broad research and development field involving different areas of focus such as design and development of active and passive medical devices; biomedical signal processing; biomaterials; computational biology; cellular, tissue and genetic engineering; medical imaging; orthopedic bioengineering and bionanotechnology.

Tracking systems have been widely used in biomedical engineering applications. Their involvement can be seen in the development of medical imaging (Punithakumar et al., 2016; Esaote, 2015) and surgical instrumentation (Franz et al., 2014), either as part of the system and as a measurement tool for its validation. Moreover, they also have been used as a direct measurement tool for diagnostics as in gait analysis (Klöpfer-Krämer et al., 2020), and during therapy as in muscular functional electrical stimulation (Chen et al., 2013).

Another example of tracking systems utility in the biomedical field is their incorporation into assessment tools for medical training instruments (Hamza-Lup et al., 2018). And more novel applications of tracking systems can be found in telemedicine, where the patients' posture needs to be tracked (Gürkan, 2020) or position inside their homes or specialized facilities monitor their physical activities (Mason et al., 2014) or located in case of an emergency.

A particular goal of high interest and not only for the biomedical sector is the robust and accurate tracking of human fingers. It would not only allow gait analysis systems for the diagnostic motor diseases (Tran et al.,

2018; Cordella et al., 2012), provide the tools for long-distance immersive control of surgical instrumentation (Kim et al., 2014), or provide a robust measurement unit for neuroscience research on human motion (Ansuini et al., 2014), but it would also allow the development of endless commercial and industrial applications.

To be noticed is that the totality of the cited examples does not involve the use of GTS. In fact, the majority of these examples use WTS because a critical characteristic of these applications is the need for a very accurate, from a couple of centimeters to millimeter-level accuracy and below. Meanwhile, a range longer than a couple of meters or a room installation is not necessary. Some specific cases make use of ITS to track the patient and devices inside a building.

We can notice that the development of medical instruments, either surgical, medical imaging or medical training instrumentation, requires the use of a tracking system with the highest accuracy possible, due to the critical aspect of these kinds of applications. Therefore, the type of technology implemented for the tracking system depends on other application constraints such as a constant obstruction of LOS or the presence of magnetic interference. Meanwhile, applications that focus on human motion tracking, allow the use of less accurate and more experimental tracking systems, searching for other qualities such as wearability, wireless system and low system cost.

In particular, it is in our interest as a research group to achieve a general solution that can be implemented and adapted to diverse biomedical projects developed inside the Politecnico di Torino and Istituto Italiano di Tecnologia. The research area of these projects covers medical rehabilitation and neuroscience studies, and in more detail, we can enclose the application area to upper limb motion tracking, hand fingers motion tracking and medical

instrumentation tracking.

For example, Sapienza et al. (2018) shows a low-power device that quantifies the muscular activity through event-driven Surface ElectroMyoGraphic (sEMG) signals capturing and one of its rehabilitation focused applications is Functional Electrical Stimulation (FES), where the trainer muscular activity would be captured and the patient muscles would be stimulated to imitate the trainer's movement. A wearable tracking system would allow assessing and comparing the patient's limb's movement.

The work presented by Ansuini et al. (2014) is a social cognition study with the idea of understanding the link between a subject's intention and the visible movement. For this study, upper limbs and finger movement were captured using VICON motion tracking system. Therefore, in this case, substituting the high-end tracking system with a lower cost and portable system with a comparable accuracy would allow much more flexibility for replications and extensions of this study.

An example of medical instrumentation tracking can be found in the work published by Memeo and Brayda (2016), where a mouse-shaped device with a 3DOF actuator changes the elevation and orientation of a plate according to the device position to simulate diverse surfaces and help develop mental maps to sight-impaired patients. In this system, the 2D position of the device is determined by a tactile tablet which grants great accuracy but limits the usable range and DOF. Substituting such a tablet with a 6DOF wireless tracking system would allow overcoming such limitations and enhancing the functionalities of the device.

Another example of medical instrumentation tracking is shown in Esaote (2015), where multiple ultrasound probes positions are tracked in order to correlate them with the perceived ultrasound images and generate a 3D

render. For this purpose, the NDI high-end magnetic tracking systems are used, which implies high implementation costs and leaves room for the development of lower-cost tracking systems to the fusion imaging system to become more accessible.

This range of applications allows us to enclose the following general set of characteristics of a tracking system suitable for biomedical applications: high accuracy, characteristic that depends directly on the implementation and we aim for values at millimeter or submillimeter level; 6DOF tracking capability; wearable and low weight, especially when used for human motion capture; wireless tracked markers, which can be seen as a plus, but as in most electronic devices, it would increase the system ease of use; and finally low system cost, characteristic that would allow the tracking system implementation and integration to market available medical devices.

From this, we can conclude that the most suitable technologies to develop a tracking system for biomedical applications are optical and magnetic tracking systems. This could be extended to IMU based tracking system in the case of gait analysis applications and UWB tracking system for applications requiring ITS. However, the accuracy provided by magnetic and optical tracking systems can not be matched by other technologies. Each one of these offers different advantages over the other, for example, optical tracking can provide a longer range for multiple wireless markers, while magnetic tracking solutions offer higher accuracy without depending on a LOS or a room level installation.

Therefore, in the next chapter, we will evaluate more in-depth the state-of-the-art of both of these technologies applied in the biomedical field to explore which could be our contribution to this field.

Chapter 2

Problem Statement and Related Literature

In the previous chapter, we introduced a general set of characteristics for a tracking system suitable for biomedical applications, focusing on upper limb motion tracking, hand fingers motion tracking and medical instrumentation tracking. These characteristics can be pointed as follows:

- 6DOF tracking capabilities.
- High spatial accuracy, from millimeter to submillimeter level.
- Wearable, wireless and low weight tracked markers.
- Low-cost system in comparison to commercially available solutions.

The finality of this study is to set the base for the development of a system accurate and flexible enough to be used in a variety of biomedical applications ranging from medical instrumentation to human limb tracking. Furthermore, having a low-cost implementation would allow the replacement of the goal standard high-cost system on research studies and

therefore increasing the research findings and scientific production, while at the same time allowing the involvement of institutes with no access to the goal standard systems.

In the following sections, we will evaluate the most suitable technologies for developing a tracking system with these characteristics for biomedical applications. Moreover, a literature review is necessary to set specific system design constrains values parting from the defined general characteristics.

As concluded in the last chapter, optical tracking systems and magnetic tracking systems are the best options due to their expected performances. We will also consider IMU based tracking system as a third option since they are continuously used as wearable devices in literature due to their low cost.

For this, we will introduce again and in more detail how each tracking system technique works. Then we will use literature to compare their usability in biomedical applications, we will extract their strength and weak points and from this, we will choose the technology from which we will start designing and developing our tracking system.

Finally, the state-of-the-art literature of the chosen technology will be further evaluated to determine which are the weak points and which can be the contributes of our new system.

Contents

2.1 Tracking System Technologies Comparison in Biomedical Research

In this section, we will compare the magnetic, optical and IMU-based tracking systems according to the use they have been commonly given inside the biomedical field. We will firstly introduce more in-depth how these tracking system technologies function to understand better their strength and weaknesses. Then using 45 different examples, we will compare in which applications each technology is more prone to be used.

As described in the previous chapter, magnetic tracking systems exploit the strong relationship between the magnetic flux density (B-field) perceived by a magnetic sensor and the sensor position $\vec{P}$ and orientation relative to the magnetic field source. This relationship is commonly expressed by a mathematical model in the form of $\vec{B} = f(\vec{P}, q)$, where q expresses the sensor relative orientation in form of a quaternion.

For 6DOF and 3D tracking systems, it is common to use triaxial magnetic sensors to capture the generated B-field, and in most cases, three perpendicular coils are used as the source to produce three controlled magnetic fields at different frequencies. Then, the chosen mathematical model of the magnetic flux density is used to extract the relative sensor position $\vec{P}$ and relative orientation q employing a non-linear regression method.

$$\vec{B} = \frac{\mu_0 M_T}{4\pi} \left(\frac{3\left(\vec{O} \cdot \vec{P}\right)\vec{P}}{R^5} - \frac{\vec{O}}{R^3} \right) \tag{2.1}$$

A commonly used model is the magnetic dipole model, as expressed in Eq. (2.1) and shown in Fig. 2.1. It describes the sensed B-field at point $\vec{P}$ with respect to the source of the magnetic dipole moment $M_T = NSI$, where

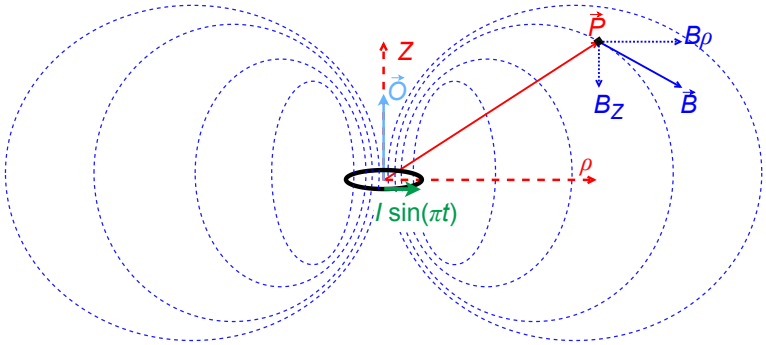

Figure 2.1: Magnetic flux density lines of a magnetic dipole created by a current loop around the Z axis. ©[2020] IEEE.

N the current loop turns number, S is the loop area and I the current magnitude, $R = \|\vec{P}\|$, and μ_0 is the vacuum permittivity. In this model, $\vec{O}$ is the unit vector that signals the orientation of the magnetic dipole north pole and it is used to express the relative orientation between the sensor and the magnetic source. The magnetic dipole is of common use because it remains valid for implementations where the sensor to bobbin distance is greater than four times the current loop radius, as stated by Raab et al. (1979).

Optical tracking is based on using multiple camera arrangements to track specific objects, being a stereo camera the simplest arrangement. These objects can be either retro-reflective markers, active infrared markers or specific objects that the system can recognize through deep learning algorithms, such as human joints or finger articulations.

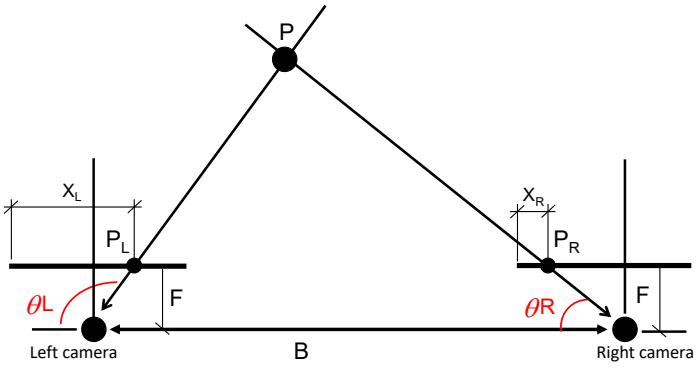

Figure 2.2: Stereo camera position determination with AOA

As shown in Fig 2.2 to estimate the object position, the AOA of the light wave travelling from the object to each camera needs to be calculated. This is done by translating the captured object image position, X_L in the case of the left camera, into horizontal plane AOA θ_L employing a previously known function $\theta_L = f(X_L)$ that depends on the camera physical characteristics. The same procedure applies for the vertical plane AOA. Then knowing each camera's absolute position and orientation, the lines of bearing can be intersected as shown in Fig 2.2 to determine the object 3D position.

As previously stated IMU are electronic devices with a set of sensors capable of measuring proper acceleration, angular rotational speed and magnetic flux density. IMU based tracking systems use these sensor measurements to estimate the device earth referenced orientation and rotation through a AHRS algorithm. The AHRS algorithms are usually based on regression algorithms such as KF, EKF and CF.

A 6DOF tracking system can be developed using accelerometer sensor information, AHRS estimation and zero velocity update based algorithms, to calculate the 3D displacement of the IMU. Other works place multiple IMU in a known position of the body and by comparing the estimated orientation of each sensor and how they are oriented relative to each other, the skeletal motion of the body can be tracked.

In order to determine in which kind of scenario each technology is more prone to be used inside the biomedical field, we extracted from literature 45 different works, 15 for each technology, and classify them in for types of applications: human posture tracking, human motion tracking, finger motion tracking and medical instrumentation tracking.

Human posture tracking refers to those works focused on measuring only

the orientation, and not the position or displacement, of specific body parts to perform posture studies or gait analysis during an activity.

Human motion tracking refers to those works focused on tracking the position and orientation of body parts, human manipulated objects or a person as a whole.

We leave as a separate classification those studies focused on tracking the motion of hand and fingers, as these systems require higher accuracy and to deal with more specific problems and, as stated in the previous chapter, it is not only of high interest for the biomedical field but also for commercial and industrial applications.

And finally, medical instrumentation tracking refers to those works incorporating tracking systems with surgical and medical imaging instruments, as they require the highest accuracy and robustness available.

These classification groups were also thought in the sense that, given certain limitations, a tracking system employed for medical instrumentation tracking, could also be adapted to be implemented for finger motion tracking, and a system employed in finger motion tracking could be adapted for human motion tracking and so on.

2.1.1 Magnetic Tracking Systems

Tab. 2.1 refers to the selected works using magnetic tracking systems. It can be seen that the vast majority of these examples are employed in medical instrumentation tracking, while a few are employed in finger motion tracking and just a couple for human motion tracking.

In particular, we found that Condino et al. (2012); Lund et al. (2017);

Table 2.1: Aim typology of research studies using magnetic tracking systems

Research Target	**Referenced studies**
Medical Instrumentation Tracking	Lee et al. (2015); Condino et al. (2012); Lund et al. (2017); Xu et al. (2012); Schwein et al. (2017); Esaote (2015); Aufdenblatten and Altermatt (2008); Atuegwu and Galloway (2008); Doering et al. (2015)
Finger Motion Tracking	Huang et al. (2016); Parizi et al. (2019); Chen et al. (2016); Polhemus (2017)
Human Motion Tracking	Romero et al. (2017); Lockery et al. (2011)
Human Posture Tracking	N.R.

N.R. = No research found.

Schwein et al. (2017); Aufdenblatten and Altermatt (2008); Doering et al. (2015); Atuegwu and Galloway (2008) focused on tracking catheter tips and guidewires for endovascular, endoscopic and intraventricular interventions. Meanwhile Lee et al. (2015); Xu et al. (2012); Esaote (2015) focused on tracking the ultrasound probes position and orientation during 3D ultrasound imaging procedures.

The works exposed by Polhemus (2017); Huang et al. (2016); Chen et al. (2013) show the magnetic tracking system utility in determining the position and orientation of multiple fingers. Huang et al. (2016) in particular can be implemented for both finger and human manipulated objects tracking inside a predetermined space. Parizi et al. (2019) implements the orientation tracking for a single finger as a Human Machine Interface (HMI) device.

The magnetic systems have shown also their utility as a human motion tracking system by Romero et al. (2017), where the Polhemus system is used as a reference for limb and body motion tracking, and by Lockery et al. (2011) where objects manipulated by patients are tracked.

Table 2.2: Aim typology of research studies using optical tracking systems

Research Target	**Referenced studies**
Medical Instrumentation Tracking	Punithakumar et al. (2016); Engelhardt et al. (2016); Lin et al. (2015)
Finger Motion Tracking	Schneider et al. (2020); Tran et al. (2018); Kim et al. (2014); Hsu et al. (2014); Cordella et al. (2012); Ansuini et al. (2014); MacRitchie and McPherson (2015)
Human Motion Tracking	Carse et al. (2013); Armand et al. (2014); Chen et al. (2013)
Human Posture Tracking	Klöpfer-Krämer et al. (2020); Ong et al. (2017)

We can see that the robustness and accuracy of magnetic tracking systems, in particular the capability of tracking without a LOS, facilitate their integration in very critical applications.

As a weak point, we can find that most of these systems are limited to a short-range, therefore human motion tracking is also limited. Moreover, most of these systems require a wire from the sensor to the central system, limiting their use of a wearable device. The few exceptions to this last statement can be found in the research works by Huang et al. (2016); Parizi et al. (2019).

2.1.2 Optical Tracking Systems

Tab. 2.2 refers to the selected works using optical tracking systems. It can be seen the versatility of the use of optical systems. Being an area of high interest the majority of these examples are employed in finger motion tracking. Due to the high accuracy of these systems they can be adapted to surgical and medical imaging instrumentation. Due to the extended range of these systems, they are highly implemented in human motion tracking. Some low-cost optical systems can be also used for simple human posture

tracking.

In particular, Punithakumar et al. (2016); Lin et al. (2015) used optical markers to track the patient respiratory phases and torso movement, Punithakumar et al. for 3D ultrasound imaging and Lin et al. for liver intervention. Engelhardt et al. (2016) demonstrated the feasibility of use of optical markers adapted to mitral valve surgery instrumentation.

Tran et al. (2018); Cordella et al. (2012) use a low-cost optical tracking system (Microsoft Kinect) with optical markers attached to the patient's hand to evaluate the ability to manipulate an object or perform predetermined movements, Tran et al. focus particularly on cerebellar ataxia assessment. Ansuini et al. (2014) used a Vicon system installation for neuroscience research to quantify the arm and hand movements of the study participants at the time of manipulating objects. Schneider et al. (2020) evaluates the accuracy of markerless low-cost optical systems (Leap Motion and VIVE Pro) against a high-end optical tracking system (Optitrack) for head-mounted hand tracking. Kim et al. (2014) evaluates the use of markerless low-cost optical tracking systems (Leap Motion and Kinect) for their use in teleoperations surgical task, concluding that their accuracy is not good enough for this critical application. Hsu et al. (2014) perform finger tracking with a low-cost markerless system for real-time virtual instrument playing, which a less critical but equally demanding application. MacRitchie and McPherson (2015) integrates the use of a camera with touch sensors for evaluating the subject performance playing piano by correlating the finger positions with the piano key touching events, creating a mixed hand tracking system.

Carse et al. (2013) assess the performance of high-end optical tracking systems (Vicon and Optitrack) for a more affordable clinical gait analysis solution. Armand et al. (2014) evaluates Vicon markers' placement on the

Table 2.3: Aim typology of research studies using IMU-based tracking systems

Research Target	**Referenced studies**
Medical Instrumentation Tracking	N.R.
Finger Motion Tracking	Baldi et al. (2017); Bellitti et al. (2020); Salchow-Hömmen et al. (2019)
Human Motion Tracking	Pereira (2016); Valldeperes et al. (2019); Weenk et al. (2014); Eikerling et al. (2017); Arachchi et al. (2016); Yang et al. (2017); Roetenberg et al. (2009)
Human Posture Tracking	Perez et al. (2019); Li et al. (2016); Lebel et al. (2016); Gürkan (2020); Zügner et al. (2019)

N.R. = No research found.

thorax for clinical gait analysis. Chen et al. (2013) quantifies anterior tibial translation during FES in dynamic knee extension exercises by tracking specific colored markers with a single camera.

Klöpfer-Krämer et al. (2020) exposes the possibility of using a marker-based and markerless optical system for gait analysis and Ong et al. (2017) assets the use of a low-cost markerless optical system for gait analysis.

We can conclude that for clinical evaluations of human motion, hand finger and medical instrumentation tracking, high-end optical systems are very well established. The research focuses primarily on using low-cost devices for clinical applications as an alternative, finding difficulties in establishing their use for critical applications such as hand and medical instrumentation tracking for clinical applications.

2.1.3 IMU-based Tracking Systems

Tab. 2.3 refers to the selected works using IMU-based tracking systems. We can observe that the majority of these examples focus on wearable solutions

for human motion and human posture tracking systems. No solutions were found for critical applications and just a few are found for finger and hand motion tracking.

In particular, Baldi et al. (2017); Salchow-Hömmen et al. (2019) use the orientation estimated from measurements of multiple IMU placed in the fingers and back of the hand to estimate hand motion and gestures for clinical applications and cutaneous feedback. Bellitti et al. (2020) combined IMU measurements and stretch sensors to estimate hand gestures.

Roetenberg et al. (2009) combine the measurements of several IMU positioned along the body to estimate the skeleton posture, motion and position with 2% error of the travelled distance. Arachchi et al. (2016) also combines multiple IMU sensor measurement for skeleton motion tracking. Pereira (2016) combine 3 IMU sensors for upper limb motion tracking. Weenk et al. (2014); Yang et al. (2017) combine IMU measurements with other sensors for novel zero velocity update algorithms in order to track pedestrian motion. Eikerling et al. (2017) compare IMU-based tracking with low-cost optical tracking for gait analysis, particularly the center of mass displacement.

Lebel et al. (2016) use IMU for estimating the multiple angles of the skeleton. Zügner et al. (2019); Li et al. (2016) use IMU to estimate the joint angles of lower limb extremities. Perez et al. (2019) focused on using IMU to estimate upper limb joint angles. Gürkan (2020) designed a wireless system with IMU to estimate the torso and head postures.

We can conclude that low-cost IMU sensors-based tracking systems are a very well-established solution for AHRS. Currently, there exist few commercially available solutions. The vast majority of solutions are research-based and it is focused on designing a wearable system with multiple sensors po-

Table 2.4: Commercial magnetic tracking gold standard systems characteristics

System	**Accuracy** (mm) (∘)	**Range** (cm)	**Update Rate** (Hz)	**Wireless Feature**
Patriot (Polhemus, 2021b)	1.524 0.4	91.44	60	No
Patriot Wireless (Polhemus, 2021c)	7.5 1	76.2	50	Yes
G4 (Polhemus, 2021a)	2 0.5	100	120	Yes
TrakSTAR (NDI, 2021c)	1.4 0.5	66	255	No
Aurora (NDI, 2021b)	0.88 0.48	50	40	No

sitioned along the body to estimate limb joint angles and even skeleton motion and posture.

Research also focuses on fusing IMU with other low-cost sensors for pedestrian motion and hand finger motion tracking. However, IMU-based tracking is limited to centimeter-level position accuracy and depends highly on the employed algorithm.

2.1.4 Commercially available tracking systems comparison

In order to understand more quantitatively the difference between these technologies, we can refer to Tab. 2.4 and Tab. 2.5. These tables reflect the expected system characteristics of a few examples of commercially available devices for magnetic and optical tracking systems. IMU-based tracking systems are mostly research-based and depend mainly on the implemented algorithm, or an example of commercially available we can refer to Roetenberg et al. (2009) that register the IMU-based tracking accuracy

Table 2.5: Commercial optical tracking gold standard systems characteristics

System	**Accuracy** (mm)	**Range** (cm)	**Update Rate** (Hz)	**Markerless Feature**
Vicon (VICON, 2021)	0.017	-	200	No
Optitrack Prime 22 (Optitrack, 2021)	0.15	300	360	No
Polaris Vega XT (NDI, 2021a)	0.15	300	250	No
Leap Motion Controller (Weichert et al. 2013)	1.2	60	200	Yes
Kinect (Khoshelham and Elberink, 2012)	40	500	30	Yes

as a 2% of the travelled distance.

We can observe that commercial magnetic systems are inherently 6DOF tracking systems, meaning that they can estimate both the position and orientation of a single sensor. Most of them have millimeter level accuracy and a few of them have sub-millimeter level accuracy, and for orientation estimation, the accuracy is sub-degree level accuracy. Their working range goes from a minimum of 50 cm to a maximum of 3 m.

The strongest point of these systems is their ability to function robustly without requiring a LOS, making them highly demanded for medical instrumentation, hand and finger tracking. However, the majority of these systems, with few exceptions, require their sensor to be wired to the central system, limiting the wearability and ease of use for some applications involving human motion or human manipulated object motion.

On the other hand, given a clear LOS, high-end optical tracking systems

have a far higher spatial accuracy and can track multiple markers at a high update rate in order to track with 6DOF objects with multiple markers attached to them.

The main weak point of these systems is the requirement of this clear LOS between all the markers and at least two cameras, which is solved by using a multiple cameras installation surrounding the best way possible the tracking space. This of course has a high economic cost, which might be suitable only for surgical and similarly critical high-income applications, while low-cost markerless systems are suitable for limited applications.

As previously stated, IMU-based tracking systems are a very well-established solution for AHRS tracking. However, few commercial systems are available for IMU-based motion tracking and they are limited to centimeter-level accuracy which is incremental and reported as 2% of the travelled distance (Roetenberg et al., 2009). This makes IMU-based systems not suitable for position tracking on critical biomedical applications.

2.1.5 Conclusions

As previously stated, our main interests rely on designing a system able to perform accurate and reliable 6DOF tracking. Such system should also be flexible enough to be used on critical applications such as medical imaging instrument tracking as in Esaote (2015); Lee et al. (2015); Xu et al. (2012), hand finger tracking for clinical assessment as in Tran et al. (2018); Cordella et al. (2012) or as a research assessment tool for works such as Ansuini et al. (2014); Memeo and Brayda (2016), while maintaining a low implementation cost. Including wearable and wireless characteristics will increase our system's ease of use and flexibility for its implementation on

either research and clinical applications.

Taking only into account optical and magnetic solutions, we can extract two main differences between them, the working range and the challenge to operate without a LOS for optical systems.

In order to reduce the LOS dependency, optical systems recur to the use of multiple cameras. This allows maintaining the LOS of the tracked markers with at least two cameras, which is the minimum needed to estimate the markers' relative position. However, this also increases the overall required system price.

Moreover, for high-end accurate systems, the cameras have to be placed in fixed positions to keep the tracking space reference after calibration. This would render the system usable only inside room installation. Moreover, the reallocation of all the necessary system equipment, including cameras, mounting tools, wiring and processing equipment, is not viable for most high-end optical tracking systems.

Even when magnetic systems require a tracking space free of ferromagnetic materials and strong magnetic field sources, which is not a difficult condition to achieve, these systems require less hardware equipment in comparison to high-end optical systems.

This characteristic is of high importance for applications where the researcher or the medical team needs to transport their assessment tool to the research subjects or patients' locations. Moreover, the capability of a magnetic system to work without a LOS allows robust tracking in applications where the user can inadvertently obstruct it.

This comparison leads us to conclude that magnetic systems are a more portable, flexible and lower-cost solution. Therefore, parting from the gen-

eral system characteristics and based on the system values shown in Tab. 2.1, we set as thesis goal, the development of a 6DOF magnetic tracking system defining as initial design constraints:

- Spatial accuracy $\leq 5\,\text{mm}$.
- Tracking volume $= 1\,\text{m}^3$.
- Update rate $= 50\,\text{Hz}$.
- Wireless feature.

Moreover, the system shall feature low weight and wearable tracked markers and have a low implementation cost in comparison to commercially available solutions.

2.2 Magnetic Tracking Systems Literature Review and Thesis Proposals

In this section, we will discuss in more depth the magnetic tracking system's state-of-the-art characteristics, for both commercially available and research-based systems, to evaluate possible research contributions and study which points we can work on to achieve a low-cost accurate tracking system that can be implemented in wearable hardware with wireless communication.

Moreover, a state-of-the-art study is necessary to solve the first research challenge presented that is choosing a hardware architecture and magnetic tracking methodology to comply with design constraints.

2.2.1 Introduction to Magnetic Tracking Systems State-of-the-art

As previously discussed, magnetic tracking systems work by measuring the magnetic field generated by a known controllable source and exploiting the strong relationship that exists between the measured magnitude with the tracked sensor position and orientation relative to the source.

Along with the studied bibliography, we encountered works that use either magnetic field strength (H-field), magnetic flux density (B-field) or voltage generated by mutual inductance as referenced magnitude. We have found also that this fact depends solely on the type of sensor used for the implemented tracking system. For simplicity, we will try to normalize the discussion of tracking models around the B-field. However, we may have to use different physical magnitudes to cite other works from the literature.

In order to perform the position and orientation estimation of the tracked sensor, we need a model of the generated magnetic field and a regression method.

Evidently, methods and algorithms used by commercial magnetic tracking systems as Polhemus, NDI 3D Guidance and NDI Aurora systems, are not disclosed, therefore we can only analyze them from a system-level hardware architecture perspective. The majority of Polhemus available systems and the totality of NDI available magnetic tracking systems present a hardware architecture where a central processing unit is wired to and controls both the driving circuitry of the magnetic field source and the sensor amplifying and filtering circuitry, very similar to the block diagram shown in Fig 2.3. Few exceptions to this architecture can be found in Polhemus systems G4 and Patriot Wireless where the amplifying circuitry is an independent wire-

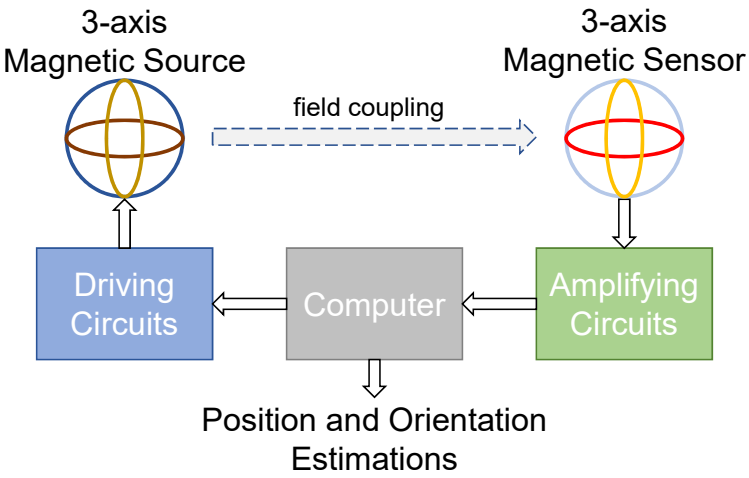

Figure 2.3: System block diagram proposed by Raab et al. (1979)

less system that sends wirelessly pre-processed sensor data to the central unit.

Moreover, the basic roots of Polhemus tracking systems algorithm were published by Raab et al. (1979). It presents the system block diagram shown in Fig. 2.3, where a central computer controls the driving circuit of a magnetic field source formed by three identical and orthogonal coils. The field coupling with a three-axis coil sensor generates a signal that is amplified and processed by the same central computer.

The Raab et al. tracking algorithm parts from the assumption that the magnetic field generated by each coil can be modeled by the magnetic dipole model, previously presented in Eq. (2.1), in spherical coordinates as follows:

$$H_r = \frac{M_T}{2\pi r^3}(\cos\xi) \tag{2.2}$$

$$H_\xi = \frac{M_T}{4\pi r^3}(\sin\xi) \tag{2.3}$$

Where $r = \sqrt{X^2 + Y^2 + Z^2}$, ξ is the angle between the dipole north pole and the measuring position point, and $\cos\xi = \frac{Z}{r}$ when the north pole is aligned with the positive Z axis.

It is stated that this model is valid for a coil of any shape if the sensor to source distance r is higher than four times the radius of the coil, that only near-field and quasi-static field component is significant if the excitation signal wavelength is much higher than r, and that the effective source axes alignment can be changed by varying the initially equal coil excitation amplitudes.

The regression method proposal parts from a source and sensor alignment where the X axes are perfectly aligned, the Y and Z axis are parallel, and the sensed signal can be written as $\vec{f_2} = (C/r^3)\,\boldsymbol{S}\,\vec{f_1}$, being $\vec{f_1}$ the source signals amplitude in vector form, $\vec{f_2}$ the sensor perceived signals in vector form, C the calibration constant that contains both M_T and sensor gain and

$$\boldsymbol{S} = \begin{bmatrix} 1 & 0 & 0 \\ 0 & -1/2 & 0 \\ 0 & 0 & -1/2 \end{bmatrix}.$$

From that starting point, ρ can be easily calculated. Then, representing the position displacement and orientation changes as the rotational matrices $\boldsymbol{T_P}$ and $\boldsymbol{T_R}$, the sensor output in any configuration different from the starting alignment is represented as $\vec{f} = (C/r^3)\,\boldsymbol{T_R}\,\boldsymbol{T_P}\,S\,\vec{f_1}$

It is proposed a closed-loop algorithm that determines small changes in $\boldsymbol{T_P}$ and $\boldsymbol{T_R}$ from the previous measurements, and applies $\boldsymbol{T_P}$ to the source excitation as to maintain alignment between the effective source X axis with the sensor spherical position vector $\vec{P} = [\,r,\,\alpha,\,\beta]$

From our point of view, we can see that for this small change determining and source updating methodology to work it is needed a closed-loop hardware architecture, where the sensor to central computer link could only be implemented wirelessly by a high speed and robust protocol, which can be challenging without taking into account the sensor circuitry and the power-consuming challenges.

To our knowledge, this may be the reason why Polhemus has developed only a few wireless systems and these do not report their best accuracy performances. As for NDI, no wireless magnetic tracking systems have been developed.

In research, we can find a great variety of magnetic tracking system architecture and regression method proposals. A very interesting system was proposed by Huang et al. (2016), where the position and orientation of wireless magnetic markers are estimated on top of a platform that determines the tracking area. The magnetic markers are composed of three orthogonal LC coils designed with different resonant frequencies. Said can be embedded inside objects or adapted to rings to capture finger motion. The platform is composed of an excitation coil that surrounds the platform and an array of multiple smaller receiver coils.

The tracking principle of this system is to have a central unit driving the excitation coil to generate an excitation magnetic field that sweeps through multiple frequencies in a short period. This excitation field will generate a response in all the marker coils corresponding to their resonant frequency. Said responses will be picked up by the receiver coils and processed by a GPU to estimate the marker position and orientation.

The tracking algorithm is based on using the signal perceived by at least 6 receiver coils for each marker LC coil, even when only two LC coils

are needed to compute the marker position and orientation. Then, using these signals, the magnetic dipole model as shown in Eq. (2.1) and least-squares with Gauss-Newton optimization method, compute and estimate the marker 6DOF motion.

Although this system presents is capable of capture 6DOF motion of wearable lightweight markers with millimeter level and degree level accuracy, the tracking space is limited by the size of the platform and requires large processing hardware which can limit its usability in environments such as surgical rooms or tabletop applications.

A different proposal for a wearable system focused in capturing finger motion is found in Chen et al. (2016). The principle of this system is using AC driven cylindrical magnetic coils as active markers to be tracked by an arrange of four tri-axial digital magnetometers placed at the positions [0, 0, 0], [1, 1, 0], [1, −1, 0] and [0, 0, 1].

$$\|H\|^2 = H_r^2 + H_\xi^2 = C\, r^{-6} \left(3 \cos \xi + 1\right) \tag{2.4}$$

The tracking approach retakes the magnetic dipole model expressed as Eqs. (2.2)-(2.3) inside the underconstrained Eq. (2.4) and forms an overconstrained equation system by using the $\|H\|$ perceived and the coil relative position expressed by Eqs. (2.5)-(2.6) inside Eq. (2.4) for each sensor of the array.

$$r = \sqrt{(X - X_i)^2 + (Y - Y_i)^2 + (Z - Z_i)^2} \tag{2.5}$$

$$\cos \xi = \frac{Z - Z_i}{r} \tag{2.6}$$

This system provides the capability of 3D tracking multiple coils with millimeter level and below accuracy inside a 12 cm which can prove very useful for short-range applications.

The main drawback can be found in the necessity of driving the coil with enough current to provide a magnetic field perceivable by the sensors inside a usable range, which can represent a hazard to the user.

Moreover, the tracking algorithm is based on the supposition that the axes of the coils are always aligned with the system Z axis, as expressed by Eq. (2.6). Said supposition can introduce higher estimation errors for a freely moving coil with random orientations, as already shown in Chen et al. publication.

A similar approach is taken by Parizi et al. (2019), where an AC-driven coil and its electronics are embedded around a lightweight ring and the generated magnetic field is perceived by an arrangement of three triaxial magnetometers embedded along with the Microcontroller Unit (MCU) around a wristband. The MCU has the main task of extracting the sensors' measurements and sending them as data packages to the processing unit, in this case, a Laptop. This is done by a common wired connection but could be substituted by a wireless communication protocol.

These works propose an overconstrained equations system using the nine measurements from the three sensors to determine the 5DOF pose of the ring. For this purpose, two tracking algorithm methods are proposed.

An iterative method based on solving the magnetic dipole model through a "non-linear optimizer with Levenberg-Marquardt algorithm to iteratively find the most likely pose" (Parizi et al., 2019) estimation that causes the lowest error the sensor measurements with the predicted magnetic field

values, with a maximum of 100 iterations per point. Parizi et al. also proposes the use of a Kalman filter to proactively estimate the next ring pose to further improve the algorithm speed and accuracy.

The second tracking method is based on a one-time calibration performed by extracting the sensors' measurements when placing the ring at predetermined poses which are measured by an external reference system. Then, using the sensors' measurements paired with the measured positions, train a Neural Network (NN) that will estimate in real-time the ring pose directly using as input the sensor measurements.

The use of NN as a calibration tool can also be found in Huang et al. (2016) where the system accuracy is enhanced by almost 5 times.

A magnetic tracking system similar to in hardware architecture to commercially available solutions but with a different regression methodology is proposed by Attivissimo et al. (2018).

In this system, a 5 coil magnetic source is used to generate multiple frequency magnetic fields. Three coils are aligned with the X, Y and Z axis of the system correspondingly, while the other two coils are aligned with a $45\,^{\circ}$ rotation around the Y of the X and Z axis. Each coil is independently driven by a sinusoidal signal with one of five selected frequencies.

The total generated magnetic field will be picked up by a single coil sensor. The inductance generated voltage proportional to the perceived magnetic field will be processed by a central unit in order to separate its frequency components and calculated their magnitudes.

It is then proposed to use a Look-Up Table (LUT) as a regression method. This LUT will be formed by positioning the sensor in a set of predetermined position points by a robotic arm and for each position point, extracts the

frequency components magnitude of the perceived voltage signal. Pairing these 5 magnitudes with the correspondent sensor position and orientation information a LUT is formed, such that it uses the frequency component magnitudes as input and provides the estimated sensor 6DOF information as output.

This approach allows a better performance of the magnetic tracking in comparison to the NDI Aurora tracking system as stated by Andria et al. (2020). Although this is a great contribution for surgical guidance applications where NDI tracking systems are mainly used, it maintains the bulky hardware architecture that limits the magnetic tracking systems' usage in less critical application fields.

2.2.2 Regression Methods and Hardware Architecture Approaches:

As previously shown, we have found in literature the application of four different methodologies to solve the regression problem and estimate the sensor position $\vec{P}$ and orientation q from the magnetic field model $\vec{B} = f(\vec{P}, q)$. These methodologies can be called closed-loop iterative method, open-loop iterative method, NN-based method and LUT-based method.

The closed-loop iterative methods as reported in Raab et al. (1979) are those where the marker position and/or orientation are estimated iteratively while at the same time the magnetic field source is modified depending on the perceived field for the same purpose, parting from a known mathematical model of $\vec{B} = f(\vec{P}, q)$.

The open-loop iterative methods as reported in Huang et al. (2016); Parizi et al. (2019) are those where the magnetic field source operates indepen-

dently of the perceived signals and the marker position and/or orientation are estimated iteratively, parting from a known mathematical model of $\vec{B} = f(\vec{P}, q)$.

Iterative regression methods as Levenberg-Marquardt or Gauss-Newton method have a computational complexity of $O(n^3)$ due to the matrix inversion involved, where n is the number of treated variables, which might be the reason why heavy hardware is needed to maintain the real-time tracking capability.

The NN-based method as reported in Parizi et al. (2019) consists in pairing sets of the sensor perceived $\vec{B}$ with the sensor P and q measured by an external reference, and train a regression NN that will then represent the inverse function $[\vec{P}, q] = f^{-1}(\vec{B})$, to solve the regression problem presented. In this case it is not necessary to know the mathematical model of $\vec{B} = f(\vec{P}, q)$.

An already trained feed-forward NN computational complexity depends on the NN architecture and can be approximated to $O(n\,m)$ where n and m are the numbers of neurons of the largest layers, which is significantly lower than the computational complexity of an iterative method. The main limitation of a regression NN is the generalization of the trained network, and as shown by Parizi et al. (2019), the performance of NN is slightly lower than the iterative method approach in terms of accuracy.

The LUT-based method as reported in Attivissimo et al. (2018); Andria et al. (2020) consists in pairing sets of the sensor perceived $\vec{B}$ with the sensor P and q measured by an external reference, and form a LUT that will then act as the inverse function $[\vec{P}, q] = f^{-1}(\vec{B})$, to solve the regression problem presented. In this case it is not necessary to know the mathematical model of $\vec{B} = f(\vec{P}, q)$.

An optimized LUT algorithm, for example, a binary tree has an average computational complexity of $O(\log(n))$, where n is the number of the list elements. We need to take into account then the trade-off between the accuracy of the LUT and the memory space needed for its implementation, since both grow when increasing the number of list elements.

Then, from a hardware architecture perspective, the majority of systems present a wired centralized architecture as shown in Fig. 2.3, where a central control and processing unit (usually a computer) controls the magnetic field generator driving circuits and process the sensors signals taken from the sensor amplifying and sometimes filtering block.

Few exceptions, such as Polhemus G4 and Patriot wireless, present an alternative architecture where the sensor amplifying and filtering block includes a digital processing unit in order to transmit wirelessly the sensor data to the central block.

2.2.3 Conclusions

Parting from the alternative wireless hardware architecture and the shown literature information, we have chosen to design a wearable and wireless magnetic tracking system based on the use of a lightweight algorithm onboard a small-sized low-cost MCU that can acquire and process the magnetic field signals perceived by movable sensors and transmit the estimated sensor position and orientation to an end-user device via wireless communication. As for the regression method, we will further study NN-based and LUT-based methods in order to design a lightweight real-time tracking algorithm.

However, by choosing magnetic tracking techniques, we need to revise the

proposed system design constraints, more specifically the system tracking volume. As it can be observed in Tab 2.4, the industry gold standard reports a millimeter-level accuracy for a maximum range of 1 m, while the more accurate systems work in a tracking range of 50 cm. Moreover, from research literature we can extract a working range of 20 cm for the work presented by Huang et al. (2016), 12 cm for the works presented by Chen et al. (2016) and Yoon et al. (2016).

An exception can be found in the work presented by Andria et al. (2020), where they managed to increase the working range to 70 cm by using a LUT approach, working with the sensors of the Aurora tracking system. Therefore, we chose to revise system constraints, parting from a 20 cm tracking range for the initial prototypes and aiming to a 50 cm for a further developed device.

It is also of our interest to limit the marker volume to ensure system wearability. From research literature, we can extract diverse examples of marker volume values. Huang et al. (2016) presented a ring-shaped marker of 4 cm^3 and Yoon et al. (2016) presented a ring-shaped marker of 19 cm^3. Chen et al. (2016) presented a point marker of less than 0.79 cm^3 and Liang et al. (2012) presented a point marker of 1.5 cm^3. On the commercially available systems, we can find that Polhemus offers markers with volume ranging from 9.85 cm^3 down to 26 mm^3, while NDI system commonly include a marker of 1.3 cm^3. Therefore, using these values as a base, we chose to set as design constrain the markers volume below 1 cm^3.

Then, our system design constraints are:

- Spatial accuracy ≤ 5 mm.
- Tracking range = 20 cm.

- Update rate = 50 Hz.
- Wireless feature.
- Marker dimensions $\leq 1\,\mathrm{cm}^3$.

It is our interest to maintain as system design objectives a low implementation cost, 6DOF tracking capability, small processing hardware size in order to be wearable or embedded in medical instrumentation and the capability of including wireless communication with the end-user device.

Up to this point in our thesis work, we have chosen the general approach for our system hardware architecture and magnetic tracking methodology. Now our research challenges consist of the following points:

- Designing a tracking algorithm for the chosen hardware architecture that can ensure real-time 6DOF tracking
- Choosing off-the-shelf hardware components to implement our tracking system within the design constraints at a low implementation cost.
- Choosing a proper methodology for our system the development to test its characteristics continuously and having design flexibility through the system evolution.

In the following chapter, we will introduce our research project development methodology in order to address the latter.

Chapter 3

Methodology

In this chapter, we will introduce the research project development methodology during the implementation of the presented 6DOF magnetic tracking system.

Additionally, we present the testing and validation methods used to characterize the system during its development starting with the consistent experimental methodology for data extraction used during most of these tests until the description of the determination of the test results from the experimental data extracted.

Contents

3.1 System Development Methodology

Adaptive Project Framework is an organized process that allows to incrementally enhance the development planning by learning from outcomes of the goals set at previous project cycle steps. The process changes and adapts to what is needed by the customer, driven by the current product status and ultimately converging to the best project outcome possible.

It grows from the idea that most current technology projects cannot be managed using traditional project management methods. It adjusts to the unknown factors that can crop up during a project's development and prepares teams to respond to unexpected results. Learning by doing can be considered its core principle since work needs to be done in step stages, and evaluated after each stage.

In general, the process begins by setting the end product characteristics. These are the main project goals and are set by the customers and stakeholders. After these goals are set, the development process cycle begins. Each cycle step is normally structured in three sections: planning, executing and evaluating.

Fast production and constant revision can be achieved by keeping the cycle steps short. This consideration allows the continuous discovery of new requirements and the search for new solutions through the collaboration between the customer and the development team.

Adopting this methodology approach, acting as both client and developer, we parted from a set of global goals and split the system development into small significant step phases. As observed in Fig. 3.1, each step represents a development cycle.

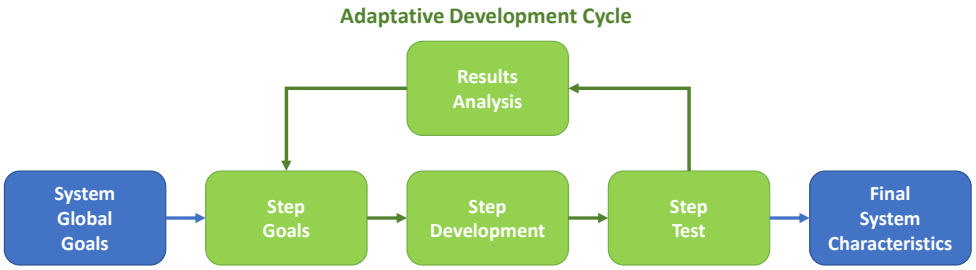

Figure 3.1: Adaptive Project Framework flowchart followed for tracking system development

At the beginning of each step, specific activity goals are set to advance towards a system that fulfills the global goals. The development step may then consist of one or both hardware and software development.

After each development step is done, the testing and/or validation experimentation step is performed. This is done to understand how well the advance has fulfilled the step-specific goals, what characteristics are needed to be modified overall, and which can be the new step-specific goals to get closer to fulfilling the global goals. Although during the project development, the step cycles were much shorter, from algorithm blocks implementation to calibration methodologies testing, in this thesis work we will expose the project development in five significant step cycles.

Parting from the information recollected on the stated of the art study and the proposed global goals, we will first present the hardware architecture and tracking algorithm basic functionalities that we want to adopt to achieve those goals.

Afterward, we present our first step cycle by using simulations of magnetic tracking systems to test the possible regression methods to be used.

Then, the conclusions obtained in the previous test will drive system prototype development, to be tested and conclude how the following step should be carried out to get closer to the system goals. Each development step

will be presented organized with the following structure: specific goals, development, test results and conclusions.

A final section will be presented as ongoing projects, containing further modifications to the final presented system to its adaptation to specific applications.

The testing methodologies will vary in accordance with each specific development step, and their specifics will be explained in the following section.

3.2 Test and Validation methods

In this section we will describe the test and validation procedures used during the development of our magnetic tracking system, starting with the consistent experimental methodology for data extraction used during most of these tests until the description of the determination of the test results from the experimental data extracted.

In order to evaluate our designed system tracking capabilities, we compared the data extracted from the designed system with data extracted from a VICON Motion Tracking system. This system, as previously exposed, is a golden standard for WTS due to its sub-millimeter level tracking capabilities. It can track multiple retro-reflective markers position inside a room-level installation with an update rate of 200 Hz as long as the marker LOS is not obscured. The retro-reflective markers position data extracted from VICON Motion Capture system need to be adapted to be comparable to our system output.

To determine how to formulate this adaptation we need to set our desired 6DOF magnetic system output format. This output will be com-

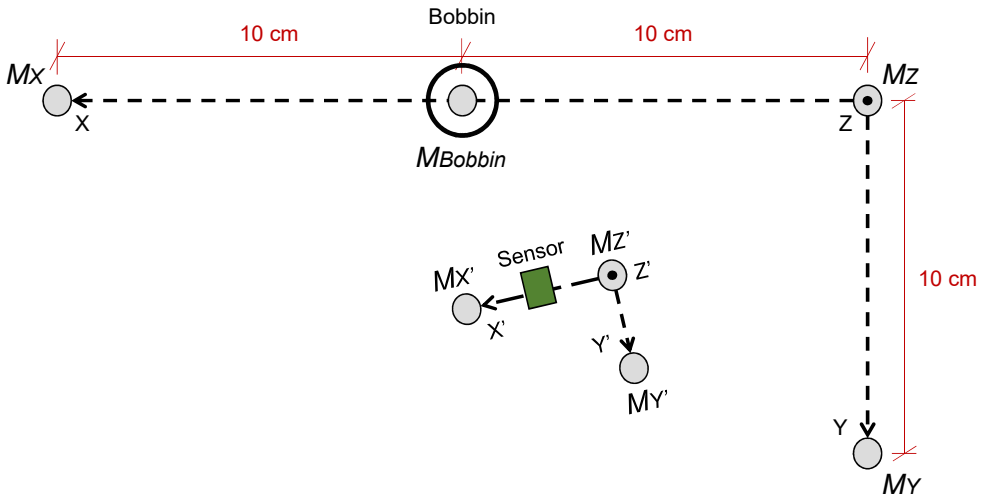

Figure 3.2: Retro-reflective markers placement for magnetic sensor motion tracking and validation.

posed by the magnetic sensor relative position 3D Cartesian vector $\vec{P_S} = [X, Y, Z]$ and the sensor relative orientation q_R in form of quaternion $q = [\cos(\frac{\alpha}{2}), \sin(\frac{\alpha}{2})\, u_X, \sin(\frac{\alpha}{2})\, u_Y, \sin(\frac{\alpha}{2})\, u_Z]$ which represent a rotation of α around the unit vector $[u_X, u_Y, u_Z]$.

In the following chapter, it will be further explained how q_R is calculated, but for now, it is useful to know that q_R is the current measured earth referenced orientation of the sensor q_S de-rotated by the system axes orientation q_0 as the Hamilton product $q_R = q_S\, q_0^{-1}$. We can extract q_0 from an external fixed sensor or by the tracked sensor fixed in an initial position before system usage.

Then, during the development and testing of our prototypes, we designed a 3D-printed sensor holder to attach at least three retro-reflective markers. As observed in Fig. 3.2 we need to extract seven retro-reflective markers position from VICON system. These markers positions are named $\vec{M_X}$, $\vec{M_Y}$, $\vec{M_Z}$, $\vec{M_{X'}}$, $\vec{M_{Y'}}$, $\vec{M_{Z'}}$, $\vec{M_{Bobbin}}$. In order to compare the VICON extracted data to our system data, we proceed as follows.

The system axes are determined as

$$\vec{X} = \frac{(\vec{M_X} - \vec{M_Z})}{\|(\vec{M_X} - \vec{M_Z})\|} \tag{3.1}$$

$$\vec{Y} = \frac{(\vec{M_Y} - \vec{M_Z})}{\|(\vec{M_Y} - \vec{M_Z})\|} \tag{3.2}$$

$$\vec{Z} = \frac{\vec{X} \times \vec{Y}}{\|\vec{X} \times \vec{Y}\|}. \tag{3.3}$$

Then we can determine the system origin $\vec{O}$ as

$$\vec{O'} = \frac{1}{2}(\vec{M_X} - \vec{M_Z}) \tag{3.4}$$

$$\vec{O} = \frac{1}{2}(\vec{M_{Bobbin}} - \vec{O'}) - Z_b\,\vec{Z} \tag{3.5}$$

where Z_b depends on the retro-reflective marker size.

The sensor axes are tracked as

$$\vec{X'} = \frac{(\vec{M_{X'}} - \vec{M_{Z'}})}{\|(\vec{M_{X'}} - \vec{M_{Z'}})\|} \tag{3.6}$$

$$\vec{Y'} = \frac{(\vec{M_{Y'}} - \vec{M_{Z'}})}{\|(\vec{M_{Y'}} - \vec{M_{Z'}})\|} \tag{3.7}$$

$$\vec{Z'} = \frac{\vec{X'} \times \vec{Y'}}{\|\vec{X'} \times \vec{Y'}\|}. \tag{3.8}$$

Since there exist the possibility of small positioning errors of the retro-reflective markers and the rotation matrices need to be orthogonal, we take $\vec{X'}$ as the correct axis and calculate a new axis $\vec{Y''} = \vec{Z'} \times \vec{X'}$. The

sensor rotation matrix is then determined as

$$R_V = [\vec{X'}\ \vec{Y''}\ \vec{Z'}]. \tag{3.9}$$

The sensor position P_V is then determined as

$$\vec{P'_V} = \frac{1}{2}(\vec{X'} - \vec{Z'})\ - Y_b\,\vec{Y''}\ - Z_b\,\vec{Z'} \tag{3.10}$$

$$\vec{P_V} = \vec{P'_V} - \vec{O} \tag{3.11}$$

In order to evaluate the static accuracy of our system inside a determined range, we perform a test consisting of fixing the sensor holder at n position points for 10 s and averaging each sensor position from both our systems and VICON as $\vec{P_{S_i}}$ and $\vec{P_{V_i}}$ correspondingly.

Then, the static accuracy ϵ_S is calculated as the averaged spatial root mean square error for all tested positions as shown in Eq. (3.12).

$$\epsilon_S = \sqrt{\frac{1}{n}\sum_{i=1}^{n} \|\vec{P_{S_i}} - \vec{P_{V_i}}\|^2} \tag{3.12}$$

In order to evaluate our system's dynamic accuracy inside a determined range, we perform m number of tests consisting of moving in four predetermined ways: T-shaped movement, circle movement, arc movement and quasi-random movement.

These shapes are determined to evaluate our system tracking not only quantitatively but also qualitatively by observing the tracked shape and evaluating if it is recognizable.

Then for each test we use our system and VICON sensor position data $\vec{P_{S_i}}(k)$ and $\vec{P_{V_i}}(k)$, being i the evaluated test number and k the time sample.

Each test dynamic accuracy is calculated as the averaged spatial root mean square error for all sampled points as shown in Eq. (3.13).

$$\epsilon_{D_i} = \sqrt{\frac{1}{n}\sum_{k=1}^{n} \|\vec{P_{S_i}}(k) - \vec{P_{V_i}}(k)\|^2} \tag{3.13}$$

Observe that our system sensor position data needs to be oversampled to match the VICON system sampling rate and that since the systems are not synchronized, the test data need to be manually matched in time.

Finally, the total system dynamical accuracy ϵ_D is calculated as the average of all the tests' accuracy.

$$\epsilon_D = \frac{1}{m}\sum_{i=1}^{m} \epsilon_{D_i} \tag{3.14}$$

In order to test the orientation accuracy of our system, we perform m number of tests consisting of rotating the sensor holder around its three axes separately starting from a zero degree position, rotating around $90°$, then rotating to $-90°$ and finally returning to the zero degrees position for each one of the axes.

After extracting both systems' data, we need to normalize the systems rotation output format. Since in literature the rotation accuracy is usually expressed in degrees, both system output formats need to be transformed in Euler angles. For this we adopted the industry standard of Tait–Bryan angles ordered as yaw φ_V, pitch θ_V and roll ψ_V.

First we transform the rotation matrix R_V calculated from VICON data

to angles as,

$$\varphi_V = \text{atan2}(R_{V32}, R_{V33}) \tag{3.15}$$

$$\theta_V = \text{atan2}(-R_{V31}, \sqrt{{R_{V11}}^2 + {R_{V21}}^2}) \tag{3.16}$$

$$\psi_V = \text{atan2}(R_{V21}, R_{V11}) \tag{3.17}$$

or if the matrix is singular $\sqrt{{R_{V11}}^2 + {R_{V21}}^2} < 10^{-6}$, the angles are calculated as follows,

$$\varphi_V = \text{atan2}(-R_{V23}, R_{V22}) \tag{3.18}$$

$$\theta_V = \text{atan2}(-R_{V31}, \sqrt{{R_{V11}}^2 + {R_{V21}}^2}) \tag{3.19}$$

$$\psi_V = 0. \tag{3.20}$$

Then the quaternion output $q_R = [q_{R0},\ q_{R1},\ q_{R2},\ q_{R3}]$ of our system is transformed into the same angles yaw φ_S, pitch θ_S and roll ψ_S as follows,

$$\varphi_S = \text{atan2}[2(q_{R0}q_{R3} + q_{R1}q_{R2}),\ 1 - 2({q_{R2}}^2 + {q_{R3}}^2)] \tag{3.21}$$

$$\theta_S = \arcsin[2(q_{R0}q_{R2} - q_{R3}q_{R1})] \tag{3.22}$$

$$\psi_S = \text{atan2}[2(q_{R0}q_{R1} + q_{R2}q_{R3}),\ 1 - 2({q_{R1}}^2 + {q_{R2}}^2)]. \tag{3.23}$$

Each test orientation accuracy is calculated as the averaged spatial root mean square error for all sampled points as shown in Eq. (3.24) being i

the evaluated test number and k the time sample.

$$\epsilon_{R_i} = \sqrt{\frac{1}{n}\sum_{k=1}^{n}[(\varphi_{S_i}(k) - \varphi_{V_i}(k))^2 + (\theta_{S_i}(k) - \theta_{V_i}(k))^2 + (\psi_{S_i}(k) - \psi_{V_i}(k))^2]} \tag{3.24}$$

Again, observe that our system sensor position data needs to be oversampled to match the VICON system sampling rate and that since the systems are not synchronized, the test data need to be manually matched in time.

Finally, the total system orientation accuracy ϵ_R is calculated as the average of all the tests accuracy,

$$\epsilon_R = \frac{1}{m}\sum_{i=1}^{m}\epsilon_{R_i}. \tag{3.25}$$

Chapter 4

Tracking System Design and Development

In this chapter, we provide information regarding our magnetic tracking system development. As exposed in Chapter 3, our development methodology derives from Adaptive Project Management, dividing it into small but significant development steps to test, analyze and adapt the process.

Therefore, we present our system development in seven sections, each one representing a different step cycle along the process. Each cycle step retakes the conclusions presented in the previous step analysis to set new development proposals.

We part from the system design constraints set in Chapter 2 as general goals and we start presenting our system tracking method proposal. Then, we compare through simulations the best magnetic measurement to position regression methodology to be used in our system. Later, we present our first proof-of-concept prototype to test the feasibility of our proposition for real-time tracking.

With the following steps, we present the system prototype evolution to a low-cost small footprint 6DOF magnetic tracking system with wireless communication.

Finally, we present application-driven design adaptations of our system along with a preliminary capability study, to set future developments and usability of this work.

Partial content of this chapter is reprinted from (Fernandez G et al., 2018) and (Fernandez G et al., 2020) ©IEEE.

Contents

4.1 Magnetic Tracking System Proposition

Partial content of this section is reprinted from (Fernandez G et al., 2020) ©IEEE.

After the previously presented literature study, in this section we will present our system tracking method proposal. For this purpose we begin our system development from the presented general goals. These goals involve the system design based on the following constraints:

- Spatial accuracy $\leq 5\,\text{mm}$.
- Tracking range $= 20\,\text{cm}$.
- Update rate $= 50\,\text{Hz}$.
- Wireless feature.
- Marker dimensions $\leq 1\,\text{cm}^3$.

Moreover, the design goals should also focus on a low implementation cost, 6DOF tracking capability and small processing hardware size to be flexible enough to be implemented in a diversity of biomedical applications.

For this purpose, we chose to work with magnetic tracking techniques. As discussed in previous chapters, magnetic tracking systems are based on exploiting the dependency of a magnetic flux density $\vec{B}$ measurement taken by a magnetic sensor on its position $\vec{P}$ and orientation q_R relative to the magnetic field generator.

This dependency can usually be represented by a mathematical model of the magnetic field. Said model accuracy heavily depends on the tracking

environment composition, the field generator geometry and materials, and could be proposed by solving Maxwell's equations.

A commonly adopted solution in magnetic tracking systems is modeling the magnetic field source current loop or bobbin as a magnetic dipole in vacuum, as expressed by Eq. (2.1). It presents a simplification of the problem and even if it does not accurately describe the generated magnetic field near the source, it has been adopted as valid for implementations assuming the sensor to source distance greater than four times the source current loop radius as expressed by Raab et al. (1979).

In order to calculate $\vec{B} = f_B(\vec{P}, q_R)$ for more complex source structures, such as a bobbin coil with ferromagnetic core, Finite Element Methods (FEM) modeling can be used to solve numerically the correspondent Maxwell's equations.

However, as expressed in previous chapters, the objective is to estimate the sensor position $\vec{P}$ using $\vec{B}$ measurements, therefore a way to perform the inverse function $\vec{P} = f_P(\vec{B})$. It can be seen from the simplest magnetic flux model represented in Eq. (2.1), that performing this regression is not a simple task.

As exposed previously, commonly used tools to solve this problem are regression methods, such as non-linear squares solved by Gauss-Newton or Levenberg-Marquardt algorithms. However, this requires high computational power for real-time application with a competitive update rate and leads to the necessity of using a high complexity processing hardware limiting the capability of a magnetic tracking system to be designed as a wearable and wireless device.

Alternatives solutions propose the use of LUT and NN as less computa-

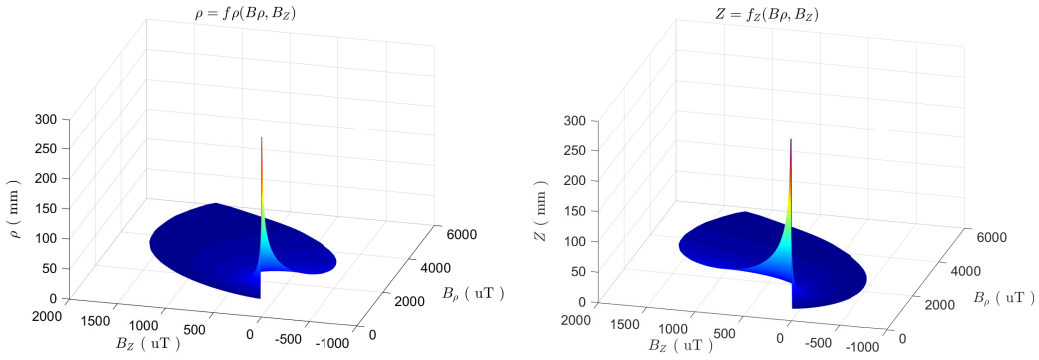

Figure 4.1: Sensor coordinates ρ (a) and Z (b) as a function of magnetic flux measurements B_ρ and B_Z. ©[2020] IEEE.

tional expensive methods.

4.1.1 Magnetic Tracking Technique

As a possible solution for the problem regarding the magnetic measurement to sensor position regression, we propose the following methodology. First we divide our tracking space of interest forming a regular grid of 2D position points in cylindrical coordinates $\{\vec{P_i}\} = \{[\rho_i, Z_i]\}$. Then, from a FEM model created with Finite Element Method Magnetics tool which allow us to simulate the magnetic field generated by a bobbin coil in 2D cylindrical coordinates, we extract the correspondent set of magnetic flux density $\{\vec{B_i}\} = \{[B_{\rho i}, B_{Zi}]\} = f_B(\{\vec{P_i}\})$ for each point of the grid.

Then for the position points $\{\vec{P_i}\} \in \{Z_i\} \geq 0$, we can use the paired data sets to form the regression functions as shown in Eq. (4.1). Fig. 4.1 displays the regression functions f_ρ and f_Z surface formed from the a position grid defined with $\Delta\rho = 1\,\text{mm}$ and $\Delta Z = 1\,\text{mm}$ showing a unique position point $\vec{P_i}$ for each $\vec{B_i}$,

$$\hat{\vec{P}} = [\hat{\rho}, \hat{Z}] = [f_\rho(B_\rho, B_Z), f_Z(B_\rho, B_Z)]. \tag{4.1}$$

In order to generalize the use of f_ρ and f_Z for an arbitrary measurement $\vec{B} \notin \{\vec{B_i}\}$ we could use a regression NN trained with $\{\vec{B_i}\}$ as input and $\{\vec{P_i}\}$ as target. Alternatively, we could an Scattered Interpolation (Amidror, 2002).

The Scattered Interpolation method consists in forming a Delaunay Triangulation with the set $\{\vec{B_i}\}$. Then, as in a LUT, the algorithm determines to which triangle T_k the new input $\vec{B_k} = [B_{\rho k}, B_{Zk}]$ belongs. And finally, a surface interpolation is carried out using the three points of $\{\vec{B_i}\}$ forming T_k, their correspondent points in $\{\vec{P_i}\}$ and the input $\vec{B_k}$, obtaining as output the estimation $[\hat{\rho}_k, \hat{Z}_k]$.

As shown in Fig. 4.2 we can use either of these 2D solutions for Eq. (4.1) at the 3D problem according to the following steps:

1. Measure the sensor magnetic flux density as $\vec{B} = [B_{X'}, B_{Y'}, B_{Z'}]$;
2. Calculate $B_\rho = \sqrt{B_{X'}^2 + B_{Y'}^2}$;
3. Estimate $\hat{\rho}$ and $\hat{Z}$ from the regressions functions Eq. (4.1), while $\hat{\theta}$ is the B_ρ projection angle in the $X'Y'$ plane.

However, this approach is applicable only if the sensor axes $[X', Y', Z']$ and the system axes $[X, Y, Z]$ are aligned. Therefore, the sensor measurements $\vec{B} = [B_{X'}, B_{Y'}, B_{Z'}]$ correspond to their system referenced components $\vec{B_R} = [B_X, B_Y, B_Z]$.

Notice that when the sensor and system axes are not aligned, the solution can still be applicable by knowing relative sensor orientation with respect to the system axes given by the Hamilton product shown in Eq. (4.2), where q_0 and q_S are the earth referenced system and sensor orientation

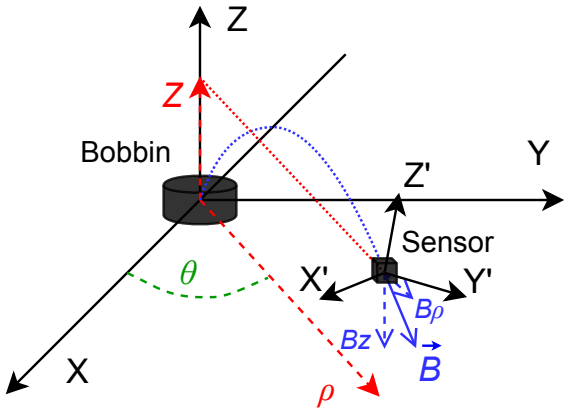

Figure 4.2: Sensed magnetic flux density vector components B_ρ and B_Z, and cylindrical sensor coordinates ρ, Z and θ with respect to the system axes. ©[2020] IEEE.

respectively.

$$q_R = q_S \, q_0^{-1} \tag{4.2}$$

In this case we can consider the transformation of the sensor measured magnetic flux density $\vec{B}$ to the system referenced magnetic flux density $\vec{B_R}$ by the quaternion rotation using the Hamilton product as shown in Eq. (4.3).

$$\vec{B_R} = q_R \, \vec{B} \, q_R^{-1} \tag{4.3}$$

Therefore, an independent method to estimate the sensor and system orientation q_S and q_0 respectively. As previously discussed, AHRS involving IMU-based algorithms to determine their Earth relative orientation has been continuously used and developed during the last two decades due to the high accuracy and the small-sized wearable hardware solutions these can provide.

For this purpose we considered the AHRS algorithm developed by Madgwick et al. (2011). It is an open source complementary filter algorithm characterized by its low computational cost compared to KF based AHRS

algorithms as shown by Madgwick et al. (2011); Li and Wang (2019).

Moreover, Li and Wang (2019); Li et al. (2018) show that the algorithm can be easily integrated in dead reckoning positioning systems and to enhance their performances. Furthermore, Cavallo et al. (2014) experimentally compares Madgwick's algorithm with an EKF based AHRS running on a M4-Cortex MCU, getting comparable accuracy results for a computational cost one order of magnitude lower. Reprinted from (Fernandez G et al., 2020)

Therefore, we have chosen Madgwick's algorithm to estimate both sensor and system Earth referenced orientations q_S and q_0 respectively.

Finally, to avoid mixing with the Earth and power lines generated magnetic fields and still considering the presented scenario as a quasistatic problem, a low-frequency field between 70 Hz and 20 kHz will be generated by the single-axis bobbin coil.

$$\vec{B_R}(t) = \vec{B_R} \sin 2\pi f_0 \, t + \phi \tag{4.4}$$

The sensed magnetic flux density signal is therefore variable in time with the form shown by Eq. (4.4), where $\vec{B_R}$ is still composed as expressed by Eq. (4.3).

Other considerations need to be taken into account since we need to use the B_ρ projection angle θ in the $X'Y$'plane as part of the position estimation procedure.

On one side having a full synchronization with the magnetic field generator would allow us to know exactly the sensed $\vec{B_R}(t)$ phase ϕ. Otherwise, using a tracking space limited by either $X \geq 0$ or $Y \geq 0$ would allow us to be

able to assume respectively $B_{X'}$ or $B_{Y'}$, as an always positive component and use this to calculate ϕ.

At this point, by knowing ϕ we can extract the sensed $\vec{B_R}(t)$ amplitude $\vec{B_R}$ with its correspondent direction and use the previously explained method to estimate the sensor position $\hat{\vec{P}}$.

Since one of our main goals is to develop a wearable and wireless system, having the processing unit and the magnetic field source generator synchronized can be quite challenging. Therefore, we opted by limiting the tracking space to the region delimited by $Y \geq 0$.

4.1.2 System Hardware Architecture

The previously exposed considerations taken into account for developing our tracking methodology, allow us to propose a wireless and asynchronous system hardware architecture as shown in Fig. 4.3, where we can observe the system divided into two modules, the field generator module and the sensing module, interfaced to an end-user device running the GUI.

The field generator module is in charge of generating the low-frequency oscillating magnetic field. It comprises a MCU that generates the sinusoidal signal, a power amplifier to feed the single axial cylindrical bobbin coil. It should also contain a mechanically fixed IMU sampled by the MCU to set the system axes orientation with respect to Earth. BLE module allows the wireless communication with the end-user device running the GUI. Finally, a power supply unit powers both the MCU and the power amplifier.

The sensing module comprises multiple couples of tri-axial magnetic flux density and IMU sensors controlled by a MCU which is also in charge of

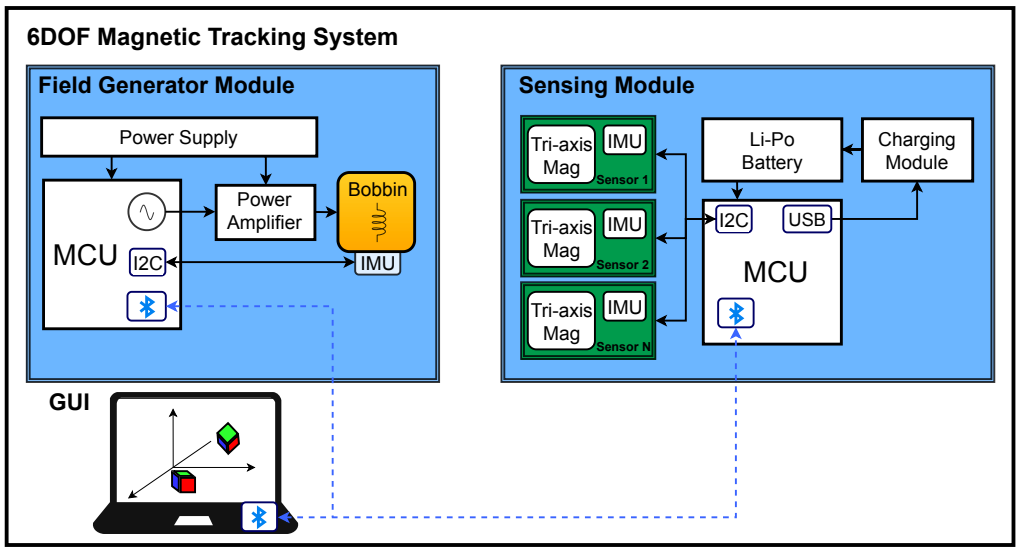

Figure 4.3: System-level conceptual hardware architecture. The system is divided into two modules, the field generator module, which is in charge of generating the AC magnetic field and the sensing module, which processes the sensed signals and estimates the magnetic sensors' relative position. Additionally, a device connected wirelessly to the modules will contain the system's graphical user interface. ©[2020] IEEE.

processing the sensor signals to estimate both its position and orientation with respect to the bobbin coil and the field generator IMU respectively. To allow high levels of wearability a rechargeable Li-Po battery-based powering system and a BLE module can be used for wireless communication to send the tracked sensors processed data to the GUI.

Finally, the GUI will run in the end-user device connected to both modules via BLE allowing the field generator control and receiving the sensor module data. As an alternative solution the GUI could run the regression functions Eq. (4.1) if the application requires a large accuracy and range, demanding a memory space higher than the MCU available Random Access Memory (RAM). To be considered is the BLE data throughput will act as a limiter to the regressions function update rate. However, we consider this alternative of secondary importance since it relies on the end-user device characteristics and not on the tracking system itself, which is the core contribution.

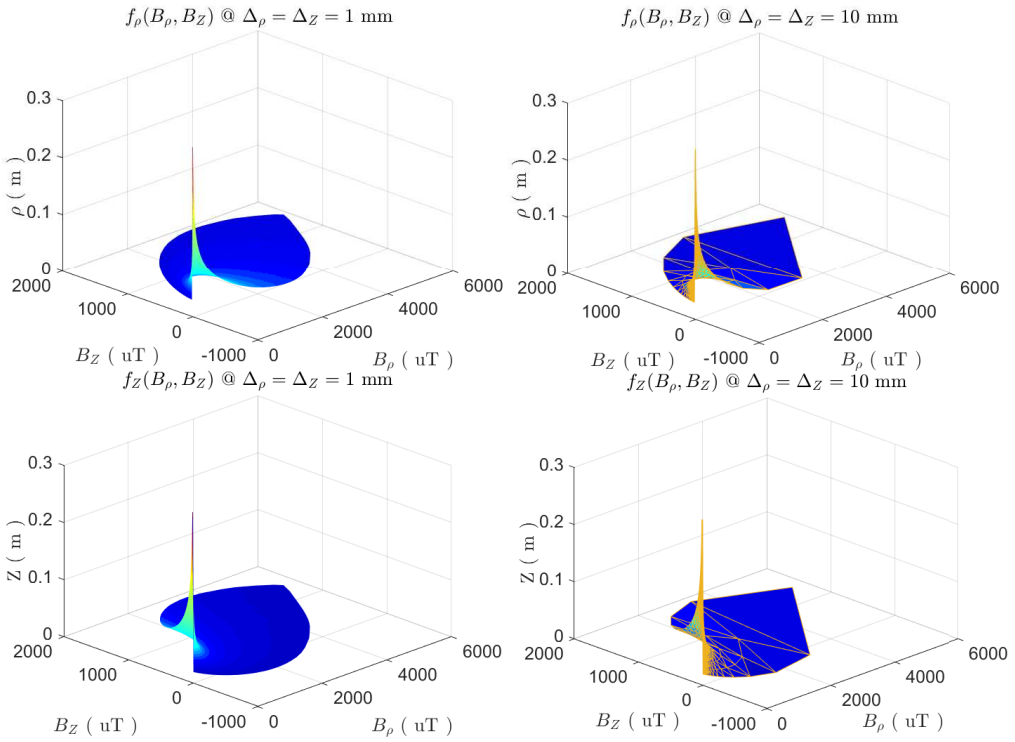

Figure 4.4: Scattered interpolation of regression functions $\rho = f_\rho(B_\rho, B_Z)$ and $Z = f_Z(B_\rho, B_Z)$ comparison for different position grids $\Delta\rho = \Delta_Z = 1\,\text{mm}$ and $\Delta\rho = \Delta_Z = 10\,\text{mm}$. ©[2020] IEEE.

It is important to take into account that if the regressions functions Eq. (4.1) are implemented inside the sensing module MCU, it is necessary to trade-off between the regressions function accuracy and range, and the required RAM space from the MCU.

As previously discussed, we propose the implementation of the proposed regression functions Eq. (4.1) through the use scattered interpolations (Amidror, 2002) or a Generalized Regression Neural Network (GRNN) (MathWorks, 2021).

The accuracy of these regression methods is directly linked to the number of points used to build the scattered interpolation mesh or to train the neural network, and to the memory space required to store the data for its real-time use. Fig. 4.4 shows the smoothness loss of the graphical representation of the regression functions Eq. (4.1) by using a position

grid of $\Delta\rho = \Delta_Z = 10\,\text{mm}$ instead of $\Delta\rho = \Delta_Z = 1\,\text{mm}$. Therefore, the quantitative trade-off between the accuracy and required memory space will be further discussed at the time of implementing the chosen method in the MCU.

First, in the following section, we will analyze through simulations of a sample magnetic field which regression method is more suitable for our needs considering accuracy, memory space and computational complexity.

4.2 3D Magnetic Tracking Simulations: Regression Methodologies Comparison

In this section, we will analyze and determine which regression method to use for the purpose of converting magnetic flux density measurements $\vec{B}$ to sensor position estimation $\hat{\vec{P}}$ between the previously discussed methods Scattered Interpolation and GRNN.

In order to do this, we will use Finite Element Method Magnetics which is a FEM toolbox focused on solving magnetic field, electrostatic field, heat flow and current flow problems with Matlab interface which allows for a fast simulation setting and simulation results processing.

First, we form a position point grid $\{\vec{P}_i\} = \{[\rho_i,\, Z_i]\}$ with a spacing $[\Delta\rho = 1\,\text{cm},\, \Delta Z = 1\,\text{cm}]$ within the range $5\,\text{cm} \leq \rho \leq 29\,\text{cm}$ and $3\,\text{cm} \leq Z \leq 30\,\text{cm}$ obtaining a total of 700 points.

Then, using the FEM toolbox we set a 2D cylindrical simulation of the magnetic field generated by a 300 turns bobbin coil with a relative permeability $\mu_r = 2000$ core, 30 AWG magnetic wire of 2 cm longitude and 6 mm

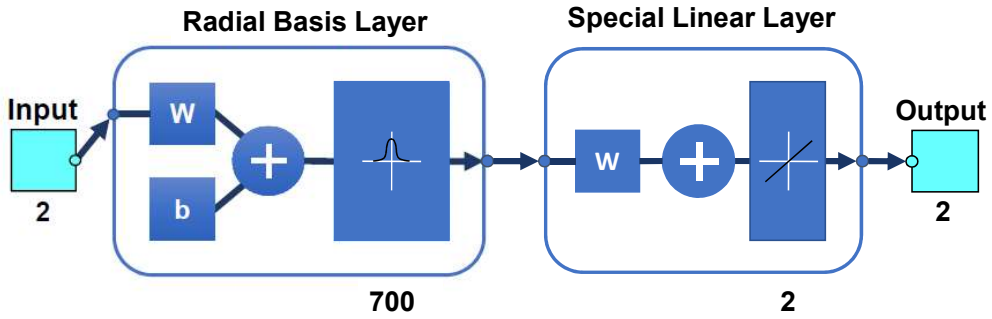

Figure 4.5: Generic Regression Two-Layer Neural Network used as regression method alternative to estimate sensor position from magnetic flux measurements.

radius fed by a 1 A current and surround by air medium with a $\mu_r = 1$.

From this simulation, using the previously defined position point grid $\{\vec{P}_i\}$, we extract the base magnetic flux data set $\{\vec{B}_i\} = \{[B_{\rho i}, B_{Zi}]\}$ that will be used to form our regression methods.

In order to create a GRNN as our first regression method proposal, we use the integrated Matlab toolbox. As shown in Fig. 4.5, the GRNN is a two-layer NN, a radial basis layer with N neurons and a linear layer with Q neurons, where N is the number of training samples and Q is the output size. Then, we use the simulated magnetic flux data set $\{\vec{B}_i\}$ as input data and the correspondent position points data set $\{\vec{P}_i\}$ as targets for NN training.

Using the Scattered Interpolant toolbox integrated into Matlab, we form two interpolated surfaces $\hat{\rho}(B_\rho, B_Z)$ and $\hat{Z}(B_\rho, B_Z)$ as our second regression method proposal. This tool forms a Delauney triangulation using the simulated magnetic flux data set $\{\vec{B}_i\}$, while defines $\hat{\rho}(B_\rho, B_Z)$ and $\hat{Z}(B_\rho, B_Z)$ using the correspondent information from the position points data set $\{\vec{P}_i\}$. An example of these surfaces can be seen in Fig 4.4.

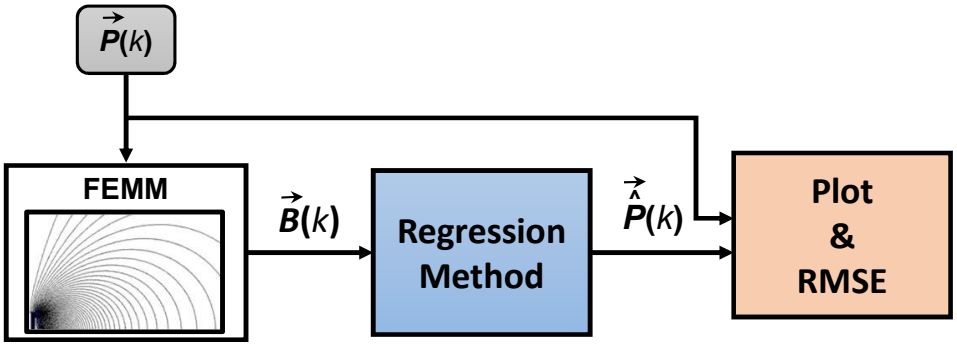

Figure 4.6: Estimation of a moving sensor position simulation blocks

4.2.1 Experimental Tests

In order to have a first idea of the accuracy of each one of these methods, we define a new position point data set $\{\vec{P_{ref}}\} = \{[\rho_{ref},\, Z_{ref}]\}$ with a spacing grid $[\Delta\rho = 1\,\text{mm},\, \Delta Z = 1\,\text{mm}]$ within the same range, and a new simulated magnetic flux data set $\{\vec{B_{ref}}\}$ extracted from the FEM simulation.

Then, we use $\{\vec{B_{ref}}\}$ as input for both regression methods and compare the output with $\{\vec{P_{ref}}\}$ using Eq. (3.12), where $\vec{P_{S_i}}$ correspond to the used regression method output and $\vec{P_{V_i}}$ correspond to $\{\vec{P_{ref}}\}$. The resulting static accuracy for GRNN is of $\epsilon_{S1} = 3.59\,\text{cm}$, while the scattered interpolations obtain a static accuracy $\epsilon_{S2} = 0.821\,\text{mm}$.

To further understand the extent of the regression methods accuracy, we form a simulation of a dynamic accuracy test as shown in Fig. 4.6, where the position vector data $\vec{P}(k)$ of a moving sensor is used as input for the Finite Element Method Magnetics simulation, extracting the correspondent simulated magnetic flux density measurement $\vec{B}(k)$. Then, $\vec{B}(k)$ is used as input for each one of the regression methods to estimate sensor position point as $\hat{\vec{P}}(k)$ and finally compare it graphically and analytically to the initial data $\vec{P}(k)$.

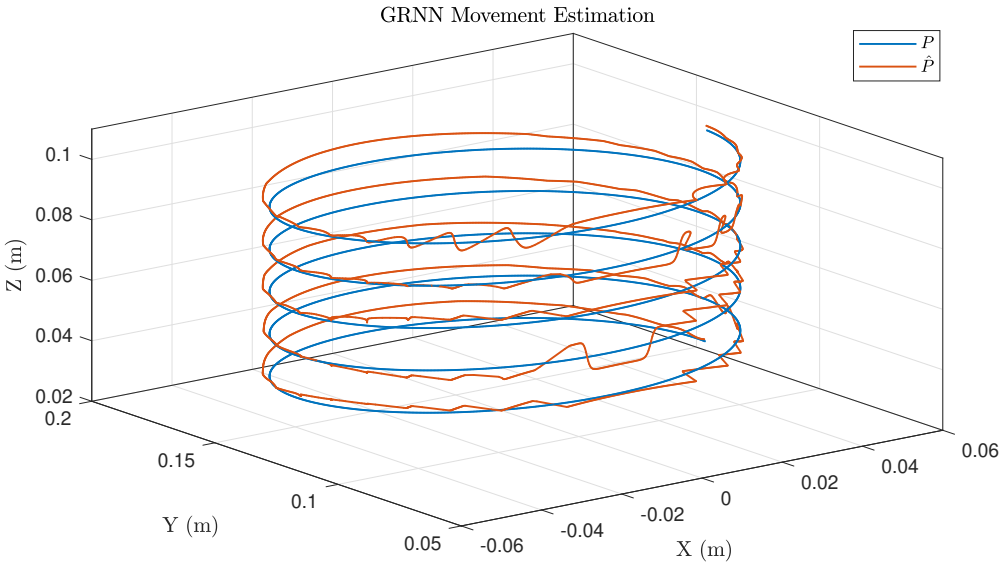

Figure 4.7: GRNN position estimation result.

We chose a movement describing a 5 cm radius circumference in the XY plane around the point $X = 0$ cm, $Y = 13$ cm, while linearly moving from $Z = 3$ cm to $Z = 10$ cm. Fig. 4.7 compares the GRNN estimated position $\vec{P}(k)$ (blue) to $\vec{\hat{P}}(k)$ (red), which results in a dynamic estimation accuracy $\epsilon_{D1} = 3.65$ mm. Fig. 4.8 compares the scattered interpolation estimated position $\vec{P}(k)$ (blue) to $\vec{\hat{P}}(k)$ (red), which results in a dynamic estimation accuracy $\epsilon_{D2} = 0.345$ mm.

For the purpose of comparing the computational cost of each method we measured the processing time that each method takes to estimate a position point from a magnetic flux measurement, obtaining results for the GRNN between 14 ms and 18 ms, while for the scattered interpolation estimations took between 0.3 ms and 1.1 ms. Finally, the GRNN occupies a memory space of 94 kB, while the interpolations occupy a total memory space of 34 kB.

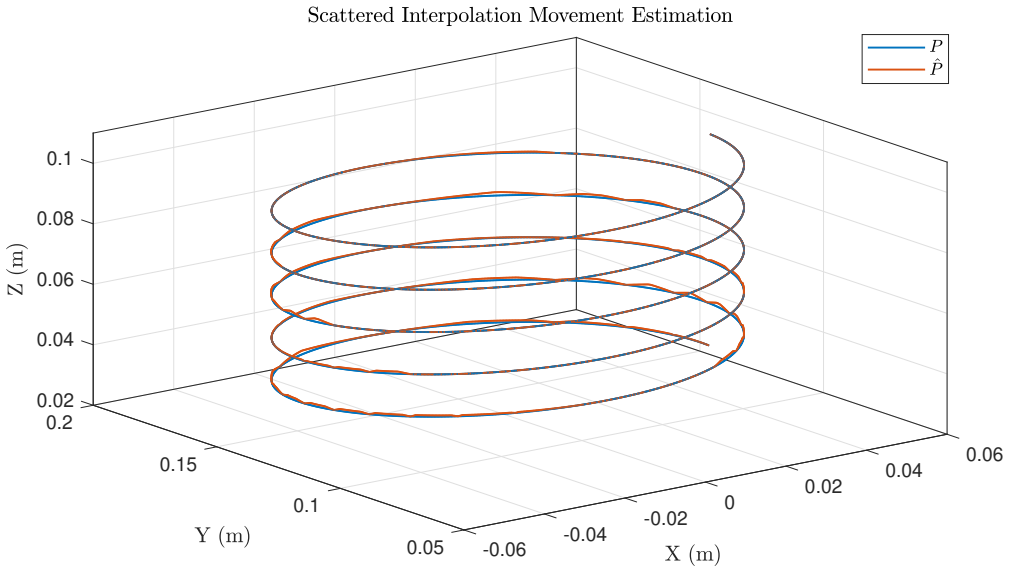

Figure 4.8: Scattered interpolator position estimation result.

4.2.2 Results Discussion

From the static accuracy test results, we can observe an already superior performance of the scattered interpolations over the GRNN.

Then, by using the simulation of a moving sensor magnetic flux density measurements as a dynamical accuracy test, we can observe both graphically and numerically superior performance of the Scattered Interpolation method in terms of spatial accuracy.

Finally, other important aspects to have into account are the required memory space and the computational cost of each method, aspects in which the Scattered Interpolation method presented better characteristics.

From these simulation results, we can determine that the optimal regression method for our system is the scattered interpolation of the regression functions Eq. (4.1). The next step for our system development is to implement a first proof-of-concept prototype with a simplified version of the hardware architecture and tracking methodology described in the previous

sections, to demonstrate the viability of our tracking proposal sensing a magnetic field in real-time.

4.3 First Proof-of-Concept Prototype: 2D Real-time Tracking

In the previous section, we determined that the optimal regression method for our system is the scattered interpolation of the regression functions Eq. (4.1) formed from a grid of position points and magnetic flux density values extracted from a FEM simulation.

In this section, we will describe the development of the first proof of concept prototype of our proposed system. For this purpose we will implement a simplified version of the hardware system architecture described in Fig. 4.3, focused on evaluating the proposed tracking method feasibility in real-time and testing the system preliminary accuracy performance. Partial content of this section is reprinted from (Fernandez G et al., 2018) ©IEEE.

The field generator module was assembled using the following elements:

- Aim-TTi EX354Tv as DC Power Suppky;
- Teledyne Lecroy Wavestation 3082 as signal generator;
- ST STEVAL-CCA044V1 as signal power amplifier board;
- 360 turns handcrafted uni-axial bobbin coil with $\mu_r = 2000$ MnZn ferrite core and 30 AWG magnetic wire.

The magnetic field is generated by feeding the bobbin coil with a sinusoidal current signal of 150 Hz frequency and 1 A amplitude.

The sensing module was assembled using the following elements:

- Kionix KMX62-1031 tri-axial magnetic/accelerometer sensor evaluating board;
- Micropython Pyboard V1.1;
- Laptop running Matlab.

The Pyboard connected through Inter-Integrated Circuit (I2C) samples the KMX62 magnetic and accelerometer sensor data at 1 kHz and sent it via USB connection to the laptop running the tracking algorithm on Matlab.

As a consequence of the hardware simplification, we implemented a simplified 2DOF tracking algorithm capable of estimating the sensor 2D position

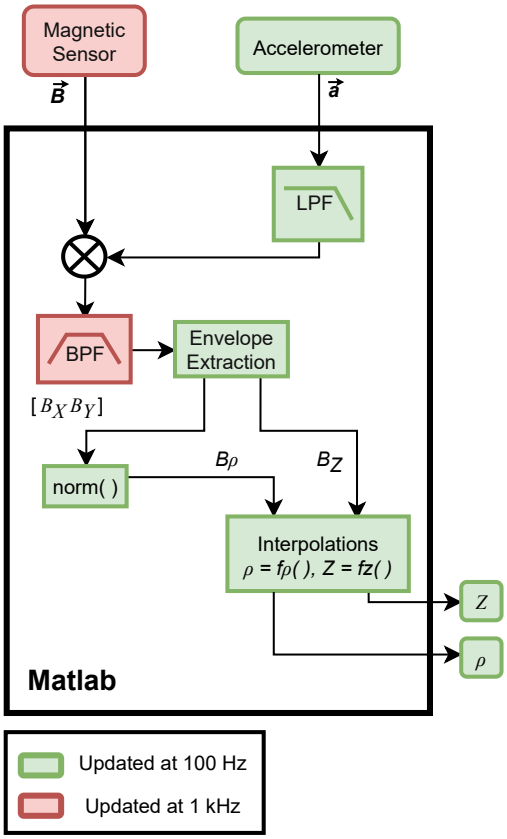

Figure 4.9: Algorithm implementation flowchart to estimate position cylindrical coordinates ρ and Z from a single tri-axial magnetic and accelerometer sensor couple.

$\hat{\vec{P}}$ as $[\rho, Z]$ and while correcting the sensor tilt and roll angles.

Fig. 4.9 describes the implemented algorithm. It uses the sensor magnetic data sampled at 1 kHz and accelerometer data sampled at 100 Hz as input.

The accelerometer data is filtered with a Low-Pass Filter (LPF) with a cut-off frequency of 10 Hz in order to extract only Earth gravitational force $\vec{g}$ from the sensor. The unit vector $\hat{\vec{g}} = \vec{g}/\|\vec{g}\|$ determines the system Z axis and the system plane XY.

This information is used to correct the sensor tilt and roll angles by rotating the measured $\vec{B}$ around the vector $\vec{u}$ Eq. (4.5) by the angle α between $\hat{\vec{g}}$ and the sensor axis $\vec{Z}' = [0\,0\,1]$ as shown in Eq. (4.6),

$$\vec{u} = \frac{\hat{\vec{g}} \times \vec{Z}'}{\|\hat{\vec{g}} \times \vec{Z}'\|} \tag{4.5}$$

$$\vec{B_R} = (\vec{u} \cdot \vec{B})\,\vec{u} + \cos\alpha\,(\vec{u} \times \vec{B}) \times \vec{u} + \sin\alpha\,(\vec{u} \times \vec{B}). \tag{4.6}$$

This operation is performed on the next 10 magnetic sensor samples for every new accelerometer sample to maintain the time correlation. Then, the corrected magnetic sample $\vec{B_R}$ is filtered by a Band-Pass Filter (BPF) with a 50 Hz bandwidth.

The amplitude of each component of $\vec{B_R}$ is extracted using the absolute value Hilbert's transformation, while the sign of the component B_Z is determined from the phase between it and B_Y, where is always $B_Y \geq 0$ as previously discussed.

Then, $B_\rho = \|[B_X\, B_Y]\|$ is determined and finally $\hat{\rho}$ and $\hat{Z}$ are calculated from Eq. (4.1) using the scattered interpolations previously defined.

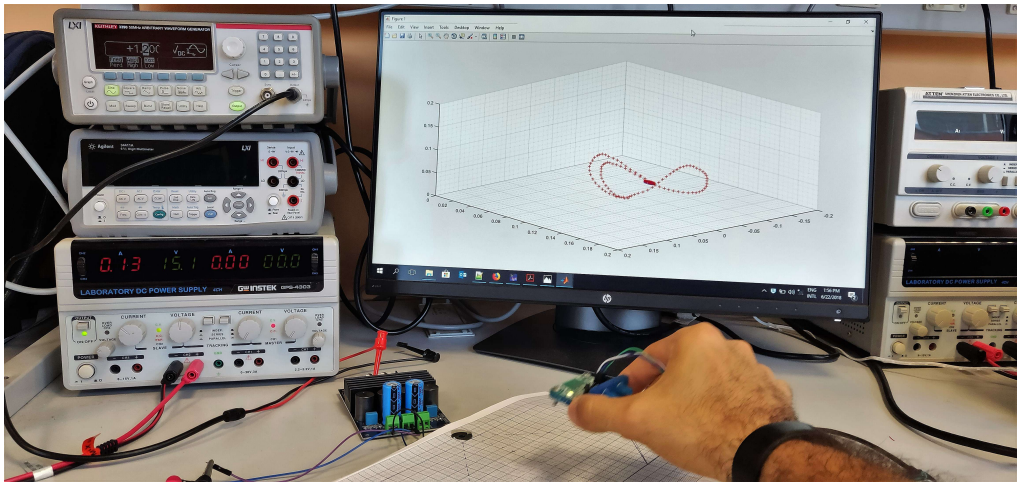

Figure 4.10: Real-time implementation of the system in Matlab. ©[2018] IEEE.

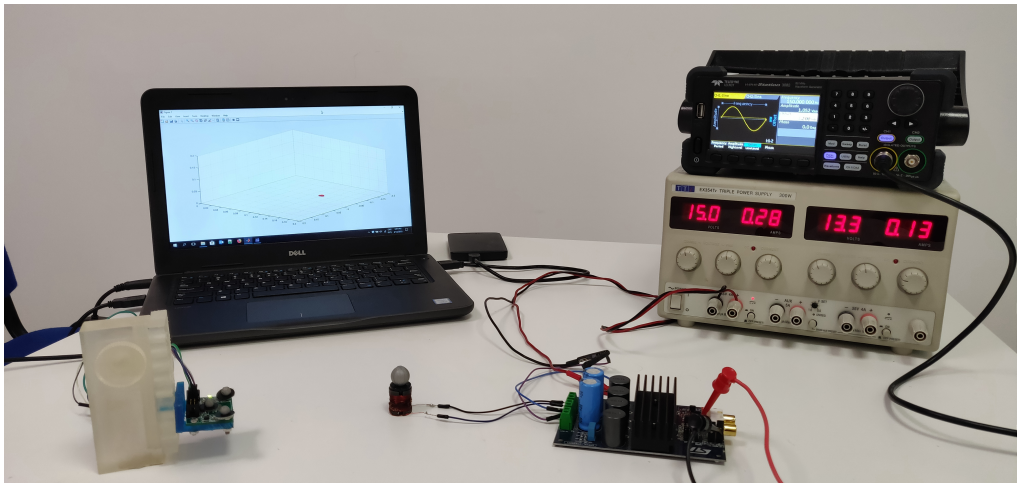

Figure 4.11: The system test setup with VICON retroreflective markers attached to bobbin and system tracked marker. ©[2018] IEEE.

4.3.1 Experimental Tests

As mentioned before, this basic real-time implementation is limited due to the current incapability of estimating the sensor yaw. Therefore, we evaluate only qualitatively the capability of the prototype system to track the sensor movements as shown in Fig 4.10 while maintaining the sensor from rotating around Z axis. From a more quantitative point of view, the system presents a stable dynamic tracking capability with 50 Hz update rate and 100 ms latency.

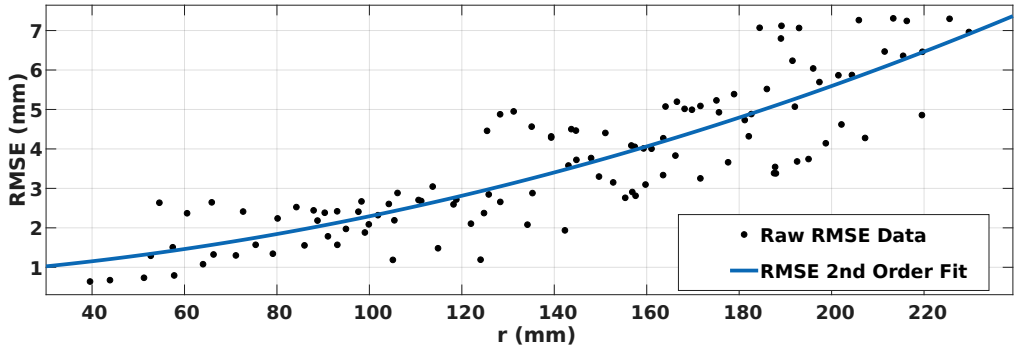

Figure 4.12: Second order fit of spatial RMSE values with respect to the reference sensor to bobbin distance r. ©[2018] IEEE.

A static accuracy test was performed placing the system on top of a table without the presence of additional strong magnetic field sources or ferromagnetic materials that could distort the generated magnetic field, inside a room of 3 m × 4 m × 3 m with 9 VICON cameras placed at 3 m height allowing the tracking of retro-reflective markers with a 1 mm accuracy and 0.1 mm precision, as shown in Fig. 4.11 .

An overall volume of 36 cm × 20 cm × 12 cm was covered using 114 different measurement points. VICON recordings of 5 s were used to calculate the Root Mean Squared Error (RMSE) of 8 s measurements of the proposed system for each used point.

The resulting system average spatial RMSE was 6.5 mm. Fig. 4.12 depicts the spatial RMSE value of each point as a function of the sensor to bobbin distance r, showing a system accuracy performance below 3 mm for a 12 cm range, below 5 mm for a 16 cm range and below 8 mm for a maximum of 23 cm.

4.3.2 Results Discussion

These preliminary results prove the feasibility of implementing the proposed regression methodology in real-time and obtaining millimeter-level

accuracy results without any preliminary calibration procedure.

Following steps shall consist in implementing the discussed algorithm embedded on a MCU as the initial implementation of an independent wearable low-cost tracking system. Furthermore, the presented algorithm capabilities shall be extended to estimate the sensor attitude and provide a 6DOF estimation output. For this purpose, a PCB marker combining the used magnetic sensor with an extra IMU sensor shall be designed to provide the necessary information for the tracking algorithm.

Another consideration taken from this experimentation is the necessity of redesigning the magnetic source bobbin coil due to the core material overheating after long testing periods while maintaining a similar magnitude of the generated magnetic flux density at a given distance, for example, 20 cm.

Additionally, the sensors' sampling frequencies and magnetic field frequency should be modified to match multiples of the internal sampling frequencies of the KMX62 sensor to reduce the sampled signal artefacts.

Moreover, since the computation of the Hilbert transform is non-trivial, an alternative and accurate way to determine the sampled signal envelope is needed to maintain and even enhance the system accuracy on board of a MCU.

Furthermore, the Scattered Interpolant toolbox is a non-disclosed Matlab integrated implementation. Therefore, we will need to develop our implementation of this method to be run inside the MCU.

4.4 6DOF Proof-of-Concept Prototype

In this section, we will describe the development of our first 6DOF magnetic tracking prototype embedded onboard a MCU parting from the 2D tracking prototype and the tracking methodologies described in the previous section and we will focus on evaluating the prototype static and dynamic accuracy performance. Partial content of this section is reprinted from (Fernandez G et al., 2020) ©IEEE.

An important point to be considered for a real-time and self-contained tracking system is the difference of computational power and available RAM between a personal computer running Matlab and a MCU. This takes importance at the time of implementing filters, the regression scattered interpolations, the Madgwick's algorithm and, as previously concluded, the envelope extraction algorithm.

The first modification to the system hardware is implemented in the field generator module due to the overheating problems of the ferrite core. For this purpose we use we analyze different bobbin models with Finite Element Methods Magnetic focusing on finding a close magnetic flux density value at the position point $\rho = 20\,\text{cm}$, $Z = 0\,\text{cm}$ keeping the current signal amplitude at 1 A and using a high temperature resistive 3D-printing resin as the material of the coil base. We find an optimal design by using a 3 cm long with 800 turns, 30 AWG magnetic wire of 1 cm internal radius and 2.3 cm external radius.

We maintain the Aim-TTi EX354TV, the Teledyne Lecroy Wavestation 3082 and the ST STEVAL-CCA044V1 board as the field generator module power supply, signal generator and signal power amplifier respectively.

Further modifications are implemented in the sensing module to extend the

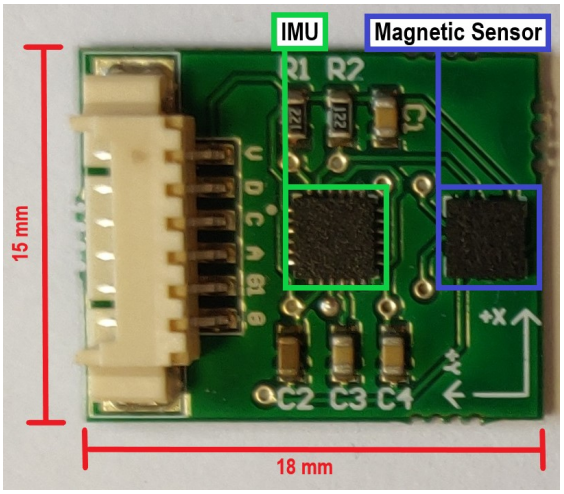

Figure 4.13: Wearable sensor prototype. A MPU9250 IMU is used to estimate the sensor couple orientation, while a KMX62-1031 is used as magnetic sensor and a Molex PicoBlade 6 pin connector is used for I2C communication and power supply. ©[2020] IEEE.

system tracking capabilities and develop it as a self-contained unit.

In the first place as shown in Fig. 4.13 we developed a sensor marker board including a 9-axis IMU MPU9250 which is commonly used for orientation estimation applications and is composed of a 16-bit accelerometer with sampling frequencies from 4 Hz to 4 kHz and full-scale range from ±2 to ±16 G; 16-bit gyroscopes with sampling frequencies from 4 Hz to 4 kHz and full-scale range from ±250 to ±2000 °/s.

The IMU is mechanically coupled to the high speed digital 16-bit magnetic sensor KMX62-1031 which has a sampling frequency from 0.781 Hz to 1.6 kHz and a full-scale range of ±1200 µT.

This mechanical coupling allows the system to estimate the magnetic sensor orientation using the IMU data. The use of both external magnetic sensor and IMU may be considered redundant for marker miniaturization, which is a direct goal for any wearable system. However, this is mandatory due to the sampling rate limitations of the AK8963 integrated into the MPU9250 and of known commercially available IMU.

Then, we chose 800 Hz as the internal sampling frequency of the KMX62-1031 magnetic sensor, 100 Hz as the internal sampling frequency of the MPU9250 accelerometer and gyroscope, and finally, we set the field generator sinusoidal signal frequency at 100 Hz to reduce the artefacts in the sampled magnetic flux density signals.

We chose the ST Nucleo-F446RE evaluation board as the prototype processing unit since the included STM32F446RE 32-bit M4-Cortex MCU is a small footprint, low cost with 180 MHz maximum CPU frequency and 128 kB available RAM with floating point unit and multiple I2C and Serial Peripheral Interface (SPI) ports for multiple sensor markers connections and further extension of the prototype functionalities.

Therefore, the sensing module is composed by the designed sensor marker which is connected through I2C to the ST Nucleo-F446RE board that runs the real-time tracking algorithm sending the output data through Universal Serial Bus (USB) to a Laptop running Matlab as GUI.

The tracking algorithm was further developed parting from the starting point presented in the previous section, as shown in Fig. 4.14, in order to be implemented and run on board of the M4-Cortex MCU.

Prior to the device usage, the system axes orientation with respect to the Earth q_0 must be calculated using the IMU data and Madgwick's algorithm.

As previously clarified a first stage of the sensing module algorithm will sample the magnetic sensor at 800 Hz and filter it with a 82 coefficients Finite Impulse Response (FIR) LPF with 10 Hz bandwidth with 2.67 dB ripple and -71.40 dB attenuation at 30 Hz. Then, the filtered earth magnetic flux density, the IMU accelerometer and gyroscope measurements, and the previously computed system quaternion q0 will be used inside the

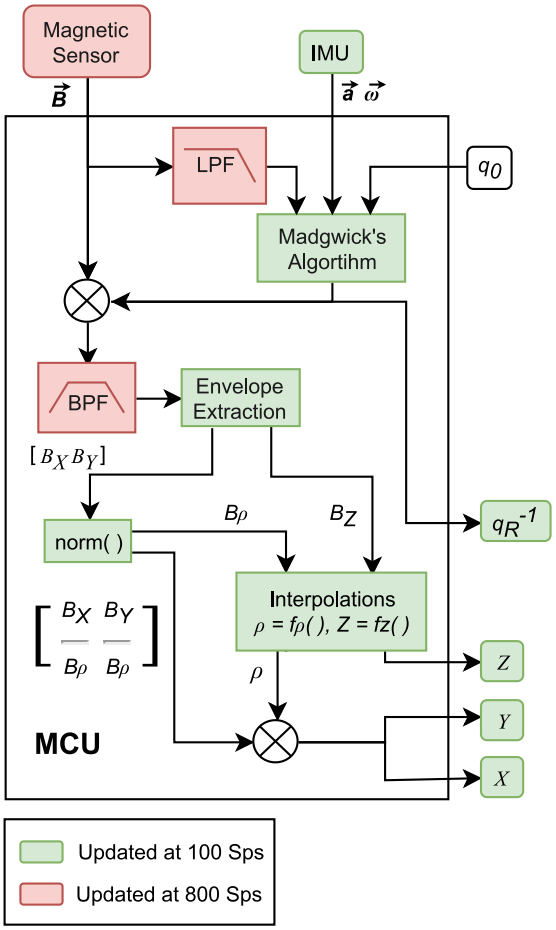

Figure 4.14: Algorithm implementation flowchart to estimate position and orientation of a single tri-axial magnetic and IMU sensor couple. ©[2020] IEEE.

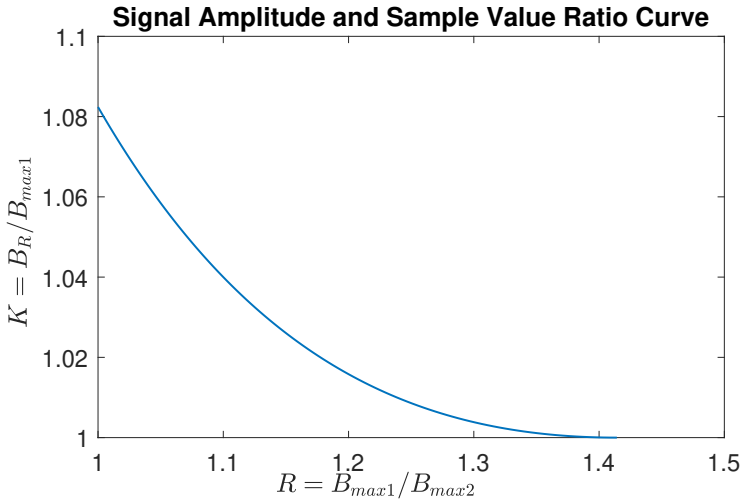

Figure 4.15: Representative curve of the existent relation between the sinusoidal signal and signal highest value sample ratio , and the signal highest and second highest value samples ratio from worst to best case scenario.

Madgwick's algorithm to compute the sensor couple relative quaternion q_R at a 100 Hz sample rate.

On a second stage, the raw magnetic sensor set of eight measurements is rotated by the conjugated quaternion q_R^{-1} and then is filtered with a 71 coefficients FIR BPF 30 Hz bandwidth around the variable magnetic field frequency $f_0 = 100\,\text{Hz}$ with 0.82 dB ripple and $-29.29\,\text{dB}$ attenuation, allowing the extraction of a single sine wave period.

A third stage will extract the $\vec{B_R}$ envelope from the filtered signal $\vec{B_R}(t)$ at a 100 Hz rate. For this purpose, we develop a solution alternative to the Hilbert transformation since as previously discussed its computational cost is non-trivial. Therefore, taking into account that we are asynchronously taking eight equally distant samples per each period of a sinusoidal signal, considering only the signal highest value sample B_{max1} we can get an envelope error of 7.58 % in the worst-case scenario where this sample is equal to the signal second-highest value sample B_{max2}.

Our solution to this specific problem was to study the existent relation be-

tween the ratio $K = \frac{B_R}{B_{max1}}$ and the ratio $R = \frac{B_{max1}}{B_{max2}}$, as shown in Fig. 4.15. Using Matlab Curve Fitting Toolbox we obtained Eq. (4.7) to calculate the envelope $\vec{B_R}$ from B_{max1} and B_{max2}, allowing a consistent and direct signal envelope estimation. Then, the envelope sign is computed comparing B_X and B_Z phase with B_Y phase.

$$\vec{B_R} = B_{max1}\,(9.402\,e^{-4.057\,\frac{B_{max1}}{B_{max2}}} + 0.8096\,e^{0.1276\,\frac{B_{max1}}{B_{max2}}}) \tag{4.7}$$

The final stage performs the regressions functions Eq. (4.1) from B_Z and $B_\rho = \sqrt{B_X^2 + B_Y^2}$, obtaining $\hat{\rho}$ and $\hat{Z}$ from which we can compute $\hat{X} = \hat{\rho}\,\frac{B_X}{B_\rho}$ and $\hat{Y} = \hat{\rho}\,\frac{B_Y}{B_\rho}$ and thus obtaining a 6DOF output including q_R with a 100 Hz output rate. To be taken into account is that this output rate can be incremented to 200 Hz by extracting the envelope from only half period of the signal.

As previously discussed, a key element of this development step is our implementation of the Scattered Interpolant method on board of the MCU. The first thing needed for this purpose is to form a $4 \times N$ array containing the set of points $\{\vec{B_i}\} = \{[\,B_{\rho i},\, B_{Zi}\,]\}$ and $\{\vec{P_i}\} = \{[\,\rho_i,\, Z_i\,]\}$, where N is the number of points. This array is called Point List.

Then a $3 \times M$ array is formed containing the Point List indexes of the vertices forming each of the M triangles of the Delaunay Triangulation. This array is called Connectivity List. Within the Connectivity List another $3 \times M$ array is stored containing the indexes of the three neighbour triangles.

Therefore, the final form of the Connectivity List is a $6 \times M$ array, where M is the number of triangles of the Delaunay Triangulation, and each array line contains the correspondent triangle information consisting in

three Point List indexes of the triangle vertices and three Connectivity List indexes of the three neighbour triangles for each triangle.

In order to evaluate if a measured point $\vec{B_k}$ is inside a givenn triangle, we need to consider a single vertex of that triangle $\vec{B_0}$ and the vectors formed from $\vec{B_0}$ to the other two vertices, $\vec{v_1} = \vec{B_1} - \vec{B_0}$ and $\vec{v_2} = \vec{B_2} - \vec{B_0}$ respectively.

$$\vec{B_k} = a\vec{v_1} + b\vec{v_2} \tag{4.8}$$

Then expressing the vector between $\vec{B_k}$ and $\vec{B_0}$ in terms of $\vec{v_1}$ and $\vec{v_2}$ results in Eq. (4.8), where a and b are constants. Solving for these constants we obtain Eqs. (4.9-4.10).

$$a = \frac{\det(\vec{B_k}\,\vec{v_2}) - \det(\vec{B_0}\,\vec{v_2})}{\det(\vec{v_1}\,\vec{v_2})} \tag{4.9}$$

$$b = -\frac{\det(\vec{B_k}\,\vec{v_1}) - \det(\vec{B_0}\,\vec{v_1})}{\det(\vec{v_1}\,\vec{v_2})} \tag{4.10}$$

If the conditions $a \geq 0$, $b \geq 0$ and $a + b \leq 1$ are given, the point $\vec{B_k}$ belongs to the evaluated triangle. In order not to test every single triangle for every measured point, we used a and b to optimize the triangle evaluation algorithm as follows:

- If $a+b > 1$, the next triangle to be evaluated is the neighbour triangle opposed to $\vec{B_0}$.
- If $b < 0$ and $b < a$, the next triangle to be evaluated is the neighbour triangle opposed to $\vec{B_2}$.
- Else, the next triangle to be evaluated is the neighbour triangle opposed to $\vec{B_1}$.

Table 4.1: Comparison of Different Scattered Interpolations of Functions $f_\rho(B_\rho, B_Z)$ and $f_Z(B_\rho, B_Z)$. ©[2020] IEEE.

Grid spacing (mm)	**# points**	**# triangles**	**Precision**	**Memory Size (kB)**	**RMSE (mm)**
1	302960	605876	Floating Point	24236	-
			Fixed Point	9694.2	0.0475
5	3080	6130	Floating Point	245.79	0.419
			Fixed Point	98.2	0.422
10	784	1541	Floating Point	62.189	0.8313
			Fixed Point	24.764	0.8322

This optimization will reduce the iterations to find the correspondent triangle T_k. A second optimization is using T_k as the initial evaluated triangle for the next measured point $\vec{B_{k+1}}$.

Once the correspondent triangle T_k is located, the linear surface interpolations are performed as detailed by Amidror (2002), using $\vec{B_k}$ the surfaces denoted by the vertices $[\vec{B_{0\rho}},\ \vec{B_{0Z}},\ \rho]$, $[\vec{B_{1\rho}},\ \vec{B_{1Z}},\ \rho]$ and $[\vec{B_{2\rho}},\ \vec{B_{2Z}},\ \rho]$ to obtain the estimated coordinate $\hat{\rho}$; and the vertices $[\vec{B_{0\rho}},\ \vec{B_{0Z}},\ Z]$, $[\vec{B_{1\rho}},\ \vec{B_{1Z}},\ Z]$ and $[\vec{B_{2\rho}},\ \vec{B_{2Z}},\ Z]$ to obtain the estimated coordinate $\hat{Z}$.

As previously discussed, to run these functions on a MCU it is possible to use only a limited number of points to form the scattered interpolation of the regression functions in Eq. (4.1). The trade-off, in this case, resides in the chosen number of points to build the scattered interpolations and the consequent needed memory space and accuracy. The required memory can be estimated as the Point List array of $4 \times N$, plus the Connectivity List array of $6 \times M$.

Tab. 4.1 compares the required memory space and RMSE of each one of the scattered interpolations created using both floating-point and 16-bit fixed-point precision for both points and triangles information arrays, and different spacing grids with respect to the ideal interpolation created with floating-point precision and a grid spacing of $\Delta_\rho = \Delta_Z = 1\,\text{mm}$.

It can be seen that using a fixed point precision introduces a negligible error in comparison to the error introduced by the use of a higher grid spacing. Since the available RAM size is of 128 kB we chose to implement the scattered interpolation formed with a spacing grid of $\Delta_\rho = \Delta_Z = 10\,\text{mm}$ for a range of $3\,\text{cm} \leq \rho \leq 30\,\text{cm}$ $3\,\text{cm} \leq Z \leq 30\,\text{cm}$, since it only introduces a theoretical error lower than 1 mm and biomedical application might require to extent the range over than 30 cm requiring more memory space for the spacing grids calculated in Tab. 4.1.

4.4.1 Experimental Tests

The experimental tests for this prototype were done placing the system on top of a table without the presence of additional strong magnetic field sources or ferromagnetic materials that could distort the generated magnetic field, inside a room of $3\,\text{m} \times 4\,\text{m} \times 3\,\text{m}$ with 9 VICON cameras placed at 3 m height allowing the tracking of retro-reflective markers with a 1 mm accuracy and 0.1 mm precision.

As observed in Fig. 4.17 the designed sensor marker is placed in a 3D-printed holder to place three retro-reflective markers aligned with the sensor marker X and Y axes at the same height with known distances to the magnetic sensor.

A retro-reflective marker is placed on top of the designed bobbin coil to

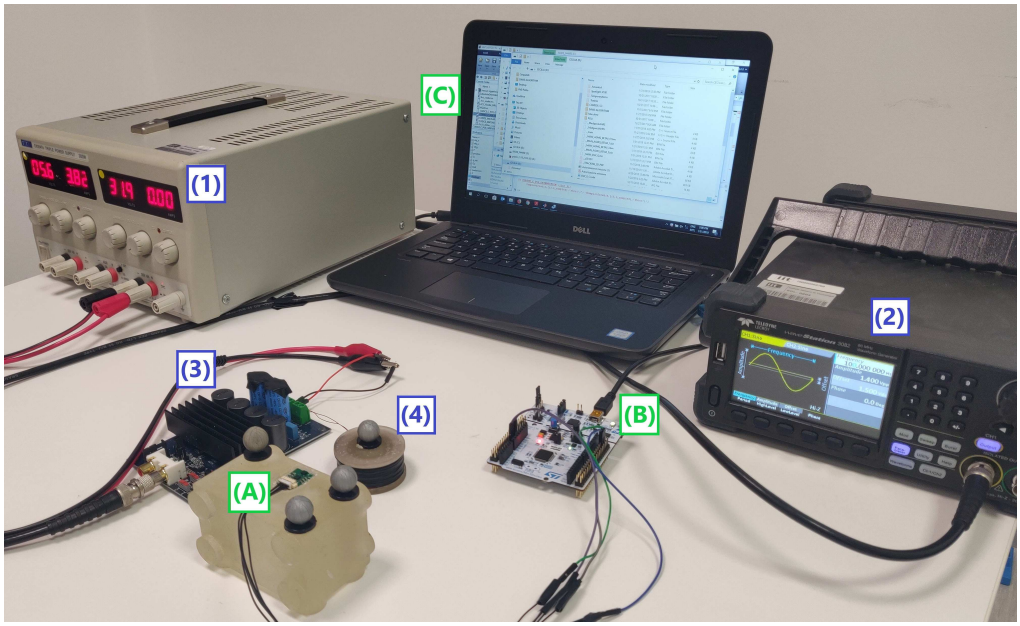

Figure 4.16: Validation system test set-up. Field generator module comprising: (1) Power supply, (2) Signal generator, (3) Signal amplifier and (4) Bobbin coil. Sensing module comprising (A) Sensor board, (B) MCU and (C) Laptop running as GUI. ©[2020] IEEE.

mark the magnetic tracking system origin in the XY plane with a measured bias in the Z axis, and three additional markers are placed on top of the used table to fix the optical system axes during the test. Therefore, using a total of seven retro-reflective markers during the experimental tests. A static accuracy test was performed covering an overall volume of 20 cm × 20 cm × 14 cm, using 95 different measurement points as shown in Fig 4.18a, resulting in an average spatial accuracy $\epsilon_S = 7.8$ mm within a maximum measured distance of 21 cm.

Then, an orientation accuracy test was performed as described in the previous chapter in the presence of the oscillating magnetic field at distance ranging between 10 cm and 15 cm from the bobbin coil. As specified by Madgwick et al. (2011), the performance of Madgwick's algorithm in the estimation of the IMU sensor orientation greatly relies on a proportional coefficient of the algorithm loop β, which balances the influence of the gyroscope data (self-referenced dynamic data) over the accelerometer and

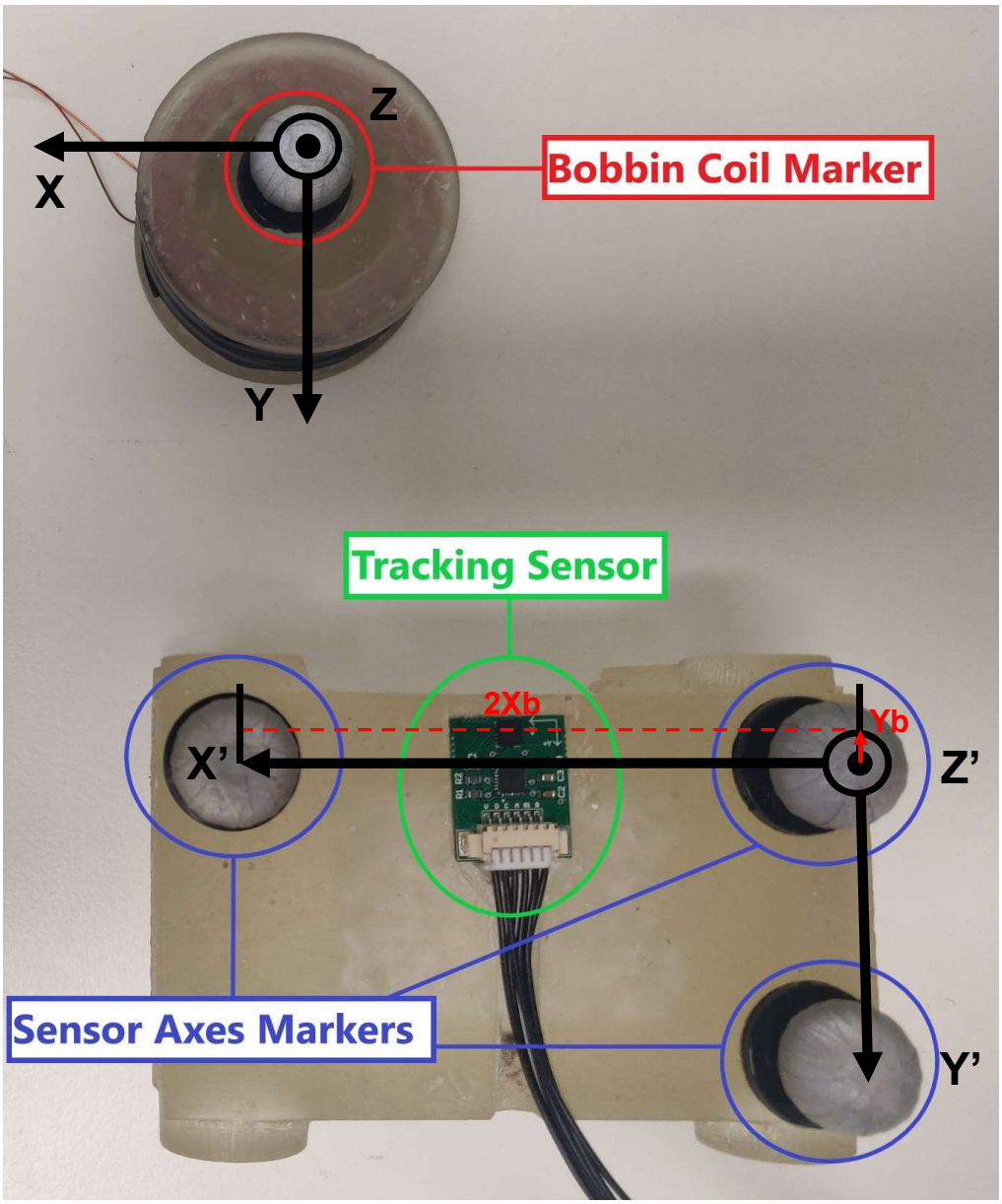

Figure 4.17: Retro-reflective markers are used on the system prototype: one marker is placed in the center of the bobbin coil axis, three are placed aligned with both X and Y sensor axes, and three extra markers are used to fix the VICON system axes.

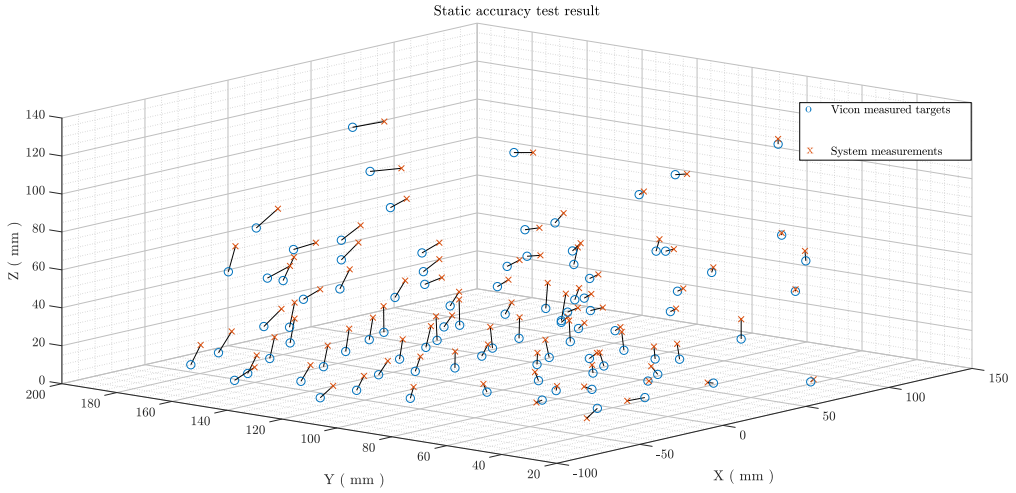

(a)

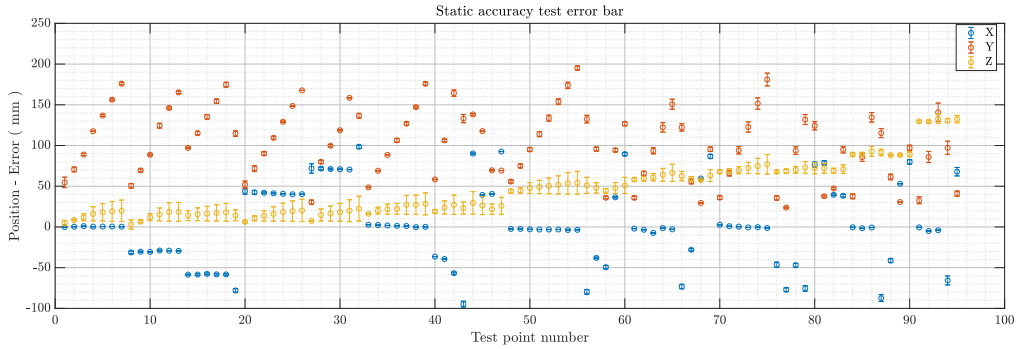

(b)

Figure 4.18: Static accuracy experimental test results. VICON measured targets are marked with blue circles, while system outputs are marked with orange crosses and the distance between them is marked with a black line. ©[2020] IEEE.

magnetic sensor data (earth referenced static data). Therefore, we need to consider this to test the sensor orientation accuracy independently, to choose the proper β set up for the dynamic accuracy test.

The averaged sensor orientation accuracy values obtained were 2.15°, 1.89°, 1.78°, 1.94° and 1.92° for β values 0.01, 0.1, 0.2, 0.3 and 0.5 respectively. Results show that $\beta = 0.2$ is the optimal value obtained for a minimum orientation error $\epsilon_R = 1.78°$ which is a very close result to the $\epsilon_R = 1.7°$ reported by Madgwick et al. (2011).

Finally, a dynamical accuracy test was performed as described in the previous chapter using the VICON motion capture system measurements as ground truth, recording four different types of movements inside half a cylinder volume of 20 cm radius and 13 cm height, a "T Movement" test, where the sensor is moved in parallel to the table plane, first in parallel to the Y axis and then in parallel to the X axis; a "Circle Movement" test, where the sensor is moved in parallel to the table plane following a circular form; an "Arc Movement" test, where the sensor is moved to form arcs traces inside the tracking space; and an "Arbitrary Movement" test, where the sensor is moved arbitrarily for 5 seconds inside the tracking space.

Dynamical accuracy measurement results are shown in Tab 4.2, obtaining an average dynamical accuracy $\epsilon_D = 7.6$ mm, which is consistent with the static accuracy result. Fig 4.19 shows the four best test recording outputs of both VICON and the prototype system.

4.4.2 Results Discussion

The static accuracy measurement result is comparable with our previous 2D prototype with the difference of performing with 6DOF. As shown in

Table 4.2: Dynamic Accuracy Measurements

Test Number	**Movement Type**	ϵ_D (mm)
1	T Movement	6.4
2	T Movement	6.9
3	T Movement	6.2
4	T Movement	5.3
5	Circle Movement	8
6	Circle Movement	7.1
7	Circle Movement	6.7
8	Arc Movement	7.5
9	Arc Movement	8.9
10	Arc Movement	10.4
11	Arbitrary Movement	7.5
12	Arbitrary Movement	9.4
13	Arbitrary Movement	7.9

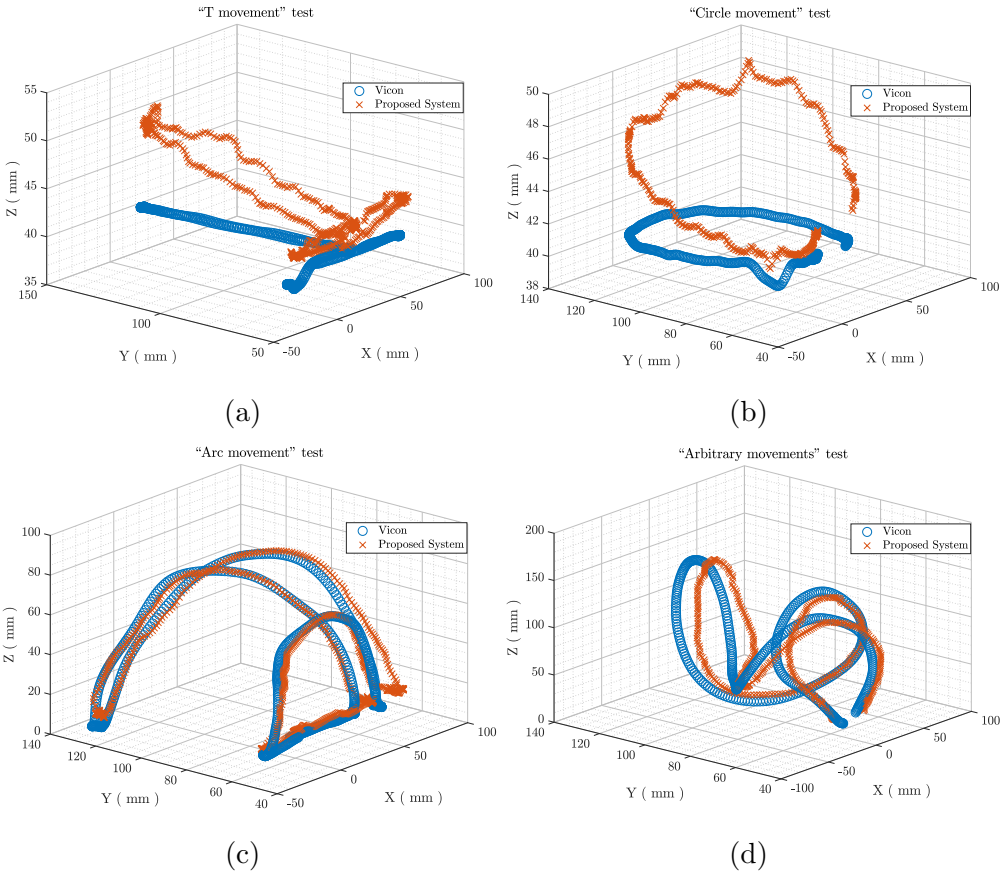

Figure 4.19: Dynamic accuracy experimental test results. "T movement" best test performance (a). "Circle movement" best test performance (b). "Arc movement" best test performance (c). "Arbitrary movements" best test performance (d). ©[2020] IEEE.

Fig. 4.18b we can observe that the major contribution to spatial error comes from the Z coordinate. Furthermore, we can observe that X and Y data, which directly depend on ρ, show a growing error as the test point gets further away from the system origin. This may correspond with used scattered interpolations computed from FEM simulations which do not correspond completely to what is being measured.

As previously mentioned, orientation accuracy results show that $\beta = 0.2$ is the optimal value obtained for a minimum orientation error $\epsilon_R = 1.78°$ which is a very close result to the $\epsilon_R = 1.7°$ reported by Madgwick et al. (2011).

While for the dynamical test results, we can observe that the proposed system can approximately follow the sensor movements. As the sensor gets further away from the system origin results shows a growing position error, more evident in the Z axis in comparison to the XY plane, supporting the previous observation taken from the static accuracy test that FEM simulations do not correspond entirely to the generated magnetic field.

To try to identify the main error source, we used the static accuracy test position points inside the FEM simulation to compute their correspondent simulated magnetic flux density values $[B_{\rho sim}, B_{Zsim}]$ and compare with the measured magnetic flux values $[B_{\rho meas}, B_{Zmeas}]$.

As a linear relation between simulated and measured magnetic flux densities is not found, potentially explaining the origin of the difference between simulated and measured magnetic flux density values, we concluded that the scattered interpolation of the regression functions Eq. (4.1) needs to be modified to match the measured magnetic flux density values and enhance system performance.

For this purpose two approaches are possible, in particular:

1. Entirely reconstructs the regression functions by substituting the simulated data sets with measured magnetic flux density on each position point of the desired grid.

2. Use a representative number measurements to form a data set of position points and magnetic flux density measurements in our tracking space of interest. Compute FEM simulations of the magnetic flux density on each position point of the data set. Then find a regression relationship between the FEM simulation results and the measurements obtained on the same position points and finally enable a generalized fitting that uses as input the FEM simulation results and as target the measurements taken.

The first approach has the drawback of being unpractical at the moment of forming the data set because it requires the correct positioning of the sensor in each of a large data set of position points.

Instead, the second approach has the advantage of adapting (calibrating) the large simulated data set of the previous regression functions using a smaller data set of the measured magnetic flux density.

The following section will describe in detail the performed calibration procedure, as well as its impact on the static and dynamical system accuracy.

4.5 Calibration Procedure and 6DOF System Characterization

In the previous section, we described the development of our first 6DOF magnetic tracking prototype embedded onboard a MCU and focused on evaluating the prototype static and dynamic accuracy performance. We concluded that to enhance the system accuracy performance the scattered interpolation of the regression functions Eq. (4.1) needs to be modified to match the measured magnetic flux density values.

In this section, we will present our calibration methodology to adapt the used scattered interpolations data sets to the measured magnetic flux density during the experimental test. Such a procedure is expected to enhance the system's spatial accuracy without impacting the tracking algorithm's computational complexity or the required memory space. Partial content of this section is reprinted from (Fernandez G et al., 2020) ©IEEE.

For the purpose of calibrating the scattered interpolation data sets, two approaches were proposed, the first one focusing on totally reconstructing the scattered interpolation data set parting using only measured magnetic flux density values, and the second approach focusing on adapting the current data set by finding a regression relationship between the FEM simulated and measured magnetic flux density values.

As previously mentioned, the first approach major drawback is that it represents an unpractical procedure at the moment of forming the data set because it requires the correct positioning of the sensor and sensor position measurement in each of a large data set of positions points, while the second approach has the advantage of adapting the large simulated data set of the previous regression functions using a smaller data set of the

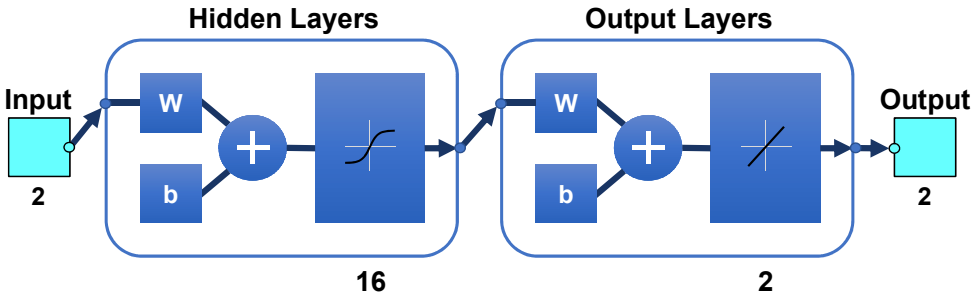

Figure 4.20: Feed-Forward Two-Layer 16 neurons Neural Network used to calibrate scattered interpolations data set.

measured magnetic flux density.

Therefore, we chose to follow the second approach because of its inherent viability and thus, the possibility of re-using the large data set obtained in FEM simulation.

Using thirty-nine of the ninety-five static test measurement, a data set directly related to the generated magnetic field is formed covering test positions points in the ranges $47\,\text{mm} \leq \rho \leq 160\,\text{mm}$ and $8\,\text{mm} \leq Z \leq 130\,\text{mm}$.

There were not any identifiable mathematical relations between the correspondent vectors $[B_{\rho sim},\ B_{Zsim}]$ and $[B_{\rho meas},\ B_{Zmeas}]$ extracted at the same position point, that could be used for simple regression fitting techniques.

Hence, we have chosen to form a two-layer feed-forward two-inputs two-outputs and sixteen neurons NN using Matlab Neural Net Fitting app as shown Fig. 4.20. The NN is trained using as input the simulated magnetic flux density values computed on a known set of position points, formed from thirty-nine of the ninety-five static accuracy test position points and as targets the magnetic flux density measured on the same set of position points. A Bayesian Regularization algorithm was implemented with 70% samples used for training and 30% used for testing, reaching a final perfor-

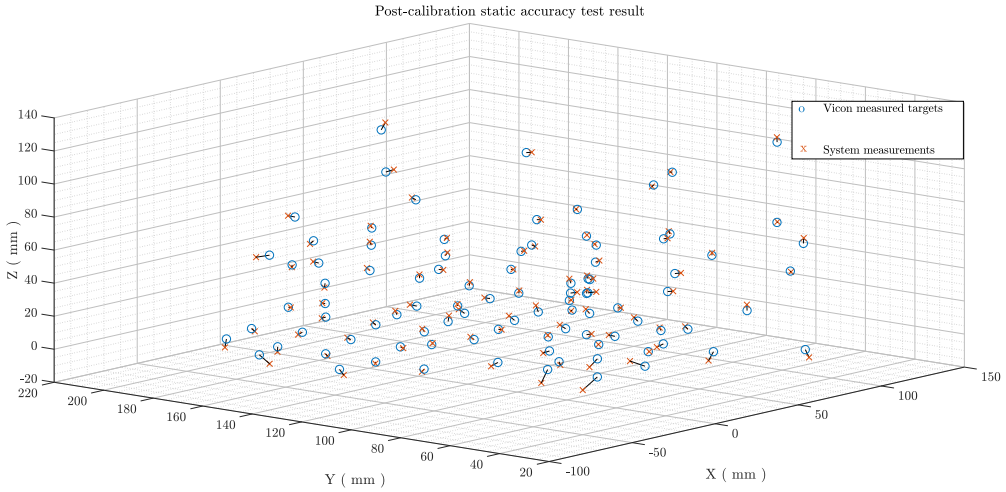

(a)

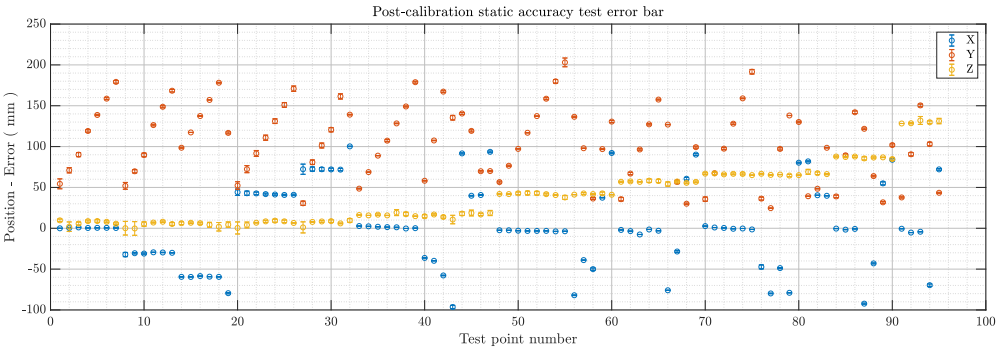

(b)

Figure 4.21: Post-calibration static accuracy experimental test results. Referenced targets are marked with red circles, while system outputs are marked with red crosses and the distance between them is marked with a black line. ©[2020] IEEE.

mance RMSE of 2.8 µT parting from an initial RMSE value of 376 µT.

Finally, the trained NN is fed with the uncalibrated regression functions magnetic flux density data set, generating a new data set to form the calibrated regression functions. These regression functions are now optimized to work with the magnetic field measured during the static accuracy test.

Table 4.3: Post-Calibration Dynamic Accuracy Measurements

Test Number	**Movement Type**	ϵ_D (mm)
1	T Movement	3
2	T Movement	3.9
3	T Movement	3.6
4	T Movement	2.7
5	Circle Movement	5.7
6	Circle Movement	3.4
7	Circle Movement	4.7
8	Arc Movement	7.4
9	Arc Movement	8.4
10	Arc Movement	10.4
11	Arbitrary Movement	5.1
12	Arbitrary Movement	6.4
13	Arbitrary Movement	5.4

4.5.1 Post-Calibration Test Results

Using the previously recorded test data with the calibrated scattered interpolation of regression functions Eq. (4.1), new static and dynamic accuracy test results were obtained. Fig. 4.21 shows the post-calibration static accuracy test results. In comparison to the previous results shown in Fig. 4.18a we observe that the responses are closer to the target points in the covered tracking space.

The resulting system static accuracy after calibration is $\epsilon_S = 2.6\,\text{mm}$. This represents a relative error of 1.23% the maximum tracked distance (21 cm) and proves that the system performance improved with the executed calibration procedure. Comparing to the pre-calibration relative error of 3.71% we obtain a 200% accuracy gain. Fig. 4.21b shows the system accuracy enhancements both on the Z axis and on the XY plane for the test point positioned farthest from the system origin, compared to Fig. 4.18b.

Post-calibration system performance enhancement is also highlighted in Tab. 4.3 which shows the results of each dynamical test, from which we

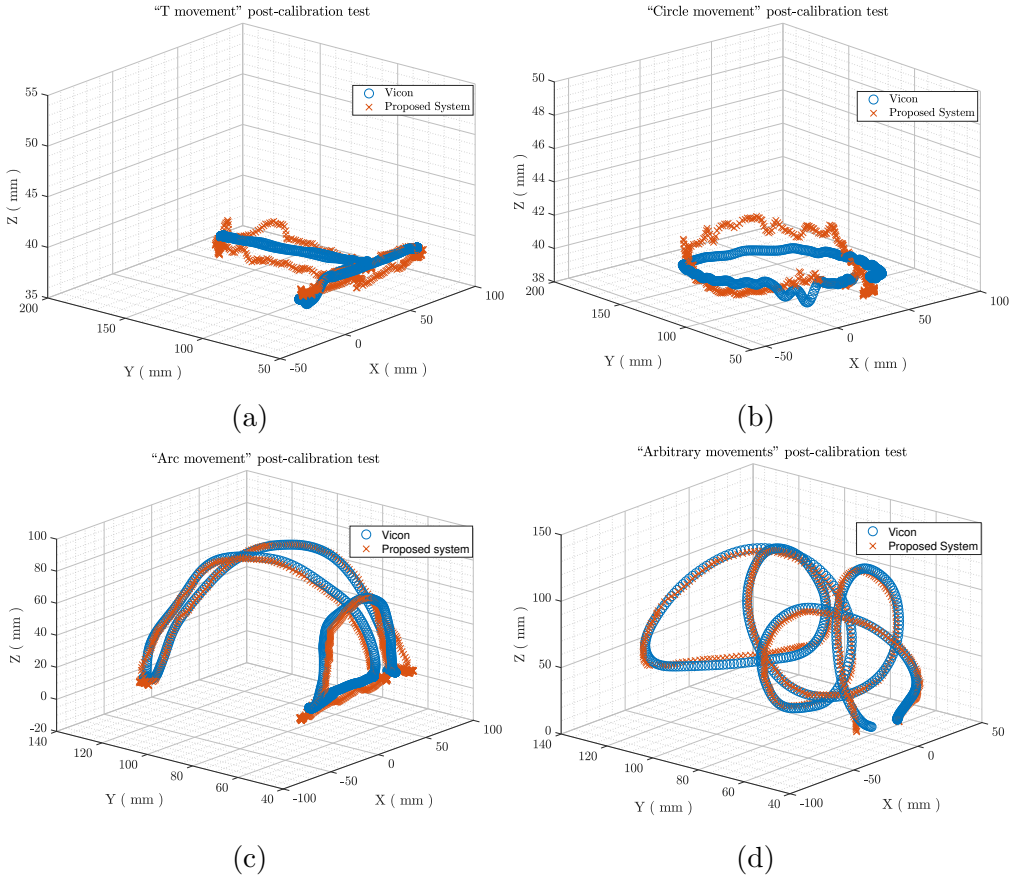

Figure 4.22: Post-calibration dynamic accuracy test results. "T movement" best test performance (a). "Circle movement" best test performance (b). "Arc movement" best test performance (c). "Arbitrary movements" best test performance (d). ©[2020] IEEE.

obtained an average dynamical accuracy $\epsilon_D = 5.4\,\text{mm}$, highlighting a 40.7% accuracy gain from the pre-calibration test results.

The improvement on the Z coordinate estimation is more evident on Fig. 4.22a and Fig. 4.22b compared to Fig. 4.19a and Fig. 4.19b respectively. While the "Arc Movement" test of Fig. 4.22c shows only a slight improvement both numerically and graphically compared to Fig. 4.19c. Meanwhile, the "Arbitrary Movement" test show a more evident improvement after calibration. As shown in Fig. 4.22d the proposed system can follow properly very complex traces after the performed calibration.

At this development point we have 6DOF magnetic tracking system based

on using a M4-Cortex MCU as processing unit capable of performing in real-time with an USB output, a data rate 100 Hz, a maximum latency of 12 ms, static accuracy performance 2.6 mm, orientation accuracy performance 1.78 ° and dynamical accuracy performance 5.4 mm.

The next development phase will consist of implementing a viable low power wireless communication protocol to send $\vec{P}$ estimated position vector data and q_R estimated quaternion orientation data consistently to the end-user device.

4.6 BLE Communication and Raspberry Pi GUI Implementation

In previous sections, we have described the development of a 6DOF magnetic tracking system embedded on board of an M4-Cortex MCU capable of performing in real-time with a data rate 100 Hz, a maximum latency of 12 ms, static accuracy performance 2.6 mm, orientation accuracy performance 1.78 ° and dynamical accuracy performance 5.4 mm.

However, at this development point, the system can only transmit the output data through serial communication. Therefore, in this section, we will describe the implementation of a wireless interface to enable communication between the tracking system wearable tracking unit and the end-user device. Partial content of this section is reprinted from (Fernandez G et al., 2020) ©IEEE.

We considered BLE in a first instance since it has been widely and continuously in low power consumption wireless device and our aim of designing a wearable device requires the use of a small footprint battery capable of

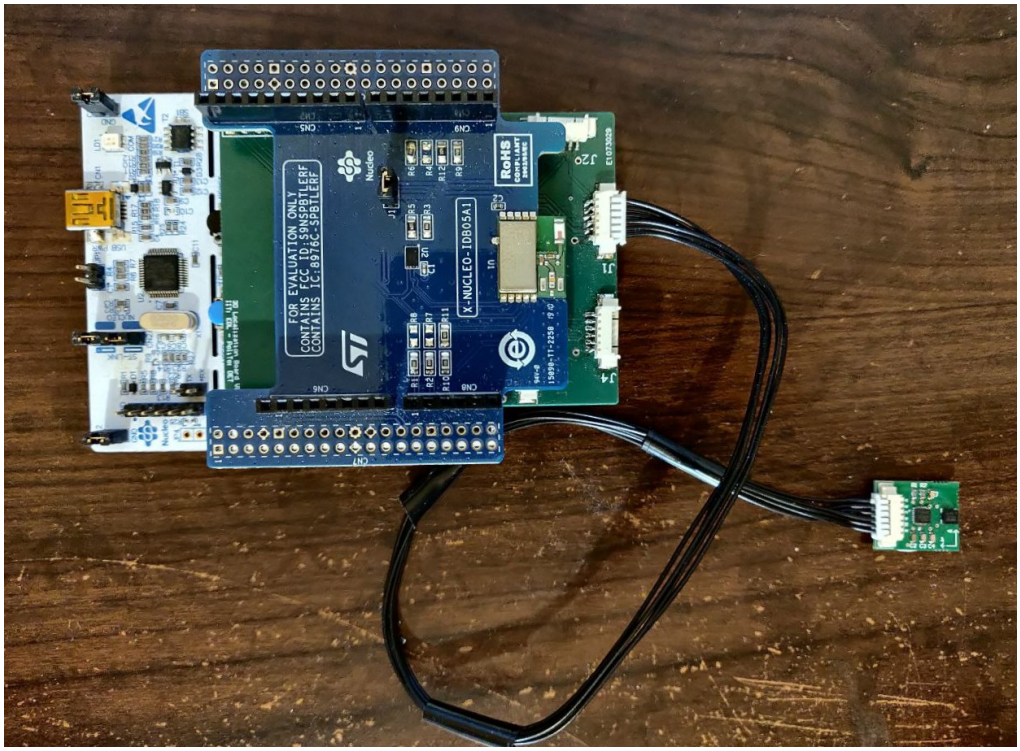

Figure 4.23: X-NUCLEO-IDB05A1 expansion board stacked on top of ST Nucleo-F446RE board connected to the sensor marker through designed I2C port connection board.

powering the device through a usable functioning time.

In order to continue a fast system prototyping and test the feasibility of replacing the USB data transmission with BLE communication, we stacked an ST X-NUCLEO-IDB05A1 expansion board on top of our ST Nucleo-F446RE board, as shown in Fig. 4.23. This board interfaces the STM32F446RE MCU with a SPBTLE-RF network processor module that includes an embedded protocol that enables BLE v4.2 compliant communication for the sensing module of our prototype.

To be considered first is the size of the payload to be transmitted. The system estimated sensor position consists of three 16-bit precision words, this is motivated to keep the available magnetic sensor precision, to avoid overflowing the FIR filters running inside the 32-bit processor and use less RAM space for the scattered interpolations for virtually the same accuracy

as shown in Tab. 4.1.

The sensor orientation represented as quaternion q_R consists of four floating-point variables with values between -1 and 1, that are converted to 32-bit fixed-point precision words by performing the product $\hat{q_R} = 2^{30}\, q_R$ before sending them to the end-user device through the serial port.

Therefore, our sensor data payload consists of 22 bytes which would need a minimum data transmission of 17.6 kbps to update the data sensor at 100 Hz. In accordance to Tosi et al. (2017) study, BLE v4.2 presents a maximum data throughput of 236.7 kbps, this would theoretically allow the transmission of 13 sensors payload as maximum.

For this reason we tried implementing a custom service with seven characteristics X, Y, Z, q_{R0}, q_{R1}, q_{R2} and q_{R3} in order to broadcast as notifications the sensor position and orientation data updated at 100 Hz. We used the BLE Analyser smartphone application to verify the correctness of the transmitted sensor data, which were received correctly demonstrating the wireless communication capabilities of our system.

However, through further analysis, we realized that after a few minutes the firmware started malfunctioning due to the large overhead time required to broadcast the seven characteristics custom service. Therefore, we recurred to use an available service to enable Universal Asynchronous Receiver Transmitter (UART) access over BLE capable of sending 20-byte data packages with an overhead time around 2 ms. Since our sensor 6DOF estimation data is composed of 22 bytes it needs to be divided to be transmitted using the UART service.

In order to develop a safe and stable implementation while keeping the tracking accuracy performance achieved, we kept running internally the

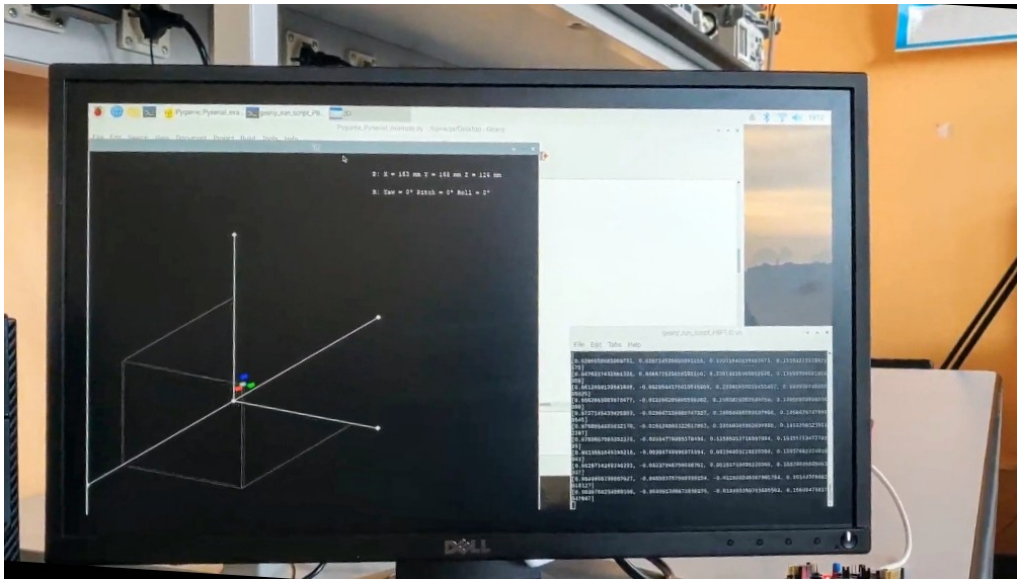

Figure 4.24: Graphical interface run in real-time on board a Raspberry Pi 3 to show 6DOF sensor data.

algorithm shown in Fig. 4.14 and transmitting only either the sensor position $\hat{P}$ or the sensor relative orientation q_R, alternating between them every output update iteration. However, this solution reduces the output update rate from the initial 100 Hz to 50 Hz, but this is still acceptable for human motion tracking. In case the higher update rate would be required, the quaternion q_R could be transformed to the Tait–Bryan angles as shown in (3.21-3.23), reducing the payload size from 22 to 18 bytes.

In order to receive and assess graphically the 6DOF sensor data sent through the UART service, we developed a simple GUI on board of a Raspberry PI 3 embedded system, as shown in Fig. 4.24. It consists of a python script capable of connecting to our BLE device, decoding the payload of the UART and rendering an axonometric projection of the estimated sensor position and orientation.

This implementation performed optimally without showing any connection error between the devices. Using a smartphone camera capable of video capturing at 480 fps we measured the latency between the sensor being

moved from a resting state and the graphical reaction to this movement shown in the GUI, with results varying between 106 ms and 150 ms.

Another aspect of interest for a wearable device is its power consumption, therefore we measured the current flowing into the ST Nucleo-F446RE board while being used. The overall measured current consumption during sensor 6DOF estimation and data transmission through USB was of 42.4 mA, while the overall measured current consumption with BLE v4.2 data transmission was of 51.1 mA.

Therefore, with this last step, we have achieved the prototype development of a functional wireless 6DOF magnetic tracking system with measured 2.6 mm static spatial accuracy, 1.78 ° orientation accuracy within a 21 cm radius, a maximum measured latency of 150 ms and processing unit current consumption of 51.1 mA.

4.7 Final System Characteristics Discussion

There exist too many singular characteristics to compare different tracking systems such as spatial accuracy, range, DOF, markers volume or the use of wireless markers. Therefore, in this section, we introduce a Figure Of Merit (FOM) Γ to compactly enable the designed tracking system performance and wearability in comparison to state-of-the-art devices either commercially available and research developed. Partial content of this section is reprinted from (Fernandez G et al., 2020) ©IEEE.

The FOM focuses on both system accuracy and range, but at the same time highlighting the systems wearability and flexibility of use. which are the main characteristic our proposed system algorithm and hardware ar-

Table 4.4: Magnetic Tracking System State-of-the-Art Comparison.

System	**Spatial Accuracy (mm)**	**Range (cm)**	**DOF**	**Marker Volume (mm^3)**	**Γ (mm^3)**	**WM**
Patriot	1.524	91.4	6	$28.3 \times 22.9 \times 15.2$	2.74	No
Aurora	0.88	50	6	$19.8 \times 7.9 \times 7.9$	0.36	No
TrakSTAR	1.4	66	6	$19.8 \times 7.9 \times 7.9$	0.44	No
Chen et al. (2016)	1.33	12	3	$10 \times 5^2 \times \pi$	2.9	No
G4	2	100	6	$28.3 \times 22.9 \times 15.2$	20.47	Yes
G4 μ-sensor	10.16	150	6	$10 \times 0.9^2 \times \pi$	0.029	Yes
Patriot Wireless	7.5	76.2	6	$88.9 \times 42.2 \times 24.6$	151.4	Yes
Huang et al. (2016)	1	20	6	4000	3.34	Yes
Yoon et al. (2016)	8.6	12	6	$35 \times 22 \times 25$	229.9	Yes
Liang et al. (2012)	0.42	10	5	$30 \times 4^2 \times \pi$	1.27	Yes
Andria et al. (2020)	0.2	70	6	$19.8 \times 7.9 \times 7.9$	0.058	No
This work	**2.6**	**21**	**6**	$18 \times 15 \times 2$	**1.11**	**Yes**

chitecture focuses on. We defined the FOM as,

$$\Gamma = \frac{\epsilon_S}{R} \frac{V_M}{DOF} \tag{4.11}$$

The first term of Γ includes the position static accuracy ϵ_S of the tracking device since this is the main performance indicator. Considering that the performance of magnetic tracking decays with the sensor to field generator distance, Γ is proportional to static accuracy ϵ_P over the tracking range R ratio.

The second term accounts for the device markers' wearability and usage flexibility. This comprises the marker volume V_M (in the nominator), as with a higher sensor volume the system becomes less useful for wearable applications. To unify the evaluation criteria among the reported magnetic tracking systems, we take into account only the tracked marker volume, as it is supposed to be worn in parts of the body that significantly move. Finally, the second term denominator comprises the system DOF to indicate a Γ improvement as DOF increases.

Tab 4.4 compares the state-of-the-art systems with our prototype in terms of spatial static accuracy (mm), tracking range (cm), degrees of freedom, the system marker volume, the capability of wireless communication between tracking markers or wearable processing unit and the end-user device and Γ.

We observe that by using the FOM Γ as an indicator, our system is ranked only fifth in a list of devices composed of several commercial and research-developed systems. This can be considered a very good result for such a low complexity and non-optimized prototype made with off-the-shelf components. Moreover, compared only to wireless systems the prototype ranks

only second w.r.t. the magnetic tracking system gold standard Polhemus G4 using deeply engineered micro-sensors.

Observe also that on Tab. 4.4 most of the compared system algorithms are run on a CPU or a GPU: Polhemus G4 transmits the sensed data wirelessly to the user CPU and process all data in the end-user device. While our system runs the tracking algorithm directly on the sensor module, particularly on a Cortex-M4 as we focus on the wearability and portability of the solution with consistent performance regardless of the end-user device capabilities.

Moreover, taking into account the off-the-shelf components composing our system: a KMX62-1031 magnetic sensor, two MPU-9250 IMU, two X-NUCLEO-IDB05A2 development boards, two NUCLEO-F446RE development boards and a STEVAL-CCA044V1 power amplifier board; we can approximate our prototype system initial cost below $150. In comparison to industry gold standard systems which costs can go above $12500 (Romero et al., 2017), our tracking methodology presents an affordable solution that with further system optimization could replace the use of industry gold standard instruments for the development of low-cost medical instrumentation and research assessment tools with off-the-shelf components.

Observe that our last prototype development includes a BLE v4.2 compliant communication module. However, further optimizations are possible and need to be considered in further studies, in particular on a battery life-latency trade-off basis. We consider this stage as a starting point for multi-sensing and system upgrade and optimization, for example regarding the use of a BLE v5 module.

Bulić et al. (2019) reports maximum data throughput for BLE v5 between

1.3 Mbps and 800 kbps using notifications. These data rates capabilities would allow our system to transmit a higher payload and increase the sensor data update rate and the number of the sensor data payload to transmit. Therefore, our solution remains a very good candidate to enable precise tracking of a considerable number of nodes simultaneously, as in finger tracking applications.

We can conclude that there is still space for improvement by further enhancing calibration in order to enhance the system tracking accuracy. Another viable option would be to use magnetic sensors with a higher resolution, while maintaining the low volume of the sensing module and a sampling rate equal or higher than the current sensor sampling rate.

Moreover, we understand that we have achieved a general solution useful for biomedical applications that still need to be enhanced through application-driven re-designing process, where the characteristics of the solution, for example, accuracy, range, wireless communication availability, number of sensors or system footprint size; can be weighted in accordance to the specific application.

In the following section, we will describe an ongoing project where our tracking system solution will be used for biomedical applications thanks to the achieved tracking capabilities and the system components' low cost. Furthermore, we will show the preliminary application-driven re-designs applied to our system to achieve a better solution.

4.8 Future Work and Application-Driven Preliminary Designs

In this section, we will present two system design modifications to enhance the presented system characteristics. As concluded in the previous section we have achieved a general solution that has space for improvements and reworking. Moreover, we understand that this process must be driven by the specific applications that will employ the tracking solution.

Therefore, we will introduce a biomedical application project currently in development for which our tracking system is planned to be used due to its tracking capabilities at a lower cost than current market solutions. Along with the project's general characteristics and motivation we will present the preliminary redesign studies driven by each specific application.

This project consists of a computer-assisted prenatal ultrasound procedure training assessment system. The motivation of this project comes from the discomfort endured by numerous patients during prenatal ultrasound procedures performed by inexpert clinicians. The main target is to create an assessment tool capable of quantitatively evaluate the clinicians' performance of prenatal ultrasound during training simulations.

For this purpose, as shown in Fig. 4.25, it is intended to fuse an ultrasound probe with a pressure sensor and a tracking marker to correlate in time the obtained ultrasound image with the probe 6DOF data and the applied pressure. This will allow evaluating how the clinician can manage and position the ultrasound probe to get a clear image by applying the minimum required pressure.

Our system will be in charge to provide the probe 6DOF information. For

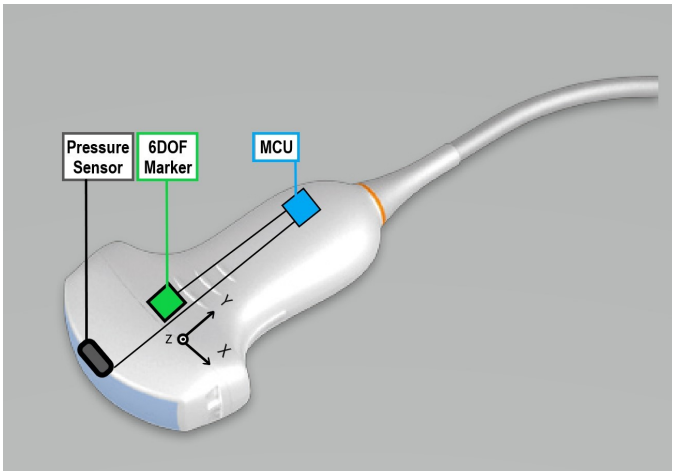

Figure 4.25: Visual example of ultrasound probe with 6DOF tracked marker and pressure sensor for prenatal echography simulation assessment.

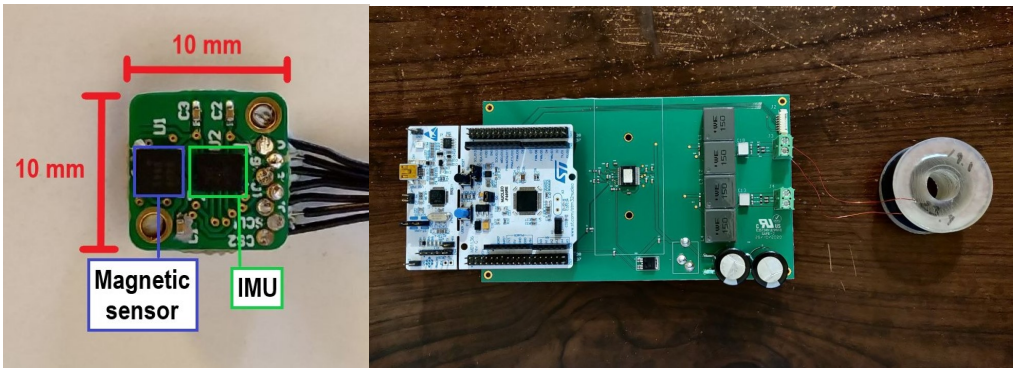

(a) (b)

Figure 4.26: New system marker hardware design (a). Field generator module integration prototype (b).

this it will be necessary to provide a minimum 5 mm spatial accuracy and 2 ° orientation accuracy within a range of 40 cm, with a 50 Hz minimum update rate.

In order to increase the tracking range, we replaced the previously used magnetic sensor KMX62-1031 with the Memsic MMC5983MA sensor capable of providing 3D magnetic flux density measurements with 18-bit precision within a range of ±800 µT with 1 kHz update rate. Furthermore, since the IMU sensor MPU9250 was discontinued, we replaced it with the Bosch BMX160 IMU that provide similar characteristics with a lower footprint. This change of sensors allows us also to replace the I2C with a SPI

port providing a higher data throughput capability between the marker and the MCU, impacting positively also any future project involving our tracking system.

Parting from these changes we designed a new marker board as shown in Fig. 4.26a. It was designed with a lower footprint than the marker shown in Fig. 4.13 to have a low impact at the time of being integrated into the ultrasound probe. It can be attached to the probe using M16 screws, while the connection port can be soldered on top of a host circuit board or directly to wires. This small footprint design could also be reused in other applications such as finger tracking.

The field generator module redesign into a more integrated prototype is shown in Fig. 4.26b, where the laboratory equipment such as the power supply and signal generator, was substituted by a single board that integrates the STEVAL-CCA044V1 power amplifier circuit, with a connection port to an ST NUCLEO-F446RE boar in charge of providing the sinusoidal signal and processing the field module generator IMU data, and power management circuit in charge of feeding the module.

Since new scattered interpolations and calibration process is yet to be developed, no accuracy test has been performed to evaluate this new design. However, we performed a preliminary test to estimate the new system hardware design range focused on evaluating the system and the scattered interpolations input signals noise.

It consisted in position both markers in a set of position points increasing the marker to bobbin distance within the ranges $7\,\text{cm} \leq R \leq 28\,\text{cm}$ for the previous design and $7\,\text{cm} \leq R \leq 44\,\text{cm}$ for the newest design. At this point, we will extract the raw sampled magnetic flux density signals and the amplitude of the processed signal.

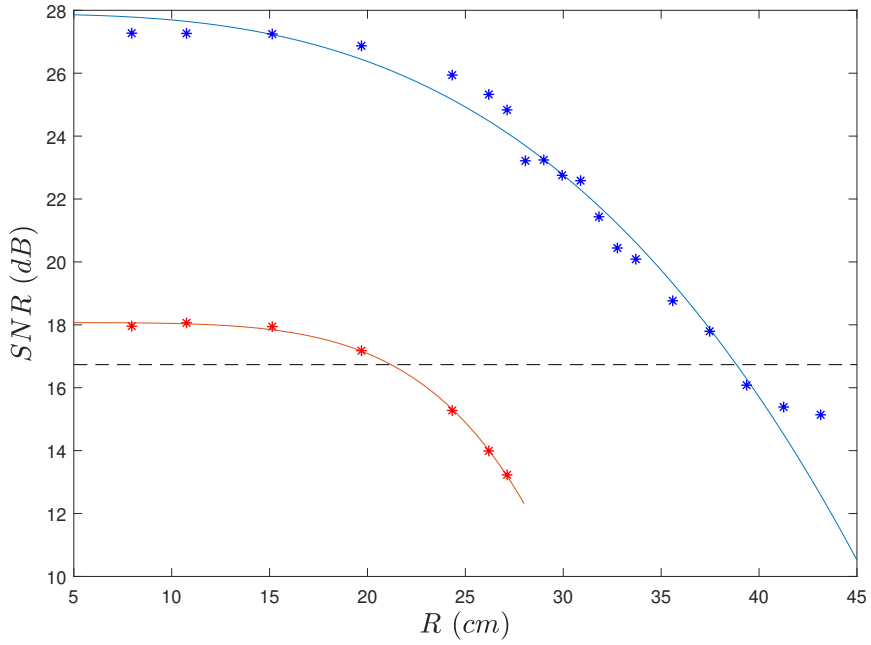

(a)

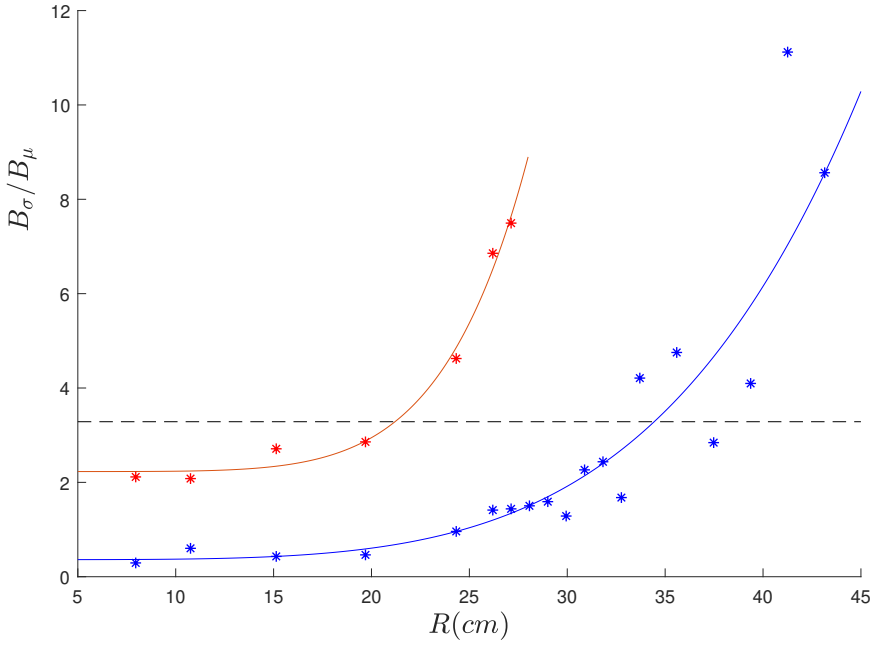

(b)

Figure 4.27: Preliminary range test results. Fitted curve for SNR (a) and processed signal amplitude noise (b) as a function to marker to bobbin distance for previous design (red) and new design (blue).

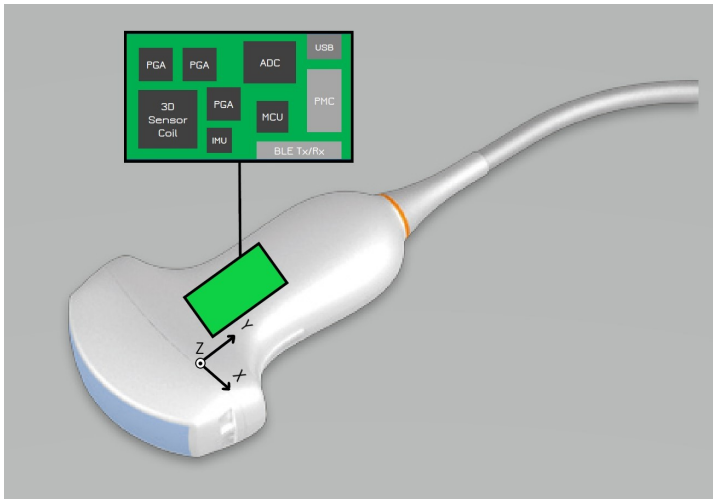

Figure 4.28: Visual example of magnetic tracking system tag integrated in ultrasound probe.

Using the raw sampled signals we calculated the Signal-to-Noise Ratio (SNR) and using the Matlab Curve Fitting tool formed a curve of both designs input SNR as a function of marker to bobbin distance. From these results, we can estimate that the new design can have the same performance at a distance of 39 cm that the previous design had at a distance of 21 cm as shown in Fig. 4.27a.

Using the processed signal amplitude from samples taken during 10 s we calculated the ratio between the standard deviation B_σ and the mean value B_μ as a representation of proportional signal noise. Using the Matlab Curve Fitting tool we formed the curves of the calculated ratio as a function of marker to bobbin distance. From these results, we can estimate that the new design can have the same performance at a distance of 34 cm that the previous design had at a distance of 21 cm as shown in Fig. 4.27b.

These results lead us to conclude that the filtering and amplitude estimation process needs to be modified to enhance the system performance to its maximum capability. Further studies and testing are yet to be done to provide a functional prototype for this project.

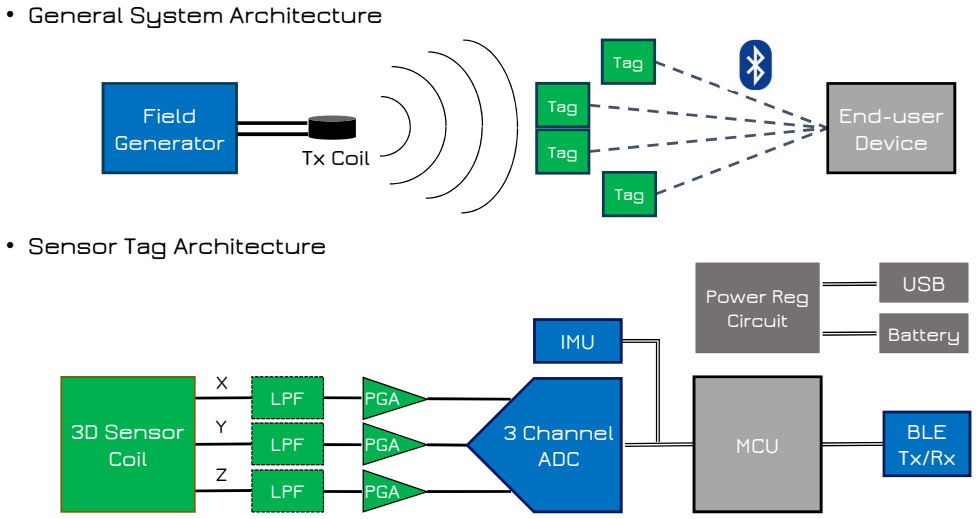

Figure 4.29: Proposed Virtual Navigator magnetic tracking system architecture and tracked tag architecture.

A second and more deep system design modification is considered to increase the tracking range from the presented 21 cm or the previously projected 39 cm range, up to 50 cm and even further. It is intended to be used in multiple ultrasound probes for medical fusion imaging.

This modification consists of integrating the magnetic sensor and the sensor module into a single magnetic tracking system tag. As shown in Fig. 4.28, the tag could be integrated inside one or multiple ultrasound probes. For this purpose, the final object can be project to be a wireless tag with reduced size under 4 cm $\times$ 2 cm $\times$ 1 cm dimensions.

We propose new design constraints consisting of the capability of tracking multiple individual tags with a minimum spatial accuracy of 5 mm inside an operational range of 50 cm $\times$ 50 cm $\times$ 50 cm, with a minimum 30 Hz rate and a maximum latency of 250 ms.

Considering the necessary increment of the tracking range and the possibility of using multiple different tracked tags designed within the given size limitations, we chose to modify the general system hardware architecture

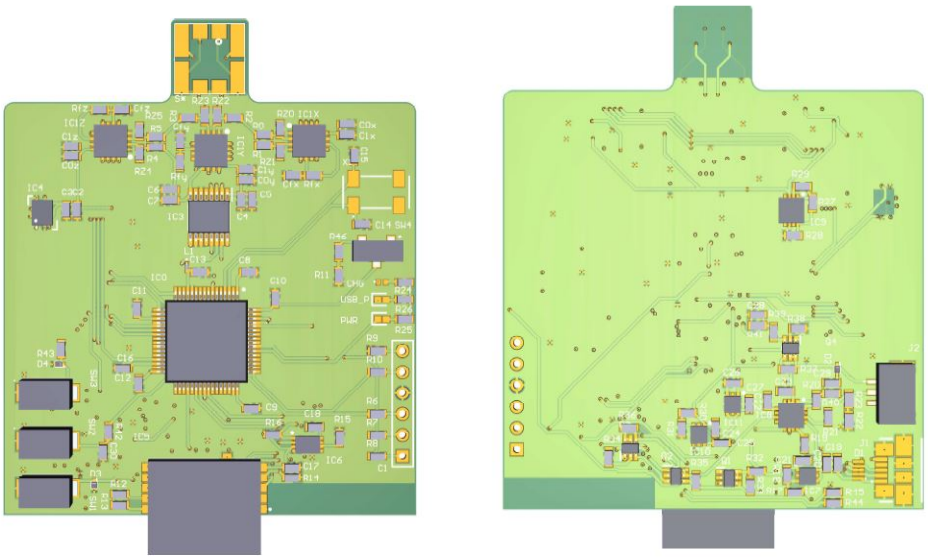

(a) (b)

Figure 4.30: Designed Sensor Tag Prototype top view (a) and bottom view (b).

as shown in Fig. 4.29.

The field generator module will be kept without modifications, while the sensing module will be conformed now by multiple individual magnetic tracking tags connected to the end-user device through BLE communication.

The major system change would consist in exchanging the digital output magnetic sensors with a 3D sensor coil followed by a LPF and a Programmable Gain Amplifier (PGA) at each output of the sensor coils, while a 3-channel ADC will sample each one of these signal chains. The rest of the sensor module architecture will be kept unmodified and integrated within each sensor tag, as shown in Fig. 4.29.

In Fig. 4.30 we can observe the first prototype design of the proposed system architecture. The design included the Premmo 3DV06 sensor coil able to provide a sensitivity of 1 mV/uT at 100 Hz, followed by the Analog Devices AD8231 PGA which provide gains ranging from $G = 1$ to $G = 128$,

and the Texas Instrument ADS8341 four channel ADC. From the previous architecture it keeps the Bosch BMX160 IMU, the STM32F446RET6 MCU and SPBTLE-RF BLE v4.2 compliant module.

This prototype is not intended to be compliant with tag size requirements yet because it includes the ports necessary for debugging and constant and easy reprogramming. The production and evaluation of this prototype are set as future research work.

Chapter 5

Conclusions

In this thesis work, we presented the development of a low complexity 6DOF magnetic tracking system for biomedical applications.

We started by introducing the types of tracking system classifications in terms of range and accuracy and in terms of the technology and techniques implemented. Following this, we introduced what is known as biomedical engineering and which are the main biomedical application sector where tracking systems can be used. Then, we discuss what kind of tracking systems are the most indicated to be used in our field of interest.

From this, we concluded that the most suitable technologies to develop a tracking system for biomedical applications are WTS, specifically optical and magnetic tracking systems. This could be extended to IMU based tracking system in the case of gait analysis applications and UWB tracking system for applications requiring ITS. However, the accuracy provided by magnetic and optical tracking systems can not be matched by other technologies.

Then, we proceed to study the literature regarding the tracking system

technologies used in the biomedical field, to understand which were the most suitable technologies for developing a tracking system with these characteristics for biomedical applications.

Specifically, we compared the use of magnetic, optical and IMU-based tracking systems by classifying the use of 45 research studies (15 for each technology) in these four categories:

- Medical Instrumentation
- Finger Motion Tracking
- Human Motion Tracking
- Human Posture Tracking

Additionally, we compared also the optical and magnetic gold standard systems' quantitative characteristics, as well as qualitative characteristics such a LOS dependency, system portability and flexibility.

This comparison led us to conclude that magnetic systems are a more portable, flexible and lower cost solution that performs accurate and reliable 6DOF tracking for critical applications such as human motion, finger motion and medical instrumentation tracking.

Moreover, using characteristics extracted from the present literature we set as initial design constrains the development of a 6DOF magnetic tracking system defining as initial design constraints:

- Spatial accuracy $\leq 5\,\text{mm}$.
- Tracking volume $= 1\,\text{m}^3$.
- Update rate $= 50\,\text{Hz}$.

- Wireless feature.

Therefore, we proceeded to study further the literature regarding magnetic tracking system research work, to solve the first research challenge presented that was choosing a hardware architecture and magnetic tracking methodology to comply with design constraints, and also to evaluate possible research contributions.

From this study, we chose to design a wearable and wireless magnetic tracking system based on the use of a lightweight algorithm onboard a small-sized low-cost MCU that can acquire and process the magnetic field signals perceived by movable sensors and transmit the estimated sensor position and orientation to an end-user device via wireless communication.

Additionally, we revised our system design constraints, in order to set a feasible tracking range of 20 cm, that can be further developed to a final goal of 50 cm. Moreover, using values extracted from literature we also defined the markers volume as an additional design constrain. The revised design constraints were set as follows:

- Spatial accuracy ≤ 5 mm.
- Tracking range = 20 cm.
- Update rate = 50 Hz.
- Wireless feature.
- Marker dimensions $\leq 1\,\text{cm}^3$.

Following this, we presented our research methodology based on Adaptive Project Framework to address the issue of choosing a proper methodology

for our system the development to test its characteristics continuously and having design flexibility through the system evolution.

This methodology projects the system development in step cycles consisting of setting the step goals, development, test and results analysis, with the intent to incrementally go from our system goals to the final system characteristics.

We introduced then our magnetic tracking technique and hardware architecture proposals, which focused on using a low computational complexity regression algorithm to transform the measured magnetic field to an estimation of the sensor position, to implement it on board a small footprint processing unit to develop a low-cost wearable electronic device capable of accurate 6DOF tracking.

Following the exposed research methodology, we presented our system development in experimental results-driven cycle steps.

First, we presented a simulation-based comparison between two low complexity regression methods extracted from the magnetic tracking literature study, regression NN and LUT. Specifically, we used a GRNN and a Scattered Interpolation method formed with the same data set. From these simulations, we determined that the scattered interpolation presented better characteristics in terms of accuracy, computational time and required memory space.

Then, we presented our first proof of concept prototype capable of estimating the sensor cylindrical coordinates ρ and Z, to test our regression methodology in real-time and to determine a preliminary system spatial accuracy. For this purpose, we implemented a simplified version of the tracking algorithm in Matlab. We then performed a static accuracy test,

and we performed a dynamical characterization of the system. We obtained a system average spatial accuracy of 6.5 mm within a 23 cm range, with 50 Hz update rate and 100 ms latency.

These preliminary results proved the real-time feasibility of the proposed regression methodology implementation and obtaining millimeter level accuracy results without any preliminary calibration procedure. Moreover, we extracted new design and implementation considerations for the next development step, involving bobbin coil redesign, changing the magnetic field frequency and tracking algorithm changes to be implemented on board of a MCU.

Taking into account these considerations, we presented the development of our 6DOF prototype capable of running the tracking algorithm on board of an M4-Cortex MCU, using the USB to sent the estimated position and orientation data to a GUI implemented in Matlab as a mean to observe in real-time the sensor 6DOF data.

Then, we a static accuracy, orientation accuracy and dynamical accuracy tests to characterize the system, obtaining an average spatial accuracy of 7.8 mm within a 21 cm range, an orientation accuracy of 1.78° and an average dynamical accuracy 7.6 mm.

From the obtained characterization, we concluded that used scattered interpolations computed from FEM simulations which do not correspond completely to what is being measured. Moreover, with further analysis, we adopted a calibration procedure consisting of the use of a representative number measurements to form a data set of position points and magnetic flux density measurements in our tracking space of interest and calibrate the existing simulated data sets.

With this procedure, a re-characterization of the system was obtained consisting in an average spatial accuracy of 2.6 mm within a 21 cm range, an orientation accuracy of 1.78° and an average dynamical accuracy 5.4 mm. This highlights a 200% static accuracy gain and a 40.7% dynamic accuracy gain from the pre-calibration test results. Moreover, the system performed in real-time with a data rate 100 Hz and a maximum latency of 12 ms using an USB output communication.

The final step of the prototype development consisted of implementing a BLE communication output transmission. A first approach consisting in implementing a custom service with seven characteristics X, Y, Z, q_{R0}, q_{R1}, q_{R2} and q_{R3} to broadcast as notifications the sensor position and orientation data updated at 100 Hz proved to be inconsistent and non-optimal.

Therefore, a second approach was adopted using a BLE UART service capable of transmitting 20 bytes per request. This approach proved to be a viable option to transmit the sensor estimated position and the orientation with a 50 Hz, as well as a current consumption of 51.1 mA which is a 8.7 mA increment from the current consumption without BLE communication.

A GUI was developed on board a Raspberry Pi 3 to use the transmitted data and graphically reconstruct the sensor 6DOF estimated data. This performed consistently with latency measurements varying between 106 ms and 150 ms.

This leave us with a final system characteristics of 2.6 mm static spatial accuracy, 5.4 mm dynamical spatial accuracy and 1.78 ° orientation accuracy within a 21 cm radius, BLE communication with a maximum measured latency of 150 ms, processing unit current consumption of 51.1 mA and a 0.54 cm^3 marker size. These characteristics are compliant with the revised system design constraints.

In order to compare our system with the state-of-the-art, we developed a FOM focusing on both system accuracy and range, but at the same time highlighting the systems wearability considering the markers volume and its use flexibility using the systems DOF. On this analysis our system ranks only second w.r.t. only wireless magnetic tracking systems to the gold standard Polhemus G4 using deeply engineered micro-sensors, and fifth overall in a list of devices composed by several commercial and research developed systems, which can be considered a very good result for such a low complexity and non-optimized prototype made with off-the-shelf components.

Additionally, approximating our prototype system initial cost below $150 and comparing it to industry gold standard system costs that can go above $12500 (Romero et al., 2017), we believe that our tracking methodology presents an affordable solution that with further system development could allow the replacement of industry gold standard instrument for the development of low-cost medical instrumentation and research assessment tools.

Moreover, we understand that we have achieved a general solution useful for biomedical applications and that it still needs to be enhanced through an application-driven re-designing process, where the characteristics of the solution, for example, accuracy, range, wireless communication availability, number of sensors or system footprint size; can be weighted in accordance to the specific application.

We consider that this work presents the basis of a low-cost and viable solution for a high accuracy tracking system that could have not only an economic impact on medical device development but also increase the scientific research production involving the assessment of human motion or human manipulated objects motion by giving to the researcher or research institutes capable of competing with gold standards at a much lower im-

plementation cost. This impact could also extend to the entertainment industry, where, with further optimization processes, the presented tracking methodology can be adopted in VR and AR systems.

Bibliography

Alarifi, A., Al-Salman, A., Alsaleh, M., Alnafessah, A., Al-Hadhrami, S., Al-Ammar, M. A., and Al-Khalifa, H. S. (2016). Ultra wideband indoor positioning technologies: Analysis and recent advances. *Sensors*, 16(5):707.

Amidror, I. (2002). Scattered data interpolation methods for electronic imaging systems: A survey. *Journal of electronic imaging*, 11(2):157–176.

Andria, G., Attivissimo, F., Di Nisio, A., Lanzolla, A. M., Ragolia, M. A., et al. (2020). Assessment of Position Repeatability Error in an Electromagnetic Tracking System for Surgical Navigation. *Sensors*, 20(4):961.

Ansuini, C., Cavallo, A., Bertone, C., and Becchio, C. (2014). The visible face of intention: why kinematics matters. *Frontiers in psychology*, 5:815.

Arachchi, S. K., Xiang, C., Kumara, W., Wu, S.-J., and Shih, T. K. (2016). Motion tracking by sensors for real-time human skeleton animation. *ICTer*, 9(2).

Armand, S., Sangeux, M., and Baker, R. (2014). Optimal markers' placement on the thorax for clinical gait analysis. *Gait & posture*, 39(1):147–153.

Attivissimo, F., Lanzolla, A. M. L., Carlone, S., Larizza, P., and Brunetti, G. (2018). A novel electromagnetic tracking system for surgery navigation. *Computer Assisted Surgery*, 23(1):42–52.

Atuegwu, N. and Galloway, R. (2008). Volumetric characterization of the Aurora magnetic tracker system for image-guided transorbital endoscopic procedures. *Physics in Medicine & Biology*, 53(16):4355.

Aufdenblatten, C. A. and Altermatt, S. (2008). Intraventricular catheter placement by electromagnetic navigation safely applied in a paediatric major head injury patient. *Child's Nervous System*, 24(9):1047.

Baldi, T. L., Scheggi, S., Meli, L., Mohammadi, M., and Prattichizzo, D. (2017). GESTO: A glove for enhanced sensing and touching based on inertial and magnetic sensors for hand tracking and cutaneous feedback. *IEEE Transactions on Human-Machine Systems*, 47(6):1066–1076.

Bellitti, P., De Angelis, A., Dionigi, M., Sardini, E., Serpelloni, M., Moschitta, A., and Carbone, P. (2020). A Wearable and Wirelessly Powered System for Multiple Finger Tracking. *IEEE Transactions on Instrumentation and Measurement*, 69(5):2542–2551.

Bennet, T. (2020). What are attitude and heading reference systems? - ahrs. https://inertialsense.com/attitude-heading-reference-systems-ahrs-explained/.

Bulić, P., Kojek, G., and Biasizzo, A. (2019). Data transmission efficiency in Bluetooth Low Energy versions. *Sensors*, 19(17):3746.

Carse, B., Meadows, B., Bowers, R., and Rowe, P. (2013). Affordable clinical gait analysis: An assessment of the marker tracking accuracy

of a new low-cost optical 3D motion analysis system. *Physiotherapy*, 99(4):347–351.

Cavallo, A., Cirillo, A., Cirillo, P., De Maria, G., Falco, P., Natale, C., and Pirozzi, S. (2014). Experimental comparison of sensor fusion algorithms for attitude estimation. *IFAC Proceedings Volumes*, 47(3):7585–7591.

Chen, C.-F., Kuo, Y.-H., Luh, J.-J., Chen, Y.-J., Chen, S.-W., Kuo, T.-S., and Lai, J.-S. (2013). Reducing anterior tibial translation by applying functional electrical stimulation in dynamic knee extension exercises: Quantitative results acquired via marker tracking. *Clinical Biomechanics*, 28(5):549–554.

Chen, K.-Y., Patel, S. N., and Keller, S. (2016). Finexus: Tracking precise motions of multiple fingertips using magnetic sensing. In *Proceedings of the 2016 CHI Conference on Human Factors in Computing Systems*, pages 1504–1514.

Colton, S. and Mentor, F. (2007). The balance filter. *Presentation, Massachusetts Institute of Technology*.

Condino, S., Ferrari, V., Freschi, C., Alberti, A., Berchiolli, R., Mosca, F., and Ferrari, M. (2012). Electromagnetic navigation platform for endovascular surgery: how to develop sensorized catheters and guidewires. *The International Journal of Medical Robotics and Computer Assisted Surgery*, 8(3):300–310.

Cordella, F., Di Corato, F., Zollo, L., Siciliano, B., and van der Smagt, P. (2012). Patient performance evaluation using Kinect and Monte Carlo-based finger tracking. In *2012 4th IEEE RAS & EMBS International Conference on Biomedical Robotics and Biomechatronics (BioRob)*, pages 1967–1972. IEEE.

Curran, K., Furey, E., Lunney, T., Santos, J., Woods, D., and McCaughey, A. (2011). An evaluation of indoor location determination technologies. *Journal of Location Based Services*, 5(2):61–78.

De Angelis, A., Moschitta, A., and Comuniello, A. (2017). Tdoa based positioning using ultrasound signals and wireless nodes. In *2017 IEEE International Instrumentation and Measurement Technology Conference (I2MTC)*, pages 1–6. IEEE.

Doering, M., Sommer, P., Rolf, S., Lucas, J., Breithardt, O. A., Hindricks, G., and Richter, S. (2015). Sensor-based electromagnetic navigation to facilitate implantation of left ventricular leads in cardiac resynchronization therapy. *Journal of Cardiovascular Electrophysiology*, 26(2):167–175.

Dotlic, I., Connell, A., Ma, H., Clancy, J., and McLaughlin, M. (2017). Angle of arrival estimation using decawave DW1000 integrated circuits. In *2017 14th Workshop on Positioning, Navigation and Communications (WPNC)*, pages 1–6. IEEE.

Eikerling, H.-J., Uelschen, M., and Stuntebeck, B. (2017). Efficient techniques for gait-analysis: comparing marker-less and IMU-based tracking systems for monitoring rehabilitation processes. In *EMBEC & NBC 2017*, pages 860–863. Springer.

Enderle, J. (2012). *Introduction to biomedical engineering*. Academic press.

Engelhardt, S., De Simone, R., Al-Maisary, S., Kolb, S., Karck, M., Meinzer, H.-P., and Wolf, I. (2016). Accuracy evaluation of a mitral valve surgery assistance system based on optical tracking. *International journal of computer assisted radiology and surgery*, 11(10):1891–1904.

Esaote (2015). Let the Fusion begin! CT, MR, PET side-by-side with Real-time Ultrasound. Retrieved from https://www.esaote.com/uploads/tx_esaotedocuments/VirtualNavigator_160000032MAK_V04.pdf.

Fernandez G, D. A., Macrelli, E., Demarchi, D., and Crepaldi, M. (2018). High-accuracy wireless 6DOF magnetic tracking system based on FEM modeling. In *2018 25th IEEE International Conference on Electronics, Circuits and Systems (ICECS)*, pages 413–416. IEEE.

Fernandez G, D. A., Ros, P. M., Demarchi, D., and Crepaldi, M. (2020). A Low-Complexity 6DOF Magnetic Tracking System Based on Pre-Computed Data Sets for Wearable Applications. *IEEE Transactions on Circuits and Systems I: Regular Papers*, 67(12):5065–5078.

Franz, A. M., Haidegger, T., Birkfellner, W., Cleary, K., Peters, T. M., and Maier-Hein, L. (2014). Electromagnetic Tracking in Medicine—A review of technology, validation, and applications. *IEEE transactions on medical imaging*, 33(8):1702–1725.

Grewal, M. S., Weill, L. R., and Andrews, A. P. (2007). *Global positioning systems, inertial navigation, and integration*. John Wiley & Sons.

Gürkan, G. (2020). PyTHang: an open-source wearable sensor system for real-time monitoring of head-torso angle for ambulatory applications. *Computer Methods in Biomechanics and Biomedical Engineering*, pages 1–16.

Hamza-Lup, F. G., Rolland, J. P., and Hughes, C. (2018). A distributed augmented reality system for medical training and simulation. *arXiv preprint arXiv:1811.12815*.

Hsu, M. H., Shih, T. K., and Chiang, J. S. (2014). Real-time finger tracking

for virtual instruments. In *2014 7th International Conference on Ubi-Media Computing and Workshops*, pages 133–138. IEEE.

Huang, J., Mori, T., Takashima, K., Hashi, S., and Kitamura, Y. (2016). 6-DOF computation and marker design for magnetic 3D dexterous motion-tracking system. In *Proceedings of the 22nd ACM Conference on Virtual Reality Software and Technology*, pages 211–217.

Khoshelham, K. and Elberink, S. O. (2012). Accuracy and resolution of kinect depth data for indoor mapping applications. *Sensors*, 12(2):1437–1454.

Kim, Y. and Bang, H. (2018). Introduction to Kalman filter and its applications. *Introduction and Implementations of the Kalman Filter*, 1:1–16.

Kim, Y., Kim, P. C., Selle, R., Shademan, A., and Krieger, A. (2014). Experimental evaluation of contact-less hand tracking systems for tele-operation of surgical tasks. In *2014 IEEE International Conference on Robotics and Automation (ICRA)*, pages 3502–3509. IEEE.

Klöpfer-Krämer, I., Brand, A., Wackerle, H., Müßig, J., Kröger, I., and Augat, P. (2020). Gait analysis–Available platforms for outcome assessment. *Injury*, 51:S90–S96.

Lebel, K., Boissy, P., Nguyen, H., and Duval, C. (2016). Proposition and Validation of a New Index to Determine the Measurement Change Resolution of Inertial Motion Tracking Systems. In *Proceedings of the 6th International Conference on Digital Health Conference*, pages 43–46.

Lechner, W. and Baumann, S. (2000). Global navigation satellite systems. *Computers and Electronics in Agriculture*, 25(1-2):67–85.

Lee, J., Kang, J., and Song, T.-k. (2015). 6-DOF free-hand navigation interface for volumetric 3-dimensional ultrasound imaging: Preliminary results. In *2015 IEEE International Ultrasonics Symposium (IUS)*, pages 1–4. IEEE.

Li, M., Wang, C., Liu, Q., Duan, L., Wu, Z., Sun, T., Liu, Q., Li, W., Lu, Z., Chen, H., et al. (2016). Lower limb motion analysis based on inertial sensor. In *2016 International Conference on Advanced Robotics and Mechatronics (ICARM)*, pages 347–352. IEEE.

Li, X. and Wang, Y. (2019). Evaluation of AHRS algorithms for foot-mounted inertial-based indoor navigation systems. *Open Geosciences*, 11(1):48–63.

Li, X., Wang, Y., and Khoshelham, K. (2018). UWB/PDR tightly coupled navigation with robust extended Kalman filter for NLOS environments. *Mobile Information Systems*, 2018.

Liang, R.-H., Cheng, K.-Y., Su, C.-H., Weng, C.-T., Chen, B.-Y., and Yang, D.-N. (2012). GaussSense: Attachable stylus sensing using magnetic sensor grid. In *Proceedings of the 25th annual ACM symposium on User interface software and technology*, pages 319–326.

Lin, Q., Yang, R., Cai, K., Guan, P., Xiao, W., and Wu, X. (2015). Strategy for accurate liver intervention by an optical tracking system. *Biomedical Optics Express*, 6(9):3287–3302.

Lockery, D., Peters, J. F., Ramanna, S., Shay, B. L., and Szturm, T. (2011). Store-and-feedforward adaptive gaming system for hand-finger motion tracking in telerehabilitation. *IEEE Transactions on Information Technology in Biomedicine*, 15(3):467–473.

Lund, K. T., Tangen, G. A., and Manstad-Hulaas, F. (2017). Electromagnetic navigation versus fluoroscopy in aortic endovascular procedures: A phantom study. *International journal of computer assisted radiology and surgery*, 12(1):51–57.

Mackey, A., Spachos, P., Song, L., and Plataniotis, K. N. (2020). Improving BLE beacon proximity estimation accuracy through Bayesian filtering. *IEEE Internet of Things Journal*, 7(4):3160–3169.

MacRitchie, J. and McPherson, A. P. (2015). Integrating optical finger motion tracking with surface touch events. *Frontiers in psychology*, 6:702.

Madgwick, S. O., Harrison, A. J., and Vaidyanathan, R. (2011). Estimation of IMU and MARG orientation using a gradient descent algorithm. In *2011 IEEE international conference on rehabilitation robotics*, pages 1–7. IEEE.

Mason, B., Lenton, J., Rhodes, J., Cooper, R., and Goosey-Tolfrey, V. (2014). Comparing the activity profiles of wheelchair rugby using a miniaturised data logger and radio-frequency tracking system. *BioMed research international*, 2014.

MathWorks (2021). Generalized Regression Neural Networks. Retrieved from https://it.mathworks.com/help/deeplearning/ug/generalized-regression-neural-networks.html.

Memeo, M. and Brayda, L. (2016). How geometrical descriptors help to build cognitive maps of solid geometry with a 3DOF tactile mouse. In *International Conference on Human Haptic Sensing and Touch Enabled Computer Applications*, pages 75–85. Springer.

Mohd, B. J., Amro, I., and Alhasani, A. (2017). Indoor Wi-Fi tracking

system using fingerprinting and Kalman filter. In *2017 IEEE Jordan Conference on Applied Electrical Engineering and Computing Technologies (AEECT)*, pages 1–6. IEEE.

Montaser, A. and Moselhi, O. (2014). RFID indoor location identification for construction projects. *Automation in Construction*, 39:167–179.

NDI (2021a). NDI Polaris Vega XT. Retrieved from https://www.ndigital.com/products/polaris-vega/polaris-vega-xt/.

NDI (2021b). NDI TrackStar. Retrieved from https://www.ndigital.com/products/aurora/.

NDI (2021c). NDI TrakStar. Retrieved from https://www.ndigital.com/products/3d-guidance/.

Ong, A., Harris, I. S., and Hamill, J. (2017). The efficacy of a video-based marker-less tracking system for gait analysis. *Computer methods in BiomeChaniCs and BiomediCal engineering*, 20(10):1089–1095.

Optitrack (2021). Optitrack Prime 22. Retrieved from https://optitrack.com/cameras/primex-22/.

Parizi, F. S., Whitmire, E., and Patel, S. (2019). AuraRing: Precise Electromagnetic Finger Tracking. *Proceedings of the ACM on Interactive, Mobile, Wearable and Ubiquitous Technologies*, 3(4):1–28.

Pereira, A. C. C. (2016). 3DArm Inertial Sensor-based 3D Upper Limb Motion Tracking and Trajectories Reconstruction.

Perez, E., López, N., Dominguez, M., and Orosco, E. (2019). Inertial Measurement System for Upper Limb Joints Tracking. In *World Congress on Medical Physics and Biomedical Engineering 2018*, pages 785–789. Springer.

Polhemus (2017). Hand and Finger Trackers. Retrieved from https://polhemus.com/motion-tracking/hand-and-finger-trackers/.

Polhemus (2021a). Polhemus G4. Retrieved from https://polhemus.com/motion-tracking/all-trackers/g4#collapseFour.

Polhemus (2021b). Polhemus Patriot. Retrieved from https://polhemus.com/motion-tracking/all-trackers/patriot.

Polhemus (2021c). Polhemus Patriot Wireless. Retrieved from https://polhemus.com/motion-tracking/all-trackers/patriot-wireless.

Punithakumar, K., Hareendranathan, A. R., McNulty, A., Biamonte, M., He, A., Noga, M., Boulanger, P., and Becher, H. (2016). Multiview 3-D echocardiography fusion with breath-hold position tracking using an optical tracking system. *Ultrasound in medicine & biology*, 42(8):1998–2009.

Raab, F. H., Blood, E. B., Steiner, T. O., and Jones, H. R. (1979). Magnetic Position and Orientation Tracking System. *IEEE Transactions on Aerospace and Electronic Systems*, (5):709–718.

Roetenberg, D., Luinge, H., and Slycke, P. (2009). Xsens MVN: Full 6DOF human motion tracking using miniature inertial sensors. *Xsens Motion Technologies BV, Tech. Rep*, 1.

Romero, V., Amaral, J., Fitzpatrick, P., Schmidt, R., Duncan, A. W., and Richardson, M. J. (2017). Can low-cost motion-tracking systems substitute a Polhemus system when researching social motor coordination in children? *Behavior research methods*, 49(2):588–601.

Salchow-Hömmen, C., Callies, L., Laidig, D., Valtin, M., Schauer, T., and

Seel, T. (2019). A tangible solution for hand motion tracking in clinical applications. *Sensors*, 19(1):208.

Sapienza, S., Ros, P. M., Guzman, D. A. F., Rossi, F., Terracciano, R., Cordedda, E., and Demarchi, D. (2018). On-line event-driven hand gesture recognition based on surface electromyographic signals. In *2018 IEEE international symposium on circuits and systems (ISCAS)*, pages 1–5. IEEE.

Schneider, D., Otte, A., Kublin, A. S., Martschenko, A., Kristensson, P. O., Ofek, E., Pahud, M., and Grubert, J. (2020). Accuracy of commodity finger tracking systems for virtual reality head-mounted displays. In *2020 IEEE Conference on Virtual Reality and 3D User Interfaces Abstracts and Workshops (VRW)*, pages 805–806. IEEE.

Schwein, A., Kramer, B., Chinnadurai, P., Walker, S., O'Malley, M., Lumsden, A., and Bismuth, J. (2017). Flexible robotics with electromagnetic tracking improves safety and efficiency during in vitro endovascular navigation. *Journal of vascular surgery*, 65(2):530–537.

Seuté, H., Enderli, C., Grandin, J.-F., Khenchaf, A., and Cexus, J.-C. (2016). Experimental measurement of time difference of arrival. In *2016 17th International Radar Symposium (IRS)*, pages 1–4. IEEE.

Terabee (2020). Time-of-Flight principle: Technologies and advantages. Retrieved from https://www.terabee.com/time-of-flight-principle/.

Tosi, J., Taffoni, F., Santacatterina, M., Sannino, R., and Formica, D. (2017). Performance evaluation of bluetooth low energy: A systematic review. *Sensors*, 17(12):2898.

Tran, H., Pathirana, P. N., Horne, M., Power, L., and Szmulewicz, D.

(2018). Automated finger chase (ballistic tracking) in the assessment of cerebellar ataxia. In *2018 40th Annual International Conference of the IEEE Engineering in Medicine and Biology Society (EMBC)*, pages 3521–3524. IEEE.

UKEssays (2018). Overview Of Tracking Devices Information Technology Essay. Retrieved from https://www.ukessays.com/essays/information-technology/overview-of-tracking-devices-information-technology-essay.php.

Uttam, B. J. and D'Appolito, J. A. (1975). Direct-Ranging Loran Model Identification and Performance Predictions. *IEEE Transactions on Aerospace and Electronic Systems*, AES-11(3):380–385.

Valldeperes, A., Altuna, X., Martinez-Basterra, Z., Rossi-Izquierdo, M., Benitez-Rosario, J., Perez-Fernandez, N., and Rey-Martinez, J. (2019). Wireless inertial measurement unit (IMU)-based posturography. *European Archives of Oto-Rhino-Laryngology*, 276(11):3057–3065.

VICON (2021). Vicon Cameras. Retrieved from https://www.vicon.com/hardware/cameras.

Weenk, D., Roetenberg, D., van Beijnum, B.-J. J., Hermens, H. J., and Veltink, P. H. (2014). Ambulatory estimation of relative foot positions by fusing ultrasound and inertial sensor data. *IEEE transactions on neural systems and rehabilitation engineering*, 23(5):817–826.

Weichert, F., Bachmann, D., Rudak, B., and Fisseler, D. (2013). Analysis of the accuracy and robustness of the leap motion controller. *Sensors*, 13(5):6380–6393.

Wong, S., Jassemi, R., Brookes, D., and Kim, B. (2017). A geometric approach to passive target localization.

Xu, H.-X., Lu, M.-D., Liu, L.-N., and Guo, L.-H. (2012). Magnetic navigation in ultrasound-guided interventional radiology procedures. *Clinical radiology*, 67(5):447–454.

Yang, W., Xiu, C., Zhang, J., and Yang, D. (2017). A novel 3D pedestrian navigation method for a multiple sensors-based foot-mounted inertial system. *Sensors*, 17(11):2695.

Yoon, S. H., Zhang, Y., Huo, K., and Ramani, K. (2016). TRing: Instant and customizable interactions with objects using an embedded magnet and a finger-worn device. In *Proceedings of the 29th Annual Symposium on User Interface Software and Technology*, pages 169–181.

Zügner, R., Tranberg, R., Timperley, J., Hodgins, D., Mohaddes, M., and Kärrholm, J. (2019). Validation of inertial measurement units with optical tracking system in patients operated with total hip arthroplasty. *BMC musculoskeletal disorders*, 20(1):52.